

EFFECT OF ALKANETHIOL SELF-ASSEMBLED MONOLAYERS ON THE PLASTIC
AND ELASTIC DEFORMATION OF GOLD (111) FILMS

By

MILCA I. APONTE

A Dissertation submitted to the

Graduate School-New Brunswick

Rutgers, The State University of New Jersey

in partial fulfillment of the requirements

for the degree of

Doctor of Philosophy

Graduate Program in Materials Science & Engineering

written under the direction of

Dr. Adrian B. Mann

and approved by

New Brunswick, New Jersey

May, 2010

ABSTRACT OF THE DISSERTATION

EFFECT OF ALKANETHIOL SELF-ASSEMBLED MONOLAYERS ON THE PLASTIC
AND ELASTIC DEFORMATION OF GOLD (111) FILMS

By MILCA I. APONTE

Dissertation Director:

Dr. Adrian B. Mann

Surface chemistry is known to affect the elastic deformation of nanocontacts, but its role in plastic deformation is less clear. Alkanethiol self-assembled monolayers (SAMs) were used to modify the surface energy and surface stress of Au(111) films. The chemical effect of this nanometer scale film on elastic and plastic deformation was investigated using nanoindentation combined with atomic force microscopy (AFM) imaging of indents. A range of maximum indentation displacements and SAM chain lengths were used. Comparisons were made between the mechanical response of the gold substrate alone and the gold modified with the different SAMs.

The nanoindentation load-displacement curves and the mechanical properties were found to be dependent on the presence of the SAM. A decrease in the reduced elastic modulus was observed when indenting the SAM systems. The work of indentation and the hardness showed a similar effect with the SAM layer lowering hardness in both cases. Remarkably, the SAM was found to affect hardness, and hence plasticity, at indentation depths over 100 times the SAM thickness. Comparisons were made between the projected contact areas approximated using the Oliver and Pharr method with the actual

areas directly measured by AFM analysis. This accounts for underestimation of the contact area due to pile-up of gold around the indent. AFM characterization of the residual nanoindentation impressions showed substantial differences between the indent shape and pile-up when comparing the gold to the gold plus SAM surfaces. The differences are more pronounced for the longer chain length SAM and as the indents become deeper. The SAM reduces the adhesion force between the indenter tip and surface which may affect the observed mechanical properties for shallow indents. For the deeper indentations the exothermic reaction of the alkanethiol molecules chemisorbed on the gold surface reduces the surface free energy of the gold substrate which favors the creation of new surface (pile-up). In addition, surface stress which is compressive when a SAM is present, but tensile otherwise, appears to modify the behavior of dislocations and strain hardening in the Au films. This is the most likely cause of the dramatic change in hardness and pile-up.

Dedication

This thesis is dedicated to my family and my friends.

My dear and lovely husband, Henry Miranda, my parents Ivette Román & Luis F. Aponte
and my siblings Camil I. Aponte Román, Luis F. Aponte Román, Andrés J. Rosa Román
and Lucas Rosa Román.

Acknowledgments

Grateful acknowledgment is made to my thesis advisor Dr. Adrian B. Mann. The author appreciates many helpful conversations with her colleagues/friends: Dr. Beril Kavukcuoglu, Dr. Sandip Basu, Dr. Julien Boisse, and Wojtek Tutak. I would also want to thank Henry Miranda, Wantinne Viratyaporn, Maryam Abazari, Piyalak Ngerchuklin (Note), Stuart Deutsch, Roberto Delgado, José Fernández, Patricia Irizarry, Alokik Kanwal, Sarika Phadke, Syeda S. Hussain, Prof. Idalia Ramos, Prof. Lisa Klein, Mr. John Yaniero, Mrs. Mercedes, Mrs. Claudia Kuchinow and all the graduate students from the Materials Science & Engineering Department who made my stay in Rutgers unforgettable. I would also like to acknowledge the financial support given by the National Science Foundation through its IGERT program on Integratively Engineered Biointerfaces at Rutgers University. Finally, but not less, I owe my deepest gratitude to my committee members; Dr. Thomas Tsakalakos, Dr. Frederic Cosandey, Dr. Tewodros Asefa, and Dr. Dunbar P. Birnie III.

Table of Contents

I	ABSTRACT.....	ii
II	DEDICATION.....	iv
III	ACNOWLEDGEMENTS.....	v
1	INTRODUCTION.....	1
2	BACKGROUND.....	4
	2.1 ELASTIC AND PLASTIC BEHAVIOR OF METALS.....	4
	2.2 DISLOCATION PROPERTIES.....	5
	2.2.1 Motion of Dislocations in Soft Metals.....	6
	2.3 STRAIN HARDENING.....	9
	2.4 SURFACE ENERGY, SURFACE STRESS AND INTERFACIAL STRESS.....	9
	2.5 GOLD.....	10
	2.6 SURFACE FREE ENERGY.....	11
	2.6.1 The Owens-Wendt Method.....	13
	2.7 NANOINDENTATION.....	14
	2.7.1 Projected Area.....	15
	2.8 CONTACT MECHANICS AND ADHESIVE FORCES.....	16
	2.9 SELF-ASSEMBLED MONOLAYERS.....	18
	2.9.1 Alkanethiol Self-Assembly Kinetics.....	19
	2.9.2 Physisorption and Chemisorption.....	21
	2.9.3 Self-Assembled Monolayers Applications.....	22
	2.9.4 Characterization of the Monolayer.....	23

3	PHYSICAL AND CHEMICAL CHARACTERIZATION OF ALKANETHIOL SELF-ASSEMBLED MONOLAYERS ON GOLD(111).....	24
3.1	MATERIALS.....	24
3.1.1	Substrate Preparation.....	24
3.1.2	Deposition of Self-Assembled Monolayers.....	25
3.2	X-RAY DIFFRACTION.....	27
3.2.1	Experimental Methods.....	27
3.2.2	Results and Conclusions.....	27
3.3	AFM ON GOLD (111).....	29
3.4	ELLIPSOMETRY.....	31
3.4.1	Experimental Methods.....	32
3.4.2	Results and Conclusion.....	33
3.5	RAMAN SPECTROSCOPY.....	34
3.5.1	Raman Basic Theory.....	35
3.5.2	Surface-Enhanced Raman Spectroscopy (SERS).....	36
3.5.3	Experimental Methods.....	37
3.5.4	Results and Conclusions.....	38
3.6	DETERMINATION OF SURFACE ENERGY BY CONTACT ANGLE MEASUREMENTS.....	40
3.6.1	Experimental Methods.....	40
3.6.2	Results and Conclusions.....	40
4	NANOMECHANICS OF ALKANETHIOL SELF-ASSEMBLED MONOLAYERS.....	43

4.1 INTRODUCTION.....	43
4.2 NANOINDENTATION EXPERIMENTAL METHODS.....	44
4.3 OLIVER AND PHARR ANALYSIS.....	45
4.4 RESULTS AND CONCLUSIONS.....	46
4.4.1 Oliver and Pharr Hardness and Reduced Elastic Modulus.....	51
4.4.2 Work of Indentation.....	56
4.5 EFFECT OF CHAIN LENGTH ON THE NANOMECHANICS OF ALKANETHIOL SELF-ASSEMBLED MONOLAYERS.....	62
5 RESIDUAL NANOINDENTATION IMPRESION ANALYSIS BY ATOMIC FORCE MICROSCOPY.....	64
5.1 INFLUENCE OF PILE-UP ON THE INDENTATION CONTACT AREA.....	64
5.2 ATOMIC FORCE MICROSCOPY.....	67
5.3 EXPERIMENTAL METHODS.....	69
5.4 RESULTS AND DISCUSSIONS.....	71
5.4.1 Nanoindentation AFM Impression Images.....	71
5.4.2 Force Measurements.....	83
5.5 EFFECT ON SURFACE AREA.....	85
5.5.1 Numerical Definition of Surface Area.....	85
5.5.2 Surface Area Calculations.....	87
5.5.3 Results and Conclusions.....	87
5.6 PROJECTED AREA OF CONTACT.....	95
5.7 RESULTS AND CONCLUSIONS.....	98
5.7.1 Hardness from AFM Images.....	98

5.7.2	Reduced Elastic Modulus from AFM Images.....	102
5.7.3	Relationship Between Hardness, Elastic Modulus and Work of Indentation.....	105
6	DISCUSSION AND GENERAL CONCLUSIONS.....	107
7	ADDITIONAL WORK.....	123
7.1	SELF ASSEMBLED-MONOLAYER PHOTOPOLYMERIZATION.....	123
7.1.1	Introduction.....	123
7.1.2	Materials and Methods.....	124
7.1.3	Results and Conclusions.....	125
7.2	PROLIFERATION AND MINERALIZATION OF HUMAN OSTEOSARCOMA CELLS ON DIFFERENT POLYARYLATES AND POLYCARBONATES SUBSTRATES.....	130
7.2.1	Introduction.....	130
7.2.2	Materials and Methods.....	130
7.2.3	Results and Conclusions.....	132
7.3	MECHANICAL CHARACTERIZATION OF PHARMACEUTICAL COMPACTS AND SINGLE CRYSTALS.....	134
7.3.1	Introduction.....	134
7.3.2	Materials and Methods.....	135
7.3.3	Results and Conclusions.....	139
8	APPENDIX.....	141
9	REFERENCES.....	179
IV	CURRICULUM VITA.....	191

Lists of Tables

Chapter 3: Physical and Chemical Characterization of Alkanethiol Self-Assembled Monolayers on Gold(111)

Table 3.1 Raman peak assignments for decanethiol monolayer on Au(111).....	39
Table 3.2 Surface tension data of the applied measuring liquids against air.....	40
Table 3.3 Overview of the measured contact angles.....	41
Table 3.4 Surface energies with their respective disperse and polar components.....	41

Chapter 4: Nanomechanics of Alkanethiol Self-Assembled Monolayers

Table 4.1 Difference in the average maximum load needed for a given displacement between Au(111) and Au(111) + SAM.....	47
--	----

Chapter 5: Residual Nanoindentation Impression Analysis by Atomic Force Microscopy

Table 5.1 Percentage increase in surface area for indents with SAM layer compared to indents on clean Au(111).....	89
Table 5.2 Percentage increase in pile-up height for indents with a SAM layer compared to indents on clean Au(111).....	92
Table 5.3 Percentage decrease in H^{AFM} for indents with a SAM layer compared to indents on clean gold.....	98
Table 5.4 Percentage decrease in E^{AFM} for indents with a SAM layer compared to indents on clean Au(111).....	102

Chapter 6: Discussion and General Conclusions

Table 6.1 Comparison between the projected areas of contact estimated from the Oliver and Pharr (O&P) method and areas approximated from the AFM images of the nanoindentation residual impressions on Dode/SAM.....	108
---	-----

Chapter 7: Additional Work

Table 7.1 Polyarylate Series. Code number and polymer.....	131
Table 7.2 Polycarbonate Series. Code number and polymer.....	131
Table 7.3 Tensile strength and Young modulus (E) of acetaminophen and sucrose single crystals using simple compression experiments.	139
Table 7.4 Average values of stiffness, reduced Young's modulus and hardness of 66 acetaminophen and 48 sucrose single crystals obtained by nanoindentation.....	140
Table 7.5 Applied plasticity theory for sucrose and acetaminophen using a 1.25 inches die for closed-die compression.....	140

List of Illustrations

Chapter 2: Background

Figure 2.1 (a) Edge dislocation in a simple cubic lattice. (b) A screw dislocation beginning at the side of a cubic crystal lattice.....	5
Figure 2.2 Screw dislocation and its image near a free surface.....	8
Figure 2.3 Scheme of a drop on the surface of a solid showing interactions described in Young's equation between a solid and liquid.....	12
Figure 2.4 Typical nanoindentation curve.....	15
Figure 2.5 Schematic of an indentation showing quantity h_p used for analysis of the projected area.....	16
Figure 2.6 Schematic diagram of alkanethiol on Au(111) monolayer.....	21

Chapter 3: Physical and Chemical Characterization of Alkanethiol Self-Assembled Monolayers on Gold(111)

Figure 3.1 n-alkanethiol, carboxyalkanethiols and aminoalkanethiol chemical structure.....	26
Figure 3.2 X-ray diffraction pattern of a 20 nm Au film evaporated onto a glass slide....	28
Figure 3.3 AFM deflection image of gold surface prepared by evaporation of gold onto a glass coverslip.....	29
Figure 3.4 AFM section analysis showing gold film thickness.....	30
Figure 3.5 Basic principles of ellipsometry.....	32

Figure 3.6 Electronic transitions accompanying Raman and Rayleigh scattering	36
Figure 3.7 Raman spectra at room temperature of Au, 1-decanethiol monolayer grown on Au, 11-amino-1-undecanethiol monolayer grown on Au, and 10-carboxy-1-decanethiol grown on Au.....	38
Figure 3.8 Raman spectra of Au film and a 1-decanethiol SAM adsorbed on a thin layer of Au.....	39

Chapter 4: Nanomechanics of Alkanethiol Self-Assembled Monolayers

Figure 4.1 Characteristic load-displacement curves for ~20 nm Au(111) film on glass and octanethiol SAM on the same gold substrate.....	48
Figure 4.2 Characteristic load-displacement curves for ~20 nm Au(111) film on glass and decanethiol SAM on the same gold substrate.....	49
Figure 4.3 Characteristic load-displacement curves for ~20 nm Au(111) film on glass and dodecanethiol SAM on the same gold substrate.....	50
Figure 4.4 Oliver and Pharr's hardness for glass, evaporated gold on glass and (a) Octa/SAM, (b) Deca/SAM and (c) Dode/SAM as a function of maximum tip displacements.....	52
Figure 4.5 Oliver and Pharr's reduced elastic modulus for glass, evaporated gold on glass and (a) Octa/SAM, (b) Deca/SAM and (c) Dode/SAM grown on the corresponding gold surfaces as a function of maximum tip displacements.....	55
Figure 4.6 The plastic and elastic areas enclosed by the load-displacement curve.....	56

Figure 4.7 Values for works of indentation obtained by integration of the load-displacement curves by the trapezoid rule.....	59
Figure 4.8 Comparison between the total work of indentation (W_{tot}) in femto Joules for Au(111) and Au(111) modified with different SAMs for maximum tip displacements of (a) 40 nm, (b) 90 nm, (c) 140 nm, and (d) 190 nm.....	60
Figure 4.9 Comparison between the plastic work of indentation (W_p) in femto Joules for Au(111) and Au(111) modified with different SAMs for maximum tip displacements of (a) 40 nm, (b) 90 nm, (c) 140 nm, and (d) 190 nm.....	61
 Chapter 5: Residual Nanonindentation Impression Analysis by Atomic Force Microscopy	
Figure 5.1 Effect of piling-up (a) and sinking-in (b) on the area of contact, h_p for the same maximum depth h_{max}	66
Figure 5.2 AFM deflection image of indents from the four different maximum tip displacements; 40 nm, 90 nm, 140 nm and 190 nm for the Au substrate.....	71
Figure 5.3 Representative AFM deflection images of residual nanoindentation impressions on Au (a, b, c, & d) and octanethiol SAM grown on the same Au (e, f, g & h).....	73
Figure 5.4 Representative AFM deflection images of residual nanoindentation impressions on Au (a, b, c, & d) and decanethiol SAM grown on the same Au (e, f, g and & h).....	74

Figure 5.5 Representative AFM deflection images of residual nanoindentation impressions on Au (a, b, c, & d) and dodecanethiol SAM grown on the same Au (e, f, g and & h).....	75
Figure 5.6 AFM 3-dimensional image of a 90 nm displacement controlled nanoindentation of Au and Deca/SAM grown of the same Au substrate.....	77
Figure 5.7 AFM 3-dimensional image of a 140 nm displacement controlled nanoindentation of Au and Deca/SAM grown of the same Au substrate.....	78
Figure 5.8 AFM 3-dimensional image of a 190 nm displacement controlled nanoindentation of Au and Deca/SAM grown of the same Au substrate.....	79
Figure 5.9 AFM 3-dimensional image of a 90 nm displacement controlled nanoindentation of Au and Dode/SAM grown of the same Au substrate.....	80
Figure 5.10 AFM 3-dimensional image of a 140 nm displacement controlled nanoindentation of and Dode/SAM grown of the same Au substrate.....	81
Figure 5.11 AFM 3-dimensional image of a 190 nm displacement controlled nanoindentation of Au and Dode/SAM grown of the same Au substrate.....	82
Figure 5.12 AFM cantilever deflection as a function of scanner displacement both in nanometers.....	83
Figure 5.13 Comparison between new surface areas created during indentation of plain gold and modified gold with SAMs.....	91
Figure 5.14 Comparison between maximum nanoindentation pile-up heights for (a) Octa/SAM, (b) Deca/SAM and (c) Dode/SAM compared to the pile-up height of their respective indented gold substrates.....	94

Figure 5.15 Geometrical figures utilized for contact area approximations from AFM nanoindentation residual impression.....	96
Figure 5.16 Partial scene of NanoScope TM Software showing sectioning analysis for measuring horizontal distances used for contact area approximations.....	97
Figure 5.17 Comparison of hardness approximations of gold and modified gold with SAM for (a) eight carbons SAM, (b) ten carbons SAM, and (c) twelve carbons SAM as a function of maximum nanoindentation displacements.....	101
Figure 5.18 Comparison of reduced elastic modulus approximations of gold and modified gold with SAM for (a) eight carbons SAM, (b) ten carbons SAM, and (c) twelve carbons SAM as a function of maximum nanoindentation displacements.....	104
Figure 5.19 Ratio of hardness to reduced elastic modulus as a function of the permanent work (plastic) divided by the total work of indentation.....	105

Chapter 6: Discussion and General Conclusions

Figure 6.1 Comparison between hardnesses computed using the true contact areas and hardnesses computed using Oliver and Pharr analysis for Octa/SAM, Deca/SAM and Dode/SAM and their respective gold substrates.....	109
Figure 6.2 Comparison between reduced elastic moduli computed using the true contact areas and using Oliver and Pharr analysis for Octa/SAM, Deca/SAM and Dode/SAM and their respective gold substrates.....	110
Figure 6.3 (a) Surface stress in gold surface. Surface atoms are strained, and the surface has a stress exerted on it by the underlying lattice. (b) Sketch showing a perpendicular	

cross section of the evaporated gold on glass and (c) the same surface under compressive surface stress caused by monolayer formation.....	117
Figure 6.4 Scheme distinguishing the pile-up and indent volume.....	118
Figure 6.5 Comparison between pile-up volumes created during nanoindentation of clean Au and modified Au with Octa/SAM, Deca/SAM and Dode/SAM.....	119
Figure 6.6 Three dimensional height profiles comparing the pile-up volume created during nanoindentation of clean Au (a, b, and c) and modified Au with Dode/SAM (d, e and f).....	120
 Chapter 7: Additional Work	
Figure 7.1 Raman spectrum of vinyl terminated SAM on evaporated gold film.....	125
Figure 7.2 Normalized Raman spectra showing bond dissociation of the 1640 shift/cm ⁻¹ (C=C stretching).....	126
Figure 7.3 AFM three dimensional images (2µm x 2µm) of vinyl terminated SAM kept in the dark during and same sample after 4minutes of UV light exposure (λ=368 nm)..	127
Figure 7.4 AFM height and three dimensional images of a vinyl terminated SAM on gold and the same area of the vinyl SAM after 2 minutes of in situ ultra violet (λ=254 nm) exposure.....	128
Figure 7.5 Saos-2 mineralization on polyarylate-coated coverslips and polycarbonate-coated coverslips	133
Figure 7.6 Photomicrograph of acetaminophen and sucrose crystal.....	137

1 INTRODUCTION

One of the most appealing and exciting ideas in the evolving field of nanotechnology is the concept of building structures from the bottom-up. Molecular assembly, layer by layer is industrially appealing because of its low cost and high throughput. These self-assembly based processes are expected to revolutionize the electronic, pharmaceutical and medical industry among others. However, the control of matter on the atomic and molecular scale is still a challenge. This is due to the chemical, physical and mechanical properties at the nanoscale exhibiting sometimes substantial differences when compared to the macro- and micro-scale.

Alkanethiol molecules are well known for their self organization properties and their ability to form a densely packed one molecule thick film on a gold surface. One of the main appeals of these alkanethiol self-assembled monolayers (SAMs) is the ability of the molecules to chemisorb to gold films by a covalent bond between the sulfur of the thiol head group and the gold atoms of the surface. Additionally, intermolecular van der Waal forces help the monolayer pack tightly thereby reducing its surface free energy. Gold surfaces covered with a SAM are environmentally inert and very stable due to the covalent binding to the surface. This makes the SAM an appealing lightweight protective coating. One of the advantages of alkanethiol SAMs is the simplicity by which the chemical and physical properties of the surface can be controlled by just varying the terminal group. The chemical functionality of a SAM/Au film can be controlled by varying the tail group, X, of the adsorbate, $\text{SH}-(\text{CH}_2)_n\text{X}$. Basically, any functional group compatible with thiols can be introduced subject only to two main constraints: that they do

not compete with the thiols as a head group; and that they do not react with the thiols. Since the discovery of SAMs the preparation of these molecular assemblies has attracted the attention of interfacial researchers interested in controlled wetting of surfaces, adhesion, friction, chemical sensing, and high resolution lithography. SAMs have also impacted the biomedical engineering field since they are compatible with cell culture conditions and are not toxic to the cells¹. Nanopattern studies using SAMs have been utilized to study cell behavior, since bioactive molecules covalently immobilized to the surface can control cell adhesion, growth, differentiation and migration by moderating the external chemical stimulation. This affects the synthesis of proteins and other small molecules by changing the cell's selective adsorption² and other cell level biosensors³.

Previous studies have also used SAMs to reduce or eliminate the effects of surface forces during nanoscale indentation test⁴. All these studies have shown the mechanical applications of this molecular assembly processes, however, little effort has gone into understanding how this nano-layer affects the mechanical properties of the underlying gold surface. SAMs terminated with non-polar groups have been previously showed to drastically decrease the surface free energy of the gold surface. But not only that, surface stresses are also modified by the presence of the SAM⁵⁻⁷. When a solid is elastically and plastically deformed, work is performed against both the volume and the surface, with the volume term the most dominant usually. However, in small structures a one molecule thick film can strongly affect and dominate the deformation of the underlying gold. The effect of surface chemistry on mechanics (plasticity) has been discussed by many groups, but nothing definitive has been shown^{8, 9, 10}.

The research discussed in this thesis is aimed at establishing how a SAM layer affects the mechanical properties of an underlying gold film during nanoindentation experiments. Comparisons are made between the chemical and mechanical behavior of glass control samples, gold films of (111) orientation on glass and the same Au(111) films modified with different chain length alkanethiol SAMs. The elastic and plastic response of the gold and SAM modified gold were investigated as a function of maximum nanoindenter tip displacement into the sample. Additionally, the residual nanoindentation impressions and areas of contact between the sample and tip were subsequently imaged with an atomic force microscope.

The observed dependence of mechanical properties on the SAM is explained by considering the role of surface energy, surface stress, intermolecular forces and strain-hardening. All of which can be modified by the addition of a SAM to the surface of the Au(111) film.

2 BACKGROUND

2.1 Elastic and Plastic Behavior of Metals

The elastic behavior of metals to an applied load is influenced fundamentally by the crystal structure and interatomic forces. In addition, the elastic movement of atoms is also influenced by the interaction between adjacent crystals of different orientations within polycrystalline metals.

The strain response and strength of a crystal is directly related to the density of atoms in the stacking layers. Atoms react with each other to stay in stable positions within the lattice array. The distance between the atoms results from the interatomic force. An attempt to move two atoms closer than their stable distance will give rise to very rapidly increasing repulsive forces, whereas any attempt to move atoms farther apart will give rise to attractive forces.

The interatomic elastic modulus is a measure of the rate of slope of the force curve in the immediate vicinity of the stable position, where stress (F/A) is proportional to strain (dl/l). Any distortion in the regularity of the lattice structure of metals will cause some weakening of the atomic bonds and therefore a lowering of the theoretical elastic limit.

If an applied force is large enough metals may eventually permanently deform. Many metals are considered to be very plastic; seeming to possess little elasticity. Plasticity in metals appears to be at its maximum when the presence of impurities in the lattice is least.

There are many types of defects in a crystal lattice and all can have an influence on the plastic behavior of the metal, but the main influence comes from a particular type of defect known as dislocations.

2.2 Dislocation Properties

Dislocations are the main cause of plastic deformation and can be considered as a line defect in a material's crystal structure. A dislocation is a mislinking of the lattice pattern along a complete row of atoms in a plane. The mislinking can be caused in two different ways; by an edge dislocation and a screw dislocation. An edge dislocation is caused by an extra part-plane of atoms in a crystal lattice causing the crystallographic plane to have an extra row of atoms on one side as shown in Figure 2.1a.

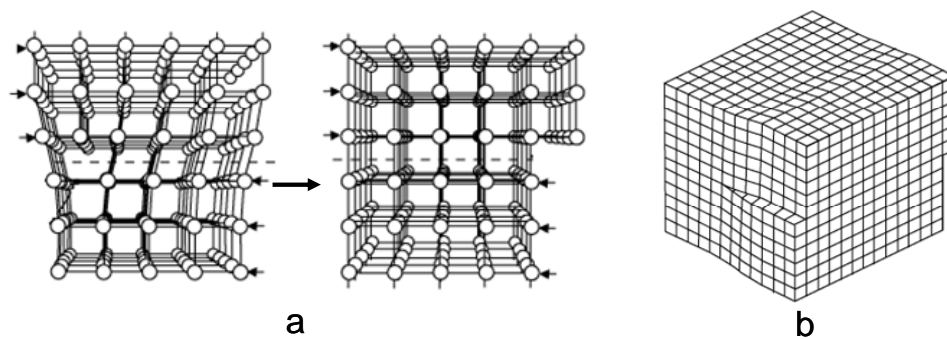


Figure 2.1 (a) Edge dislocation in a simple cubic lattice. Completion of movement of the edge dislocation leaving an atomic step. (b) A screw dislocation beginning at the side of a cubic crystal lattice. A step is left on each of the sides of the crystal at completion of the movement. (Adapted from W.D. Callister, John Wiley & Sons, Inc, 2000¹¹).

The presence of the edge dislocation induces tension to the part of the lattice under the edge dislocation and compression in the part above as the atoms try to adjust elastically. The linkage of the row of atoms forming the edge dislocation can transfer to

the right or left under the application of a stress. As long as the stress is applied it is possible to move the linkage of the dislocations from one atomic space to another towards the surface of the crystal. At the surface of the crystal the dislocation egresses leaving one atomic step.

A screw dislocation is when the atoms in one row are displaced one atomic space along the row by a shear stress applied in that direction. As shown in Figure 2.1b, continued application of the activating stress causes spread of the movement by progressive migration of the slip boundary through the crystal until it reaches the other side leaving an atomic step of opposite sign on each of the sides of the crystal¹².

2.2.1 Motion of Dislocations in Soft Metals

The motion of dislocations induces a change in the crystal shape. Two factors are important for dislocations to cause plastic flow; the energy needed to move the dislocation and the amount of plastic flow that is possible. The bonds in a dislocation are relatively weaker than the bonds between the regular crystal lattice. During plastic deformation dislocation bonds break first leading the crystal to lower its energy through the formation of new bonds between the dislocation and the next atomic row. In the case of a shear stress τ acting on a crystal with an edge dislocation, the force f on the dislocation can be calculated from the amount of work done by the applied stress. The force acting on an area ds of a dislocation segment dl that moves a distance dx under a stress tensor P is defined by dsP . The work done during dislocation migrations is $dW=(dsP) \cdot b$, because the area ds moves by b (burgers vector) with the dislocation migration. The force df on the dislocation element obtained from the work definition is:

$$df = (bP) \times dl \quad (2.1)$$

which is called the Peach-Köhler equation and is well described in the literature^{13, 14}.

The potential energy of the dislocations is called the Peierls potential. According to Peierls¹⁵ and Nabarro¹⁶, the Peierls force is the intrinsic lattice resistance to dislocation glide and it is influenced strongly by the periodicity of the crystal structure. The Peierls potential in fcc metals, such as gold, is very small compared to other materials. Dislocations in such soft metals move at speeds of a few ms^{-1} or more at the yield point. Such motion subjects the dislocations to strong frictional forces due to conduction electrons and lattice phonons¹³.

When a dislocation moves to the surface, the energy of the crystal changes (reduces usually) and thus the surface applies a force (attractive usually) on the dislocation. The force, which characterizes the interaction between the dislocation and the free surface is called the image force. In order to find the force exerted by a free surface on a dislocation it is necessary to calculate the self energy of the dislocation as a function of distance from the surface. For a simple case (Figure 2.2), a screw dislocation parallel to the free surface, a distance x from the surface, the elastic energy of the crystal is a function of the position of the dislocation, $U=U(x)$. The dependence of the energy on the position of the dislocation results in the image force whose magnitude is given by:

$$f = -\frac{\partial U}{\partial x} \quad (2.2)$$

where U denotes the potential energy of the field. The energy of the dislocation can be determined by the dislocation's total strain energy:

$$U(x) = \frac{\mu b^2}{4\pi} \ln \frac{2x}{r_0} \quad (2.3)$$

where r_0 is the core radius and μ is the shear or torsional modulus. From this, the stress σ_i that causes a force $\sigma_i b$ to act on a dislocation x from the surface is:

$$f = \sigma_i b = \frac{\mu b^2}{4\pi x} \quad (2.4)$$

This force is the image force and it plays an important role in strengthening of materials by strain hardening effect. The image force can get affected by the surface stress since it is dependent on the internal forces acting on the dislocation.

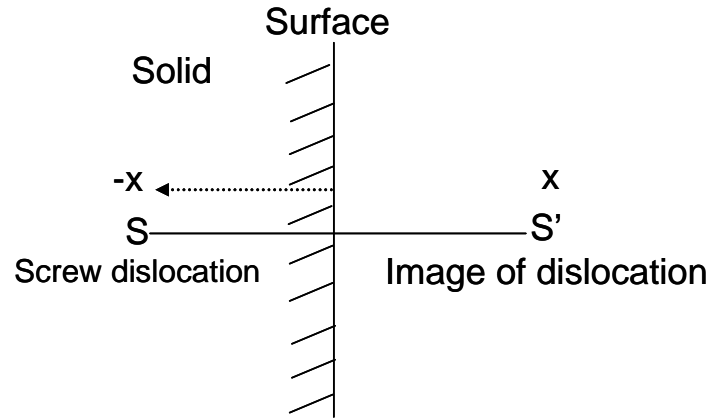


Figure 2.2 Screw dislocation and its image near a free surface¹⁷.

Fang et al¹⁸ studied the effect of surface stress on a screw dislocation. Their results showed that surface stress influences the motion of dislocations and an expression for the image force was obtained.

In summary, the periodic potential energy with respect to dislocation position is called the Peierls potential. Additionally, the motion of a dislocation in a finite perfect body is affected by the image force, which characterizes the interaction between the dislocation and the free surface. The solution of this problem is difficult and laborious.

Additional information and derivations can be found elsewhere¹⁹. The importance of image force will be discussed later with respect to the role of surface stress in plastic deformation.

2.3 Strain Hardening

Strain hardening, also known as work hardening, is the strengthening of a metal by dislocation multiplication. During plastic deformation the material becomes saturated with new dislocations. Too many dislocations leads to interactions between their respective strain fields which will prevent new dislocations from nucleating, creating a resistance to dislocation formation. A resistance to dislocation nucleation manifests as a resistance to plastic deformation thus a strengthening of the material is observed.

Dislocation multiplication occurs when a stress is large enough for a dislocation segment to become the source of new dislocations, a Frank-Read source. Dislocations when subjected to an external force can interact with each other and accumulate creating significant obstacles for their motion. Concentration of dislocations leads to an increase in the yield point of the material subsequently decreasing the ductility.

2.4 Surface Energy, Surface Stress and Interfacial Stress

The amount of reversible work dw performed to create new surface area dA for a liquid can be expressed by:

$$dw = \gamma dA \quad (2.5)$$

where γ is the surface free energy. In a solid new surface area created by plastic deformation can be treated in the same way. However, Gibbs²⁰ in 1906 pointed out that for solid surfaces there is a second quantity called the surface stress.

The distinction between the surface free energy (γ) and the surface stress (f) is perhaps one of the fundamental differences between a solid surface and a liquid. The reversible work per unit area involved in forming a new surface, which exposes new atoms, is the surface free energy. While, the surface stress is the reversible work per unit area required to elastically stretch a surface. The origin of the surface stress develops from the argument that the surface atoms exist in a lower electron density compared to the bulk atoms and as a consequence they adopt an equilibrium spacing different from the bulk. For the surfaces of clean metals, the atoms prefer to adopt a smaller equilibrium spacing than the bulk in order to increase the local electron density, this results in a surface tensile stress.

2.5 Gold

Gold is considered to be a relatively inert metal mainly because it does not form a stable oxide surface and it resists atmospheric contamination. Although gold compared with other metals is inert, toward chemisorption of O₂, CO, H₂O and hydrocarbons, a gold surface under ambient laboratory condition has a strong specific interaction with sulfur.

A widely used method employed to produce gold surfaces is the evaporation of gold onto flat substrates. This deposition process is conducted within a vacuum chamber capable of achieving pressures less than 10⁻⁵ Torr. A typical evaporator system passes an

electrical current through a metal target to heat it to a temperature where the source (gold in this particular case) material evaporates and deposits onto the substrates. Routinely used substrates include, silicon wafers, mica and glass as these materials are relatively flat. Gold prepared by evaporation at room temperature is polycrystalline and textured with a (111) orientation. Gold films prepared in this way do not contain many impurities or solute atoms in the lattice structure.

The unit cell of gold is face centered cubic (fcc). The face centered cubic structure has atoms located at each of the corners and the centers of all the cubic faces. The fcc structure allows the atoms to be packed closely. Metals that have a fcc structure are usually softer and have smaller Peierls forces compared with those with bcc structure.

Theoretical calculation of surface stress for gold involves calculating the surface free energy and its derivative with respect to elastic strain. A calculated surface stress energy of 1.51 J/m^2 and surface free energy of 0.79 J/m^2 for clean gold (111) was reported by Gumbsch²¹. Vermaak et al.²² measured the experimental surface stress of different metals, resulting in a value of 1.175 J/m^2 for gold.

2.6 Surface Free Energy

Measuring the contact angle is one of the most convenient methods for determining the surface free energy of solids. Contact angle relies on measuring the interaction between the solid under study and liquids with well defined surface tensions. Note that for liquids the surface free energy in J/m^2 is the same as the surface tension in N/m .

The equilibrium of forces at the edge of a resting drop (Figure 2.3) can be described by Young's equation²³:

$$\gamma_S = \gamma_{SL} + \gamma_L \cos \theta \quad (2.6)$$

where γ_S and γ_L are respectively the surface free energy of the solid and the surface tension of the measuring liquid, γ_{SL} is the solid-liquid interfacial free energy and θ the equilibrium contact angle between the solid and the measuring liquid.

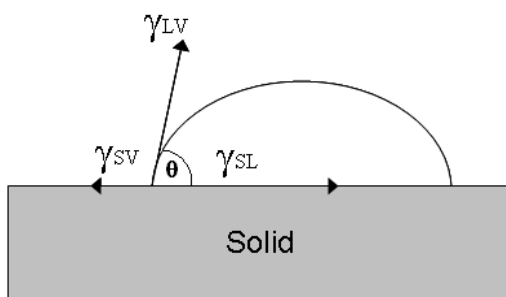


Figure 2.3 Scheme of a drop on the surface of a solid showing interactions described in Young's equation between a solid and liquid.

The quantities γ_L and θ are easily experimentally measured, but γ_{SL} remains unknown. In order to solve Young's equation different assumptions need to be made. One of the basic assumptions is that γ_{SL} is determined by various interfacial interactions that depend on the properties of both the solid and the measuring liquid. Fowkes²⁴ assumed that the surface free energy of a solid is the sum of the dispersion, polar, hydrogen, induction, and acid-base components.

2.6.1 The Owens-Wendt Method

The Owens-Wendt method²⁵ is one of many methods used for estimating the free surface energy of solids from contact angle measurements. In the Owens-Wendt method assumptions similar to those in Fowkes method were made. According to this method the interfacial tension can be divided into dispersive and polar interactions. Dispersive forces exist in all atoms and surfaces and are caused by time fluctuations of the charge distribution, and the polar forces contain Coulombic interactions between permanent and induced dipoles.

$$\gamma_S = \gamma_S^D + \gamma_S^P \quad (2.7)$$

$$\gamma_L = \gamma_L^D + \gamma_L^P \quad (2.8)$$

$$\gamma_{SL} = \gamma_S + \gamma_L - 2\left(\sqrt{\gamma_S^D \gamma_L^D} + \sqrt{\gamma_S^P \gamma_L^P}\right) \quad (2.9)$$

Substituting γ_{SL} in Young's equation results

$$\gamma_S = \gamma_S + \gamma_L - 2\left(\sqrt{\gamma_S^D \gamma_L^D} + \sqrt{\gamma_S^P \gamma_L^P}\right) + \gamma_L \cos \theta \quad (2.10)$$

Finally, the Owens-Wendt equation can be reduced as

$$1 + \gamma_L \cos \theta = 2\left(\sqrt{\gamma_S^D \cdot \gamma_L^D} + \sqrt{\gamma_S^P \cdot \gamma_L^P}\right) \quad (2.11)$$

This formula is one of the most common methods for calculating the surface free energy of solid ($\gamma_S = \gamma_S^D + \gamma_S^P$). For surface energy calculations contact angles from at least two measuring liquids with different surface tensions are needed. However, using at least three liquids is recommended.

2.7 Nanoindentation

Nanoindentation is an experimental technique used to measure the mechanical properties of a material. In nanoindentation usually a spherical or sharp diamond indenter is pressed into a material. During the experiment the force applied is recorded as a function of indentation displacement. Nanoindentation is similar to conventional hardness testing, but performed on a much smaller scale. The forces and displacements recorded are typically in the μN and nm ranges respectively.

When a nanoindentation test is performed a load versus displacement curve is obtained. Both load and displacement are recorded at each load increment. Following the application of the maximum load, the load is progressively removed and the displacement is recorded. On unloading, if yielding occurred, the load-displacement data follows a different curve to the loading until at zero applied load a residual impression is left in the specimen surface (Figure 2.4). To analyze the data classical contact mechanics solutions are commonly used^{26,27}. The maximum depth of penetration, jointly with the slope of the unloading curve measured as the tangent to the unloading data at maximum load, gives a measure of both the hardness and elastic modulus of the specimen²⁸. The analysis for extracting the mechanical properties from the load-displacement curves was originally proposed by Jean-Luc Loubet et al.²⁹ and later developed by Doerner and Nix³⁰, Oliver and Pharr³¹, and Field and Swain³².

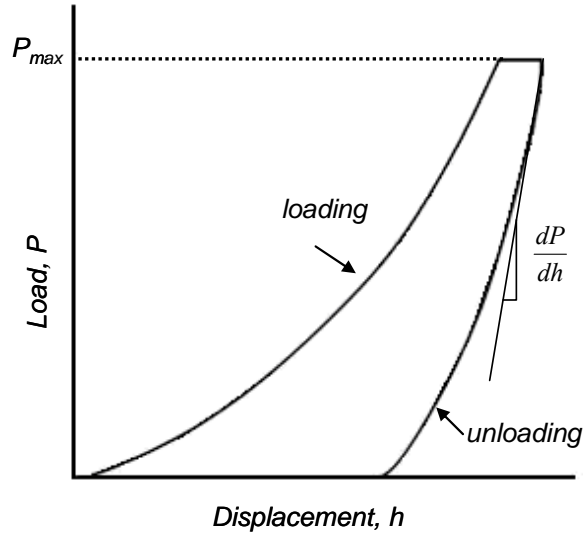


Figure 2.4 Typical nanoindentation curve.

2.7.1 Projected Area

A particularly meaningful quantity in indentation is the projected area of the contact. In nanoindentation the projected area of the contact is estimated from the plastic depth of penetration (h_p). The Berkovich indenter consists of a three sided pyramid. The projected area of the contacts for an ideal three sided pyramidal tip is given by:

$$A = 3\sqrt{3} h_p^2 \tan^2 \theta \quad (2.12)$$

for a Berkovich the semi-angle $\theta=65.27^\circ$. The depth of penetration, h_p , is related to the deformation of the material and the shape of the indenter by:

$$h_p = h_{\max} - \varepsilon \frac{P_{\max}}{S} \quad (2.13)$$

where h_{max} and P_{max} are the maximum tip displacement and load, ϵ is a geometric constant that accounts for the deflection of the surface at the contact perimeter, it is estimated as 0.75 by Oliver and Pharr and S , is the stiffness calculated from the slope (dP/dh) of the unloading curve. However, a perfect tip is impossible to achieve. To account for non-ideal geometry of the indenter it is necessary to apply a correction factor that is part of the instruments calibration. For this tip area calibration a series of indents at various contact depths on a calibration sample (fused quartz) of known elastic modulus are performed to fit a six order polynomial function of the form:

$$A = C_0 h_p^2 + C_1 h_p + C_2 h_p^{1/2} + C_3 h_p^{1/4} + C_4 h_p^{1/8} + C_5 h_p^{1/16} \quad (2.14)$$

where $C_0=24.5$; $C_1=1.66 \times 10^4$; $C_2=-6.67 \times 10^4$; $C_3=5.08 \times 10^6$; $C_4=-1.08 \times 10^6$; $C_5=6.31 \times 10^6$. However, the constants in the area function change with time. A schematic of a cross-sectional area of an indent illustrating the quantities h_{max} , h_p , and P all used for the analysis is shown in Figure 2.5.

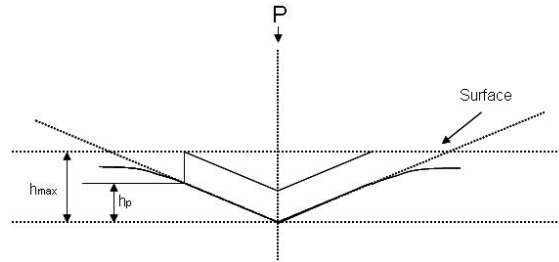


Figure 2.5 Schematic of an indentation showing quantity h_p used for analysis of the projected area.

2.8 Contact Mechanics and Adhesive Forces

During nanoindentation a tip is brought into contact with the material's surface to measure mechanical properties such as elastic modulus and hardness. While Classical

Mechanics ignores effects at the atomic scale, Contact Mechanics considers surface and geometrical constraints. It is well known that geometry of the indenter tip affects the local elastic deformation³³. One of the first theories that relate the circular contact area of a sphere with a plane, or more general between two spheres, to the elastic properties of the material is the Hertz Theory of Elastic Deformation^{34, 35}. However, Hertz theory does not take into account van der Waal forces, friction and adhesion.

When the indenter tip is in contact with the surface, even at zero loads, there is an effect from adhesive forces²⁷. In 1970 Hertz's theory was adapted by Johnson et al. with the JKR theory³⁶. The JKR (Johnson, Kendall and Roberts) model considers the contact to be adhesive and assumes the formation of a capillary neck. The combined surface and elastic free energy is then minimized to find the contact radius. A more involved theory commonly used to account for adhesive interactions is the DMT (Derjaguin, Muller and Toporov)³⁷ model. The DMT model assumes a rigid contact under the influence of van der Waal forces acting outside the elastic contact which gives rise to an additional force. The difference between the JKR and the DMT models lies in the assumption of adhesive force acting inside or outside the contact area. A more simplified DMT theory is Bradley's theory³⁸. In Bradley's model the two surfaces are significantly apart and any elastic deformation due to attractive forces is neglected. In summary, the Hertz, JKR and DMT assume fully elastic contacts. The JKR considers adhesion in the contact zone by the formation of a capillary neck whereas the DMT includes long range van der Waals forces operating outside the contact area, and finally the Bradley's model assumes a rigid surface under purely van der Waals forces.

Selecting the contact mechanics model to interpret nanoindentation data is not always easy. Commonly the JKR model is more appropriate for softer materials with high surface energy while the DMT applies better for hard materials with low surface energy. However, this generalization can often not work well when describing each peculiar surface-tip interaction and mistakes can be made³⁹. Additionally, these theories do not take account of time dependent effects.

Tabor⁴⁰ later proposed that the two theories, JKR and DMT, represents the opposite extremes of a dimensionless parameter μ given by:

$$\mu = \left(\frac{4 R \gamma^2}{E^2 z_0^3} \right)^{1/3} \quad (2.15)$$

where z_0 is the equilibrium atomic spacing in the Lennard-Jones potential⁴¹, R is the relative radii of curvature, γ is the surface free energy and E is the reduced modulus. The JKR theory is more applicable for large radius ($\mu > 5$) whereas the DMT theory applies to small rigid solids ($\mu < 0.1$).

2.9 Self-Assembled Monolayers

Self-assembled monolayers (SAMs) are ordered molecular assemblies formed by the spontaneous adsorption of amphiphilic molecules onto hydrophilic surfaces usually by the immersion of a substrate into a solution of an active surfactant. A surfactant (surface active agent) molecule has a hydrophilic (water-loving) head and a hydrophobic (oil-loving or water-hating) tail. The production of SAMs can be traced back to 1946 when Zisman et al.⁴² found that certain types of polar organic molecules are adsorbed from solutions in non-polar solvents to form well-oriented monolayers on solid surfaces.

Zisman's group found that by exposing glass and a variety of metallic and non-metallic solid surfaces to a dilute solution of long-chained alcohols in hexadecane and a variety of solvents, ranging from, mineral oils, benzene, methylnaphthalene and dicyclohexyl to other solvents such as carbon disulfide, carbon tetrachloride, bromobenzene and diphenyloxide, an adsorbed film was attached to the surface through the polar group. Zisman's films were nearly close-packed and formed approximately vertically oriented molecules. In 1983, Nuzzo and Allara⁴³ published an extension to Zisman et al's approach, showing that disulfides form oriented monolayers on gold surfaces, and exposed both high- and low-energy surfaces, depending on the tail group present. Later the same was found for sulfides⁴⁴ and thiols⁴⁵. SAMs can be prepared using different types of molecules and different substrates. Self-assembled monolayers of alkanethiols $[\text{CH}_3(\text{CH}_2)_{n-1}\text{SH}]$ on Au(111) is one of the most widely studied and used systems. Alkanes, are chemical compounds that consist only of the elements carbon and hydrogen, wherein these atoms are linked together exclusively by single bonds. Each carbon atom must have 4 bonds (either C-H or C-C bonds), and each hydrogen atom must be joined to a carbon atom (H-C bonds). Thiol, is a compound that contains the functional group composed of a sulfur atom and a hydrogen atom (-SH).

2.9.1 Alkanethiol Self-Assembly Kinetics

The adsorption of alkanethiols onto gold is the most frequently studied system due to the relative inertness of the gold. The kinetics of the alkanethiol adsorption onto Au has been previously studied⁴⁶. Usually the monolayer is deposited onto the surface from a low concentration solution. The initial step is the adsorption, which is strongly dependent of thiol concentration. In essence, an alkane chain with a thiol head group

adsorbs onto the gold forming the monolayer. It has been shown that the S-H bond cleaves and the molecules chemisorb to the surface through a covalent Au-S bond⁴⁵. Sulfur has particular affinity for gold, with a binding energy in the range of 20–35 kcal/mol (85–145 kJ/mol). The second step is the surface crystallization, basically the hydrocarbon chains pass from a disordered state into unit cell forming 2-dimensional crystals. The hydrocarbon chains (alkyl chains) interact by packing together due to van der Waals forces with a strong lateral interaction of 4-8 kJ/mol per CH₂⁴⁷. The alkyl chains are close-packed and are normally oriented ~30 degrees from the normal⁴⁸. Electron diffraction pattern have shown that the monolayer adopts the commensurate $(\sqrt{3} \times \sqrt{3})R30^\circ$ overlayer lattice⁴⁹ configuration of the hexagonal closed-packed Au(111). Self-assembling systems of alkanethiols that terminate in nonpolar groups produce a lower-energy surface. Due to the low surface energies, high hydrophobicity, and compact packing structures, SAMs usually have low adhesion and friction. These features make SAMs excellent boundary lubricants in micro-electric and micro-mechanical systems^{50,51}. Once the SAM is prepared longchain alkanethiols do not desorb and are stable in air at room temperature².

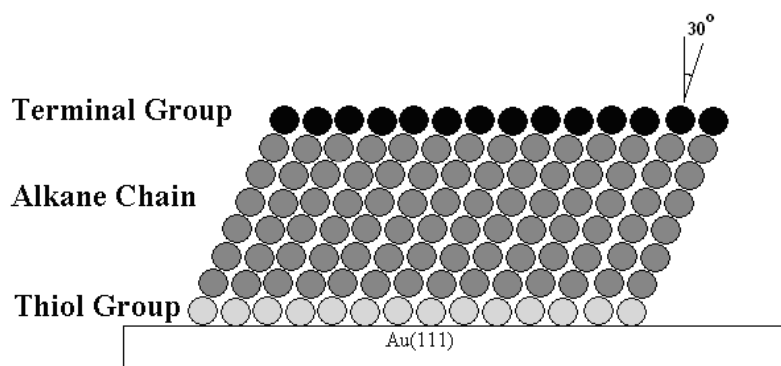


Figure 2.6 Schematic diagram of alkanethiol on Au(111) monolayer. The alkyl chains are packed with nearly crystalline densities and are oriented ~ 30 degrees. The terminal group determines the interfacial characteristics of the surface.

Different functional terminal groups, such as a methyl group, carboxyl group or amine group can be introduced by an ω -substituted alkanethiol. The interfacial properties of the film surface are mostly determined by the chemical and physical properties of the terminal group.

The adsorption of thiols to form densely packed, oriented monolayers is not limited to gold surfaces. The formation of chemisorbed molecular films also occurs on silver, copper⁴⁸, mercury⁵², GaAs⁵³, and InP⁵⁴ surfaces and silicon/silica as well.

2.9.2 Physisorption and Chemisorption

Physisorption is a physical adsorption where the forces are intermolecular (van der Waals), and in which there is not a significant change in the electronic orbital patterns. In contrast, chemisorption, is an adsorption which results from a chemical bond, thus there is a strong interaction between the substrate and the adsorbant.

Alkanethiol molecules have the ability to both chemisorb through the sulfur atom and physisorb through van de Waals interactions. The strong lateral interaction occurring from the van der Waals forces between the hydrocarbon chains is one of the principal factors for self-assembly. As mentioned before the quantity of this force is controlled by the length of the chain (4-8 kJ/mol per CH₂).

A recent study quantified the rate of chemisorption from a physisorbed precursor state. Hydrocarbon desorption temperature from the physisorbed state was showed to increase linearly with chain length. This result shows that as the chain length of the alkane chain increases the physisorption energy also increases.

While the interactions between alkane chains are relatively well understood the specific sulfur-gold interaction is still under debate. SAM chemisorption occurs through a chemical bond and because of this chain length is not expected to significantly affect the desorption enthalpy of the S-Au.

2.9.3 Self-Assembled Monolayers Applications

From their discovery the preparation of these molecular assemblies attracted the attention of interfacial researchers interested in controlling wetting^{48,55}, adhesion⁵⁶, friction⁵⁷, chemical sensing⁵⁸, and high resolution lithography⁵⁹. With the advances in nanotechnology and biomedical engineering new applications for gold-alkylthiolate SAMs have emerged. SAMs are used in micro- and nano-electronics; as a lubricant for microelectromechanical systems⁵¹; for molecular recognition (biosensors)⁶⁰; and as biomembranes⁶¹ in studies of biomolecules at surfaces.

2.9.4 Characterization of the Monolayer

When studying monolayers it is important to know both their surface and bulk properties. Ellipsometry is often used to measure the thickness and uniformity of the prepared SAMs by measuring the optical response. Contact angle measurements with different liquids are used to evaluate the wetting properties, surface free energy and uniformity. Fourier transformation infrared spectroscopy (FTIR) is used to learn about the direction of transition dipoles and to evaluate molecular orientation and packing. Also, surface measurements like electron spectroscopy for chemical analysis (ESCA)⁶², Raman and FTIR can be used to study surface composition. In addition, plasmon resonance spectroscopy (SPR) is an in situ technique that can be used to measure changes in the refractive index of a monolayer attached to a metal surface. SPR can detect the adsorption and association of thiols onto gold to form the monolayer. Nanoindentation techniques can be used to measure the effect of the monolayer on mechanical properties of the underlying metal substrate. Finally, but no less important, atomic force microscope (AFM) can be used to look at the surface topography and roughness.

3 PHYSICAL AND CHEMICAL CHARACTERIZATION OF ALKANETHIOL SELF-ASSEMBLED MONOLAYERS ON GOLD(111)

3.1 Materials

3.1.1 Substrate Preparation

Self-assembled monolayers of alkanethiols are formed by alkanethiol molecules chemisorbed on gold surfaces through the thiol head-group. The preferred crystal face for alkanethiolate SAM preparation on Au substrates is the (111) direction, which can be obtained by evaporation of a thin gold film onto a flat glass substrate. Gold is the most commonly used material as a substrate. Unlike other materials, gold is a relatively inert metal: it does not form a stable oxide surface and it resists atmospheric contamination. In addition, gold has a strong specific interaction with sulfur that allows it to form monolayers in the presence of many others functional groups.

Microscope glass coverslips (thickness: 0.137 mm) were cleaned by sonication into acetone, methanol, ethanol and distilled water consecutively for 10 minutes. Cleaned glass samples were blown dried using pure Nitrogen. Highly pure gold pellets (99.99 % pure, Kurt J. Lesker Co) were used for evaporation. Evaporation processes were performed using an Edwards E306A evaporator under a vacuum of $\sim 5 \times 10^{-6}$ Torr and an e-beam evaporator from the physics department at Rutgers. Film thicknesses were monitored with a quartz crystal thickness monitor. After deposition the coated samples were rinsed in ethanol solutions. The gold substrates can be handled with few

precautions and do not require specialized facilities such as clean rooms. For example, weakly adsorbed material to gold samples exposed to organic contaminants found in typical laboratories will be later displaced by the thiols during self-assembly of the SAM⁶³. Finally, the samples were glued to magnetic metal stubs using cyanoacrylate glue (super glue). Mounting the samples onto the metal stubs was obligatory since both the nanoindenter and AFM require a stable and magnetically attached surface.

3.1.2 Deposition of Self-Assembled Monolayers

Commercially available 10-carboxy-1-decanethiol, 97.6% ($C_{11}H_{22}O_2S$) and 11-amino-1-undecanethiol, hydrochloride, 94.6% ($C_{11}H_{26}ClNS$) were obtained from Dojindo Laboratories with melting points of 46-50 °C and 154-163 °C respectively. These functionalized molecules were not used for mechanical studies later. 1-decanethiol, 96% ($CH_3(CH_2)_9-SH$), 1-octanethiol, 98.5% ($CH_3(CH_2)_7-SH$) and 1-dodecanethiol, 98% ($CH_3(CH_2)_{11}-SH$) were obtained from Sigma-Aldrich with densities of 0.841 g/mL, 0.843 g/mL, and 0.845 g/mL respectively. To build up the monolayer 2 mM solutions of ethanolic alkanethiol were freshly prepared before each experiment. A large drop of the solution was applied to the evaporated Au(111) substrates in such a way that the entire surface was covered with the solution. This part of the process was introduced to replace the substrate being immersed into the ethanolic solution. This was necessary since it was noticed that long immersion of the substrates into the ethanolic solutions was dissolving part of the cyanoacrylate glue used to mount the samples onto the metal stubs. Monolayer adsorptions were carried out in well covered clean weighing bottles (30 x 60 mm, 50 mL). Even though the monolayer forms very rapidly, it is

necessary to wait between 19 to 24 hours to obtain well-ordered monolayers. After monolayers formation samples were rinsed with ethanol to wash off the excess.

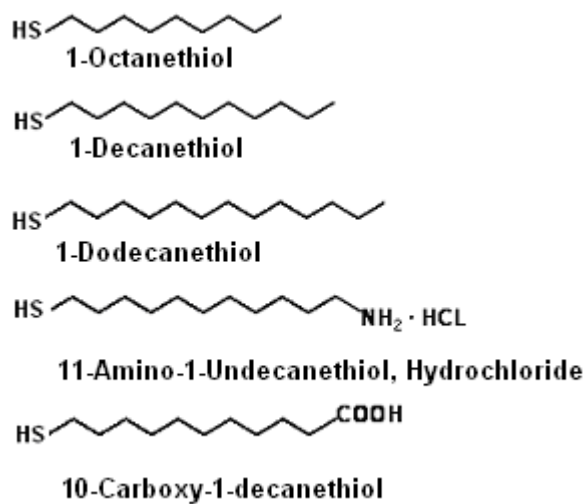


Figure 3.1 n-alkanethiol, carboxyalkanethiols and aminoalkanethiol chemical structure.

3.2 X-Ray Diffraction

The preferred crystal face for alkanethiolates on Au substrates is the Au(111) direction. The freshly prepared gold-coated substrates were characterized by X-ray diffraction (Siemens Kristalloflex Diffractometer, Cu K_α radiation) to confirm the preferred gold crystal's orientation.

3.2.1 Experimental Methods

Evaporated gold on glass samples were attached to the X-ray diffraction (XRD) sample holder using clay. Data was collected over 2θ values ranging from 20° to 90° with steps of 0.05° .

3.2.2 Results and Conclusions

Figure 3.2 shows the X-ray diffraction pattern of an evaporated Au film (~ 20 nm, measured with ellipsometry) on a glass slide. A strong peak centered at a value of 2θ of 38.55° confirmed that the dominant orientation of the Au film is the (111).

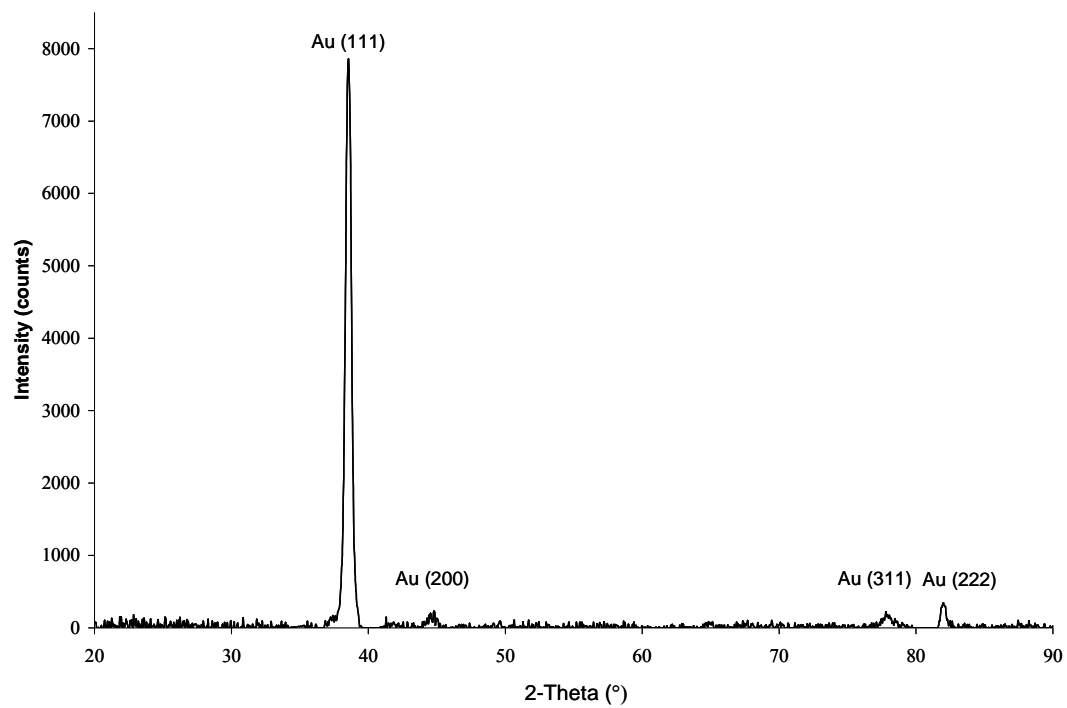


Figure 3.2 X-ray diffraction pattern of a 20 nm Au film evaporated onto a glass slide.

3.3 AFM on Gold (111)

The morphology of the gold surfaces produced by evaporation was observed with AFM. Analysis of the gold surface images revealed monatomic steps, a feature characteristic of the (111) orientation. Figure 3.3 is a deflection AFM image of the Au(111) surface produced by evaporation onto a glass coverslip substrate. AFM image analysis revealed average grain size of 30 nm and steps of 1 nm. The gold surface is not atomically smooth, but rather shows variations of the thickness which results from the polycrystalline nature of the film. The mean roughness measured by AFM was found to be 0.134 nm. These results are in agreement with previous AFM⁶⁴ and SEM⁴⁵ morphology characterization work on gold films prepared by evaporation.

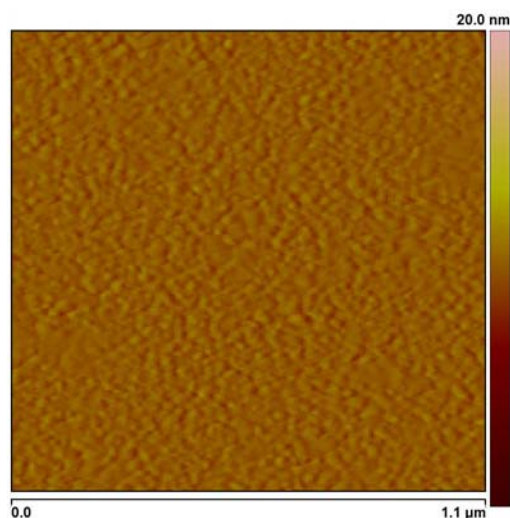


Figure 3.3 AFM deflection image of gold surface prepared by evaporation of gold onto a glass coverslip.

The thickness of the gold film was also measured using AFM imaging. The resulting thickness for sample L4 was ~20 nm, as shown in the section analysis in Figure 3.4.

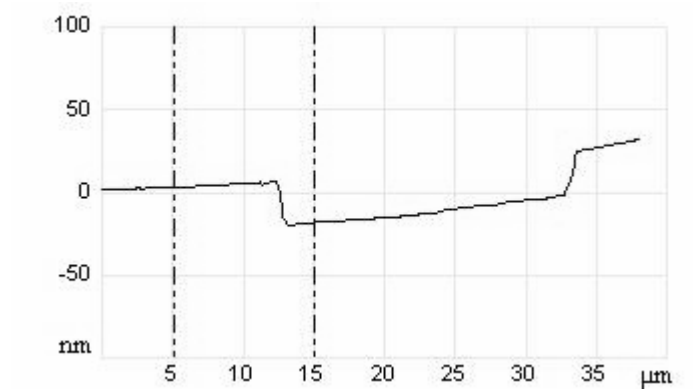


Figure 3.4 AFM section analysis showing gold film thickness by cross-sectional profile.

3.4 Ellipsometry

Ellipsometry was used to characterize the monolayer, confirm the presence of the adsorbed 1-decanethiol molecules on the surface, and measure the thickness and uniformity of the freshly prepared films. Ellipsometry is a common optical technique used for the determination of the thickness and refractive angle of thin homogenous films. This technique was used before and after SAM formation to detect adsorption of molecules onto the Au. Some of the advantages of ellipsometry over other techniques are: it is a non-destructive technique; it is fast; it is very sensitive; and it is a highly reliable tool for characterizing thin film structures.

Ellipsometry is an optical non-destructive technique that uses polarized light to probe the dielectric properties of a sample. Ellipsometry measures the change in the polarization state of the incident and reflected light waves due to its interaction with the sample under study. This change is usually described by two angles (Ψ) and (Δ), shown in Figure 3.5, that represents the amplitude ratio and phase difference between p- and s-polarizations. The indices “p” and “s” stand for light polarized parallel and perpendicular to the plane of incidence; and the incident vectors are defined by E_{ip} and E_{is} (Figure 3.5). The exact nature of the polarization change is determined by the sample's properties such as thickness and refractive index.

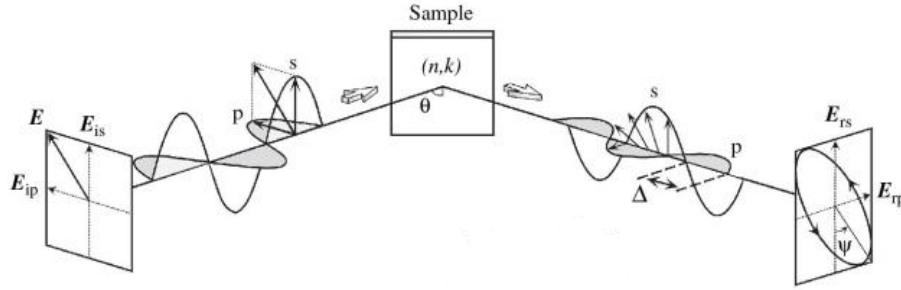


Figure 3.5 Basic principles of ellipsometry⁶⁵.

When a sample structure is simple, the amplitude ratio (Ψ) is characterized by the refractive index (n), while Δ represents light adsorption described by the extinction coefficient (k). The two measured angles (Ψ) and (Δ) express the ratio of the amplitude reflection coefficients (r_p) and (r_s) of the sample. The name "ellipsometry" comes from the fact that the most general state of polarization is elliptic. The fundamental equation of ellipsometry is described by:

$$\tan \Psi \exp(i\Delta) \equiv \frac{r_p}{r_s} \quad (3.1)$$

3.4.1 Experimental Methods

Ellipsometry measurements were made on a Horiba Jobin Yvon Ellipsometer. All the measurements were done under air and room temperature using wavelengths of 250-800 nm and an incident angle of 70° . Samples were washed briefly with ethanol and blown dry with nitrogen before the measurements were taken. Six separate points were measured on each sample by constructing a spiral-map model. Ellipsometry readings were averaged and plotted using Microsoft Excel. Measurements were taken on the clean gold and after monolayer formation. In order to transform the ellipsometric

measurements into film thickness a model has to be chosen. The samples were taken to be like three flat parallel layers of thickness 'd' made of SiO₂, Au, and CH₃-(CH₂)₉SH with a refractive index of 1.45. In this model all layers are considered to be of homogeneous composition.

3.4.2 Results and Conclusions

Ellipsometry measurements done on three clean gold films deposited onto glass by vapor deposition revealed average thicknesses of the gold coatings of 45 nm, 20 nm and 25 nm. The average thickness of the decanethiol monolayer was 0.809 nm which agrees with previous studies of kinetics and film formation of n-alkanethiols SAMs on gold surfaces ⁴⁶. Ellipsometry measurements confirm that the surface was covered by decanethiol molecules adsorbed onto gold.

3.5 Raman Spectroscopy

Raman spectroscopy is an optical, laser based characterization tool that measures the vibration spectra of materials. The spectrum is sensitive to the length, strengths, and arrangement of bonds in a material as well as the chemical composition. The technique is named after the Indian scientist Sir Chandrasekhara Venkata Raman who discovered the phenomenon in 1928. The Raman effect is based on the principle that when a material is exposed to monochromatic light most photons are elastically scattered (Rayleigh scattering) such that the scattered photons have the same energy as the incident beam. However, a tiny fraction of the light (~ 1 in 10 million) exchange energy with the molecules or atoms, exciting vibrational modes and thus the light is scattered with a different energy. Raman scattering is a form of inelastic scattering of photons, so the wavelength of the Raman scattered wave is different from that of the incident light. For a given incident wavelength there will be a Stokes and an anti-Stokes Raman signal. Stokes scattering results when the molecules in the material under study absorb energy from the photons. The resulting scattered photons are shifted to the red side of the incident spectrum meaning they have lower energy. On the other hand, when molecules (due to thermal energy) are in an excited state, transfer of energy to the scattered photons can occur. When molecules lose energy anti-Stokes scattering occurs. In anti-Stokes the resulting photons are shifted to the blue side of the spectrum. Both shifts are possible because when light interacts with matter the absorption or emission of light of the same precise matching energy difference with the incident photons is allowed. Raman spectroscopy usually relies on the analysis of the Stokes lines. Anti-Stokes lines are less intense than Stokes because only molecules that are vibrationally excited prior to

radiation can give rise to anti-Stokes and at room temperature the number of molecules in an excited vibrational state is generally very small.

3.5.1 Raman Basic Theory

The Raman spectrum arises from a coupling of the incident high frequency radiation with the electron clouds that make up a chemical bond. The electric field of the incident radiation distorts the electron cloud in the sample, storing some energy. The electric field strength (E) of the electromagnetic wave from the laser fluctuates with time (t) as described in the following equation:

$$E = E_0 \cos 2\pi \nu_0 t \quad (3.2)$$

where E_0 is the vibrational amplitude and ν_0 is the frequency of the laser. When a molecule is irradiated by this light inducement of the electric dipole moment (P) occurs:

$$P = \alpha E = \alpha E_0 \cos 2\pi \nu_0 t \quad (3.3)$$

where α is a proportionality constant commonly called polarizability. When the field reverses as the wave passes, the distorted clouds relax and the stored energy is re-radiated. A small portion of the stored energy is occasionally transferred to the sample itself, exciting the vibrational modes of the bond⁶⁶. A diagram showing the electronic transitions accompanying Raman and Rayleigh scattering is shown in Figure 3.6.

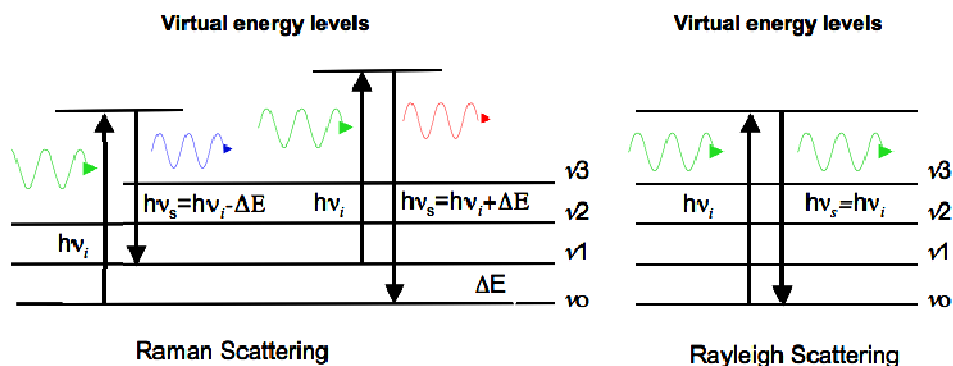


Figure 3.6 Electronic transitions accompanying Raman (left) and Rayleigh (right) scattering.

Some of the advantages of micro-Raman spectroscopy are: the micro-scale resolution; is a non-destructive technique; provides chemical and structural information in only a few seconds; and it is sensitive to self-assembled monolayers.

3.5.2 Surface-Enhanced Raman Spectroscopy (SERS)

SERS is the enhancement of Raman scattering of molecules physisorbed or chemisorbed on metal particles or surface. Because of the large enhancement small sample volumes can be analyzed. Scattering intensity from adsorbed molecules onto metals can be several orders of magnitude stronger than that of non-adsorbed molecules, which allows the technique to be sensitive enough to detect single molecules. The Raman enhancement is possible because of metallic substrates or nanoparticles. The metallic substrate surface is extremely important for Raman enhancement. The exact enhancement mechanism is still under debate, but it is clear that any enhancement must come from an enhancement in molecular polarizability (α) or from the electric field (E).

One of the proposed enhancement mechanisms occurs when the light incident at the surface of the metal excites conduction electrons and generates a surface plasma resonance causing the roughness features of the metal to be polarized and the electromagnetic field in the interiors of the particles at the surface to increase from the incident field. The second theory states that the enhancement can result from a charge transfer or bond formation between the metal and adsorbate which can increase the molecular polarizability (α).

Gold and silver are typically the metal of choice for SERS because their plasmon resonance frequencies fall within the visible and near-infrared radiation commonly used to excite the Raman modes of vibration. Other metals whose adsorptions falls within the range for SERS experiments are platinum, copper and palladium. Detail information about surface-enhanced Raman can be found elsewhere⁶⁷

3.5.3 Experimental Methods

To confirm the adsorption of the alkenthiol molecules onto the Au(111) substrates Raman Spectroscopy was performed. Enhancement of the signal was obtained by virtue of surface enhancement by the underlying metallic substrate.

Raman measurements were performed using a Renishaw *inVia* micro-Raman spectrometer coupled to a Leica microscope and equipped with a 785 nm diode laser with ~300 mW power output at the laser head. A 785 nm edge laser in regular mode was focused on each point using the Leica microscope with a 50X/0.75 NA objective. A silicon wafer was used to calibrate the spectrometer by focusing on the 520 shift/cm⁻¹. Measurements over the spectral range of 100 to 3200 Raman shift/cm⁻¹ were conducted

using a 1200 I/mm (633/780) grating and a 10 seconds exposure time. Three accumulations were performed at each scanned point on the sample. All the samples were tested under room temperature using 10% of the laser. Raman spectra were processed with the Renishaw Wire 2.0 Service Pack 9 software. To yield spectra with flat baselines, background subtraction was performed by carefully adding points manually below the spectra and using the cubic spline interpolation method.

3.5.4 Results and Conclusions

Figure 3.7 presents the Raman spectra of four different samples; Au film deposited onto glass (red), 1-decanethiol monolayer grown on Au (green), 11-amino-1-undecanethiol monolayer grown on Au (blue), and 10-carboxy-1-decanethiol grown on Au (black).

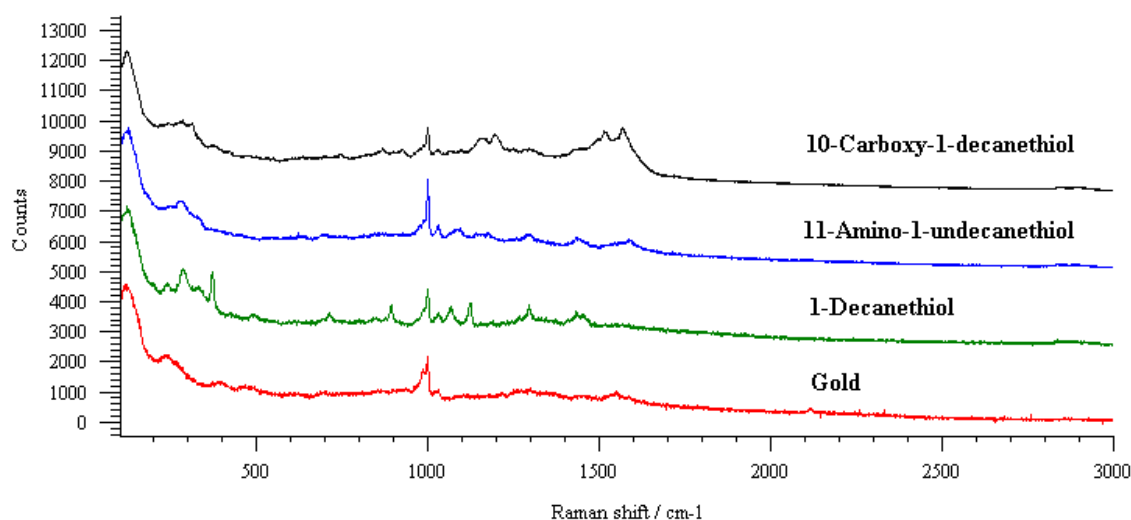


Figure 3.7 Raman spectra at room temperature of Au (red), 1-decanethiol monolayer grown on Au (green), 11-amino-1-undecanethiol monolayer grown on Au (blue), and 10-carboxy-1-decanethiol grown on Au (black).

Figure 3.8 shows two Raman spectra corresponding to a film of evaporated Au and a 1-decanethiol SAM on Au(111). Peak assignments are shown in

Table 3.1. The positions of these Raman peaks are in agreement with previous studies of alkanethiol monolayers on Au. The peaks at 1432 cm^{-1} , 1293 cm^{-1} , and 708 cm^{-1} correspond to the CH_2 scissor, twist-rock and rock-twist vibrations respectively. The peak at 1064 cm^{-1} represents the C-C stretch and at 889 cm^{-1} the CH_3 rock vibration. The peak positioned at 367 cm^{-1} have been previously attributed to a S-S bond⁶⁸. These peaks confirmed the presence of a well ordered SAM layer on the Au.

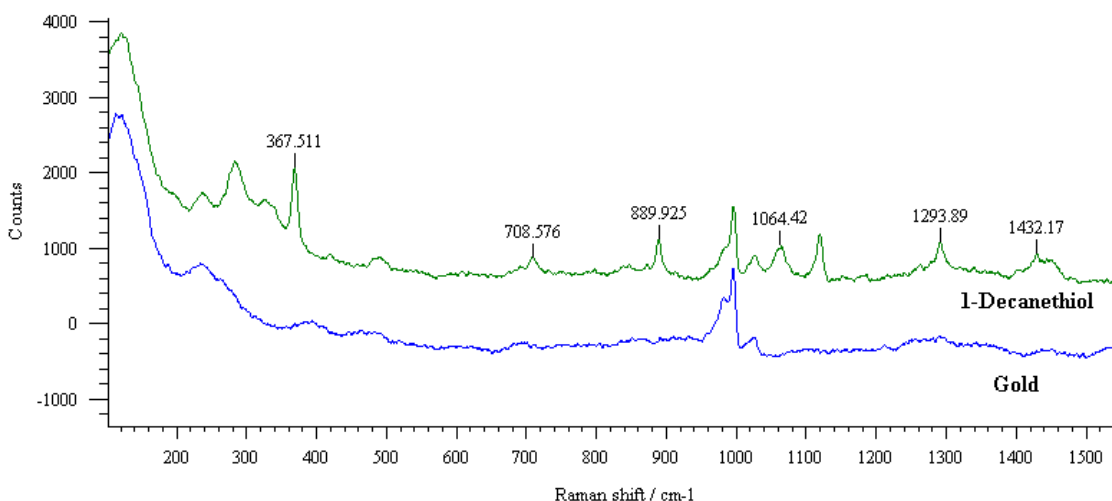


Figure 3.8 Raman spectra of Au film (blue) and a 1-decanethiol SAM adsorbed on a thin layer of Au (green).

Table 3.1 Raman peak assignments for decanethiol monolayer on Au(111). *Values taken from literature⁶⁸.

Peak position (cm^{-1})	Mode assignment	Reference value (cm^{-1})
1432	CH_2 scissor	1450^*
1293	CH_2 twist-rock	1280^*
1064	C-C stretch	1050^*
889	CH_3 rock	880^*
708	CH_2 rock-twist	720^*
367	S-S-C bend	370^*

3.6 Determination of Surface Energy by Contact Angle Measurements

3.6.1 Experimental Methods

The static contact angles of glass substrates, evaporated Au(111) on glass and various SAMs (octanethiol, dodecanethiol) on Au(111) were measured using three different relevant solvents. A Ramé-Hart (Netcong, NJ) goniometer at room temperature with no control ambient humidity and the DropImage Advance Software were used to record and analyze the drops. Three different liquids; water, ethylene glycol and glycerol were used as measuring liquids. Their respective surface tension values (Table 3.2) were adopted from DSA surface tension database (DSA1 v 1.80, Kruss, Germany). Four 2 μ L droplets from each liquid were dispensed with a micropipette and each droplet was measured on each sample six times and then averaged. Contact angles were measured by fitting a mathematical expression to the shape of the drop and then calculating the slope of the tangent to the drop at the liquid-solid-vapor interface.

Table 3.2 Surface tension data of the applied measuring liquids against air. Values adopted from DSA surface tension database

Solvent liquid	Dispersion tension (mJ/m²)	Polar tension (mJ/m²)	Total Surface Tension (mJ/m²)
Water	21.8	51	72.8
Ethylene Glycol	29	19	48
Glycerol	37	26.4	63.4

3.6.2 Results and Conclusions

The contact angle values of the various liquids for the different SAMs, glass and Au(111) are summarized in Table 3.3.

Table 3.3. Overview of the measured contact angles.

	Glass	Au(111)	Octanethiol SAM	Dodecanethiol SAM
Water	69.22°	79.37°	95.19°	87.00°
Ethylene Glycol	49.27°	53.61°	74.46°	77.13°
Glycerol	62.10°	72.07°	86.30°	74.18°

The surface energy, both the polar and the dispersive component, were extracted using the Owens-Wendt method. By arranging equation 2.11 in Section 2.6.1 it is possible to obtain an equation of a straight line with the $y=mx+b$ form.

$$\frac{1 + \cos \theta}{2\sqrt{\gamma_L^D}} \cdot \gamma_L = \sqrt{\gamma_S^P} \cdot \sqrt{\frac{\gamma_L^P}{\gamma_L^D}} + \sqrt{\gamma_S^D} \quad (3.4)$$

To calculate γ_S^D and γ_S^P , y versus x were plotted. The sum of γ_S^D and γ_S^P gives the value of the surface free energy.

The surface energies with their respective disperse and polar components in mJ/m^2 for the different substrates calculated according to the Owens-Wendt method are summarized in Table 3.4.

Table 3.4 Surface energies with their respective disperse and polar components.

	Dispersion (mJ/m^2)	Polar (mJ/m^2)	Surface Energy (mJ/m^2)
Glass	15.24	18.97	34.21
Au(111)	18.51	10.36	28.87
Octa/SAM	11.80	9.83	21.63
Dode/SAM	14.85	4.47	19.32

The wettability of the samples was quantified through the measurement of water contact angle. When the measuring liquid is water the surface can be classified as hydrophilic, contact angle $<90^\circ$, or hydrophobic, contact angle $>90^\circ$. As expected the Au(111) samples covered with the octanethiol SAM (Octa/SAM) and dodecanethiol SAM (Dode/SAM) augmented the water contact angle of the underlying Au(111) from 79° to 95° and 87° respectively (reference to Table 3.3). Measured Au(111) contact angle is comparable with the value of 71° reported for ultra-smooth gold surface⁶⁹. By growing a SAM on the Au(111) the hydrophobic exposed tails of the monolayers lowered the Au(111) surface energy from 34 mJ/m^2 to 21 mJ/m^2 and 19 mJ/m^2 for the Octa/SAM and Dode/SAM respectively by producing a sessile drop with higher surface tension. In contrast, the hydrophilic Au(111) substrate showed lower contact angle because the surface energy is greater. The SAMs water contact angle results are somehow different from Lages et al.⁷⁰ values of 105° for dodecanethiol and 86° for pentanethiol, a five carbons SAM, probably due to contamination.

It is important to understand that there is no absolute experimental solution for the surface free energy of solids. The results obtained from contact angle experiments are related to the purity of the test liquids and the cleanness of the solid surface under test. Contact angle experiments were performed after nanoindentation and AFM were performed on the samples. Additionally, for the drop analysis, an assumption that the drop is symmetric is considered. Finally, to obtain stable and valid contact angle data is needed precise control of the ambient humidity. In summary although contact angle measurements are relatively simple to perform, the interpretation in relationship to the surface energy is not simple.

4 NANOMECHANICS OF ALKANETHIOL SELF-ASSEMBLED MONOLAYERS

4.1 Introduction

It is very important for scientist and engineers to be able to measure and understand the mechanical properties of materials. These properties have been always a major consideration in the design of structures and materials in our society. In general, mechanical properties are not purely fundamental, in that the values attributed to them are usually dependent on the testing conditions in addition to the conditions of the material itself. In this regard, it is essentially to note that the values for mechanical properties discussed in this chapter were obtained using nanoindentation experiments. The technique was selected among others because by using nanoindentation it is possible to monitor, study, and measure the mechanical properties of small scale materials.

This chapter reports nanoindentation measurements of the mechanical properties of alkanethiol self-assembled monolayers on Au(111) substrates and compares how having a ~ 1 nm thick monolayer affects the mechanical properties of the underlying gold film. Very thin, organic surface layers play a vital role in many tribological processes, but how they modify the mechanical behavior of a surface is difficult to quantify. Using SAMs, which have a very uniform thickness and well defined structure, enables the role of a sub-nanometer thickness film to be investigated in a systematic manner.

4.2 Nanoindentation Experimental Methods

Nanoindentation experiments were performed using a TriboindenterTM (Hysitron, Minneapolis, MN) that uses an electrostatic transducer to apply loads. Fused silica was used to calibrate the indenter and identify the tip area function as discussed in Section 2.7.1. Air indent calibrations were performed before each experiment to automatically account for the position dependence of the electrostatic forces. The TriboindenterTM can be used in displacement or load control mode. In displacement control, the maximum depth and the speed in nm/s of the indent is set. In load control, the maximum load and the loading rate in $\mu\text{N/s}$ is set. Displacement control nanoindentation experiments were performed at room temperature with a Berkovich diamond indenter. Information and schematics of the Berkovich indenter geometry can be found in the Appendix A. During displacement controlled experiments the load is adjusted while keeping the loading/unloading displacements constant. The SAMs considered for this study were made from 1-octanethiol, 98.5% ($\text{CH}_3(\text{CH}_2)_7\text{-SH}$ on Au(111), 1-decanethiol, 96% ($\text{CH}_3(\text{CH}_2)_9\text{-SH}$) on Au(111), and 1-dodecanethiol, 98% $\text{CH}_3(\text{CH}_2)_{11}\text{-SH}$ on Au(111). All the samples were nanoindented in a dry state. The three type surfaces were tested: cleaned glass coverslip; Au(111) evaporated onto the glass; and the different SAMs grown on the respective gold substrates. Each sample was indented using maximum tip displacements of 40, 90, 140, and 190 nm. A trapezoid displacement function of 5 nm/sec loading and unloading with 5 seconds hold at peak load was used for all the measurements. An automated pattern (group of locations where indents are performed) consisting of a line of ten indents $8\mu\text{m}$ apart was created for each of the four maximum tip displacement. A total of forty indents were performed on each of the surfaces.

4.3 Oliver and Pharr Analysis

The reduced elastic modulus and hardness of the samples were evaluated from the load versus displacement curves using the previously discussed Oliver-Pharr^{31,71} method and the following equations.

$$H = \frac{P_{\max}}{A} \quad (4.1)$$

$$S = \frac{dP}{dh} = \frac{2}{\sqrt{\pi}} E_r \sqrt{A} \quad (4.2)$$

where A is the projected area for a Berkovich indenter (defined in Section 2.7.1), h_p is the plastic depth of penetration, H is the hardness, P_{\max} is the maximum applied load, and S is the contact stiffness during the initial unloading. The reduced elastic modulus accounts for the fact that elastic deformation occurs in both the indenter and the sample and it is related to the modulus of elasticity (E) through:

$$\frac{1}{E_r} = \left(\frac{1 - \nu^2}{E} \right)_{\text{sample}} + \left(\frac{1 - \nu^2}{E} \right)_{\text{indenter}} \quad (4.3)$$

For a standard diamond indenter tip E_{indenter} is 1140 GPa and ν_{indenter} is 0.07.

4.4 Results and Conclusions

Figure 4.1, Figure 4.2, and Figure 4.3 show representative load versus displacement curves for the different maximum tip displacements used for clean Au(111) and Au(111) surfaces modified with three different monolayers: octanethiol SAM (Octa/SAM); decanethiol SAM (Deca/SAM); and dodecanethiol SAM (Dode/SAM). It is very interesting that for the four different maximum tip displacements, SAM covered surfaces needed lower loads than for just the gold film to drive the indenter to the same displacement (except for Octa/SAM, 90 nm maximum displacement). The peak load for a given load also shows a dependence on SAM chain length with greater differences between the loads for plain Au(111) and the Dode/SAM than the differences for shorter chains. On average for the extreme case (Dode/SAM), maximum loads of 146 μN , 972 μN , 2324 μN , and 4248 μN were needed to displace the indent 40 nm, 90 nm, 140 nm and 190 nm, respectively, whereas for just the Au; 172 μN , 1048 μN , 2518 μN , and 4561 μN were needed for the same displacements. Table 4.1 reports the difference in the average maximum load needed to displace the indent 40 nm, 140 nm and 190 nm deep between Au(111) and the Au(111) modified with the three different chain length SAMs. The maximum applied load is dependent on the presence of the SAM and the differences are more pronounced for the longer chain length SAM and as the indents become deeper.

Representative load-displacement curves for indents performed on the glass substrate can be found in Appendix A

Table 4.1 Difference in the average maximum load needed for a given displacement between Au(111) and Au(111) + SAM. Load units in μN .

	40 nm	90 nm	140 nm	190 nm
Octa/SAM	171-168 =3 \pm 2	1027-1034 =-7 \pm 5	2502-2446 =56 \pm 16	4539-4397 =142 \pm 23
Deca/SAM	217-172 =45 \pm 10	1088-1054 =34 \pm 9	2585-2454 =131 \pm 15	4680-4414 =266 \pm 26
Dode/SAM	172-146 =26 \pm 4	1048-972 =76 \pm 7	2518-2325 =193 \pm 13	4561-4248 =313 \pm 14

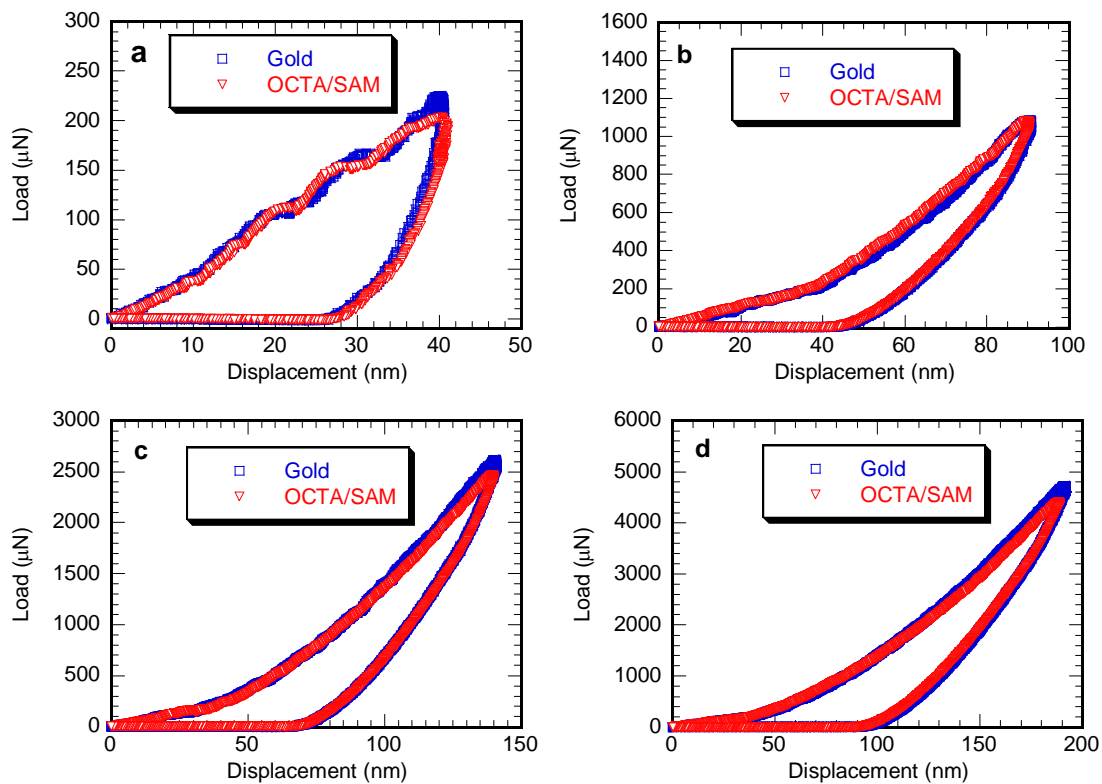


Figure 4.1 Characteristic load-displacement curves for ~20 nm Au(111) film on glass and octanethiol SAM on the same gold substrate. Nanoindentation experiments performed using displacement control mode with maximum displacements of (a) 40 nm, (b) 90 nm, (c) 140 nm, and (d) 190 nm.

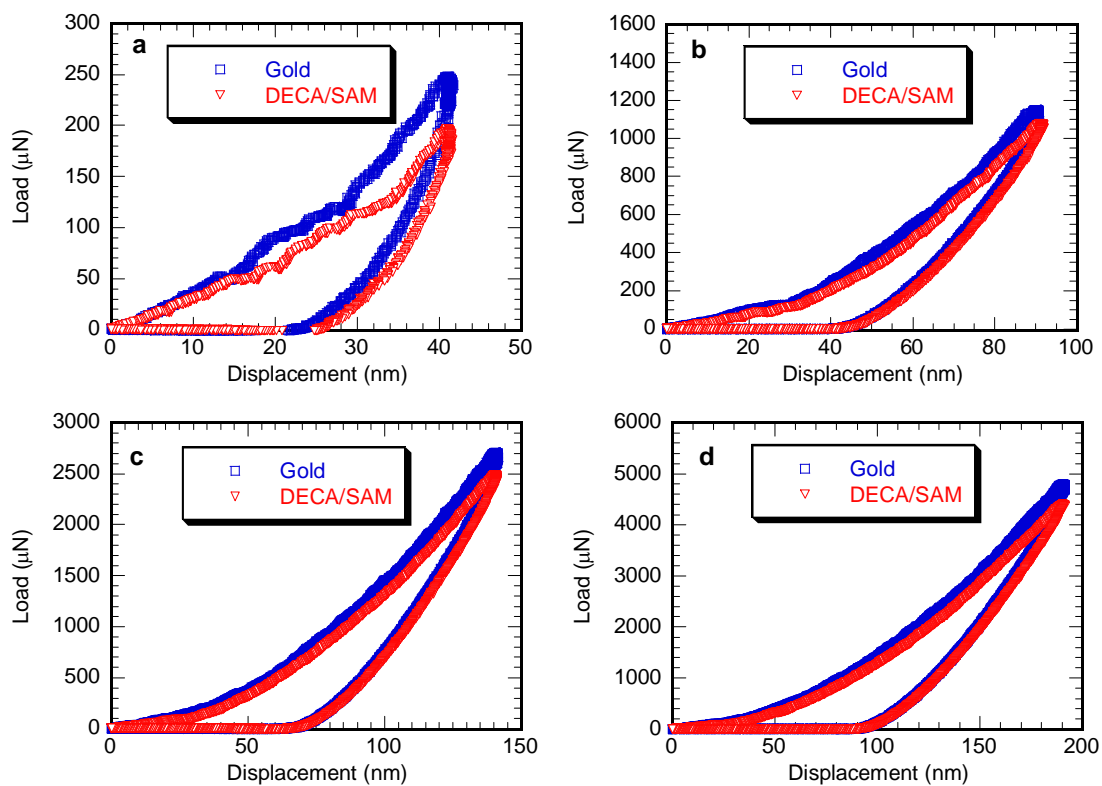


Figure 4.2 Characteristic load-displacement curves for ~20 nm Au(111) film on glass and decanethiol SAM on the same gold substrate. Nanoindentation experiments performed using displacement control mode with maximum displacements of (a) 40 nm, (b) 90 nm, (c) 140 nm, and (d) 190 nm.

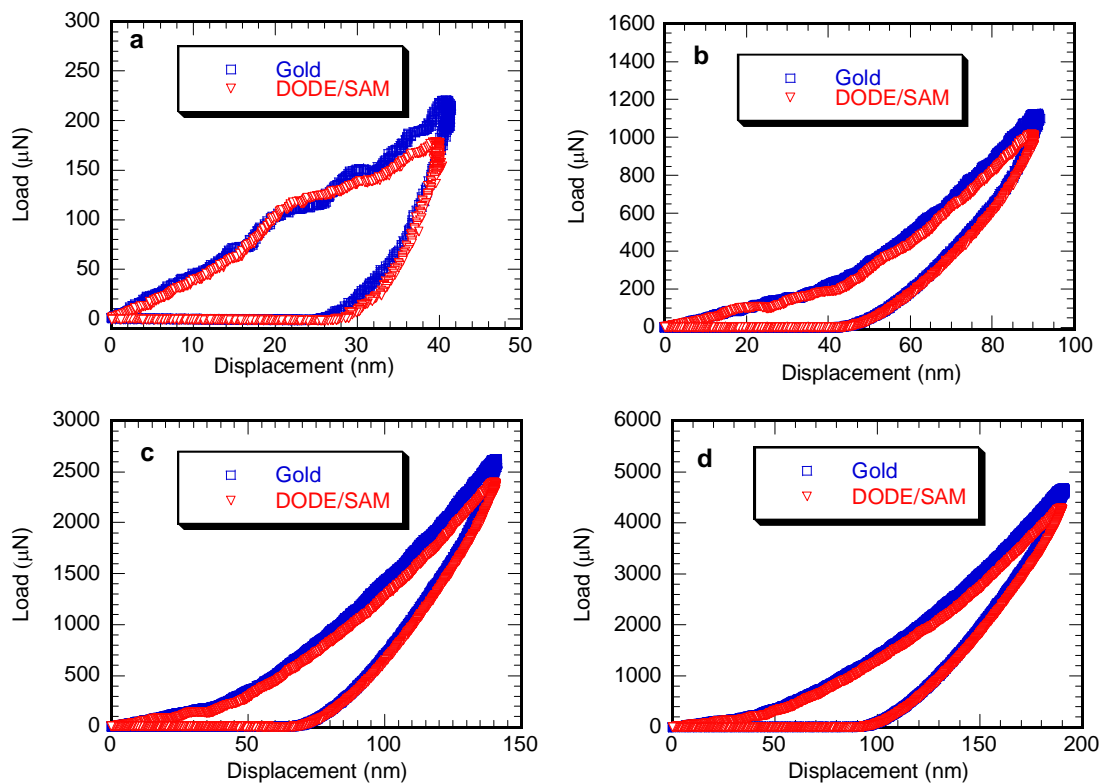


Figure 4.3 Characteristic load-displacement curves for ~20 nm Au(111) film on glass and dodecanethiol SAM on the same gold substrate. Nanoindentation experiments performed using displacement control mode with maximum displacements of (a) 40 nm, (b) 90 nm, (c) 140 nm, and (d) 190 nm.

4.4.1 Oliver and Pharr Hardness and Reduced Elastic Modulus

Figure 4.4 compares the Oliver and Pharr hardness (H_{OP}) for glass, Au film deposited onto the same glass, and Au modified with different SAMs (Figure 4.4a for Octa/SAM, Figure 4.4b for Deca/SAM and Figure 4.4c for Dode/SAM) as a function of maximum tip displacement. H_{OP} data shows an increase with indenter displacement converging on the substrate (glass) H_{OP} for both the Au and the SAM/Au films. No significant difference on the H_{OP} was seen between the Au and the Octa/SAM. The longer chain SAMs (Deca/SAM and Dode/SAM) both decreased the H_{OP} of their respective underlying gold films. The effect is more pronounced for the shallow indents (40 nm deep) where the H_{OP} of the Au was reduced by 23% by the Deca/SAM and 22% by the Dode/SAM. For the deeper indents, on average the Deca/SAM reduced the H_{OP} of the underlying Au film by 2%, when indenting 90 nm deep, and 4% for maximum displacements of 140 nm and 190 nm. In the case of the Dode/SAM the H_{OP} of the respective Au film was decreased by 7%, 6% and 4 % when indenting 90 nm, 140 nm and 190 nm deep. It should be noted that small variations in the gold film thickness affects the actual values for H_{OP} . This gives different values for the three gold films.

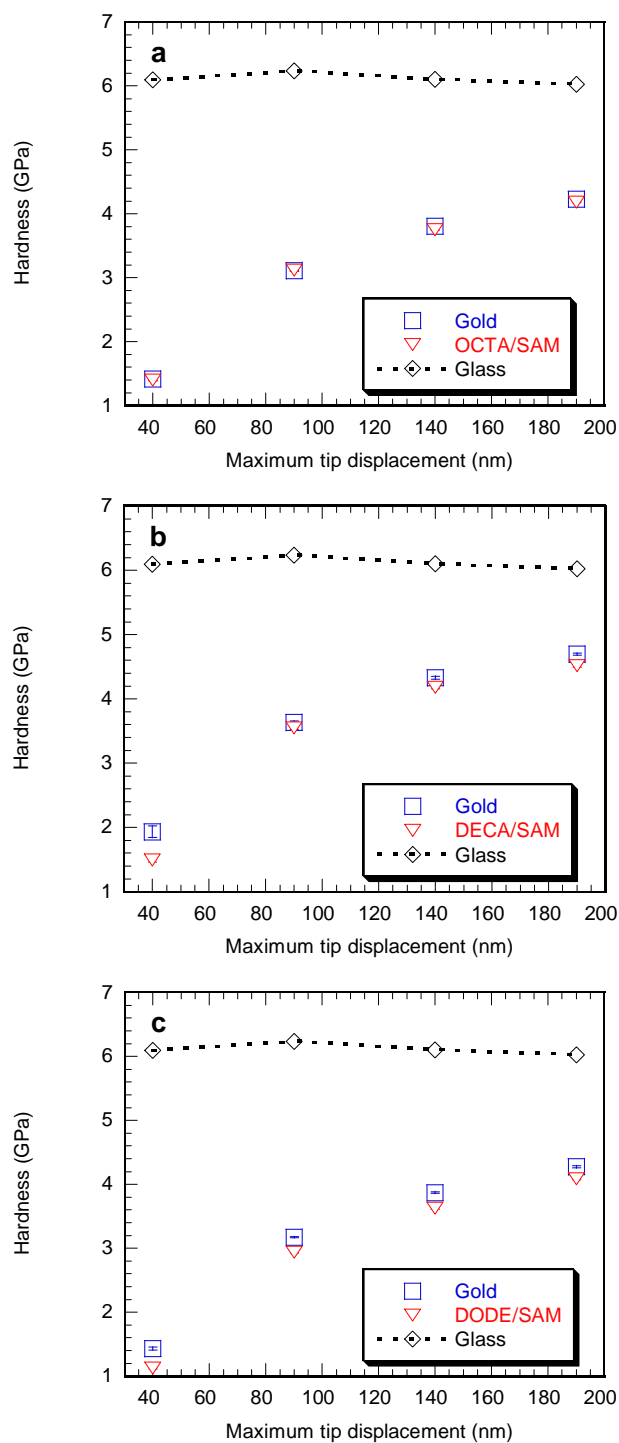


Figure 4.4 Oliver and Pharr's hardness for glass, evaporated gold on glass and (a) Octa/SAM, (b) Deca/SAM and (c) Dode/SAM as a function of maximum tip displacements. Error bars correspond to standard error.

Figure 4.5 shows the corresponding reduced elastic modulus based on the Oliver and Pharr analysis (E_{OP}) for glass, Au film deposited on the same glass, and Au modified with different SAMs (Figure 4.5a for Octa/SAM, Figure 4.5b for Deca/SAM and Figure 4.5c for Dode/SAM) as a function of nanoindentation maximum tip displacements. The E_{OP} data also shows some dependence on indenter displacement especially for the shallow indents. However, a different trend from H_{OP} on indent displacement is observed for the E_{OP} . For the shallow indents (40 nm deep) the E_{OP} of both the Au and SAMs/Au are similar to the values for glass. Conversely, for the following deeper indents (90nm), the E_{OP} of both the Au and SAMs/Au films decreased abruptly. When indenting at 140 nm and 190 nm, SAMs/Au films showed an increase in E_{OP} with indenter displacement which is not seen with just the Au (except for Deca/SAM).

No significant difference between the E_{OP} of the Octa/SAM and the Au is seen when indenting at 40 nm and 90 nm. For the deeper indents, 140 nm and 190 nm, the E_{OP} of the Au was decreased by the Octa/SAM by only 3% and 4%. On average, the Deca/SAM decreased the E_{OP} by 11% when indenting 40 nm deep and 7% when indenting at 90 nm, 140 nm and 190 nm deep. In the case of the Dode/SAM E_{OP} decreased by 8%, 6%, 8% and 9% when indenting at 40 nm, 90 nm, 140 nm, and 190 nm, respectively. Tabulated data containing the averaged H_{OP} and E_{OP} for both the Au films and modified Au with SAMs can be found in Appendix C.

The Oliver and Pharr analysis demonstrated that the even a ~ 1 nm thick organic film can affect the mechanical properties of an underling Au film. The results show a larger effect from the SAM on H_{OP} than E_{OP} and are more significant for the shallow indents than for the deeper. The variation of H_{OP} and E_{OP} with indentation displacement

is a very common effect for soft films on harder substrates. Some of the reported reasons in the literature are indeed a real reflection of the material. The striking thing in this case is that the SAM, a very thin organic film, gives substantially different mechanical properties from the underlying gold and bulk glass substrate. With respect to the shallow indents, it is difficult to quantify H_{OP} and E_{OP} for very small values of indentation displacement. The most commonly observed indentation size effect is the error associated with the area function of the indenter which is hard to determine accurately at small values of penetration depth.

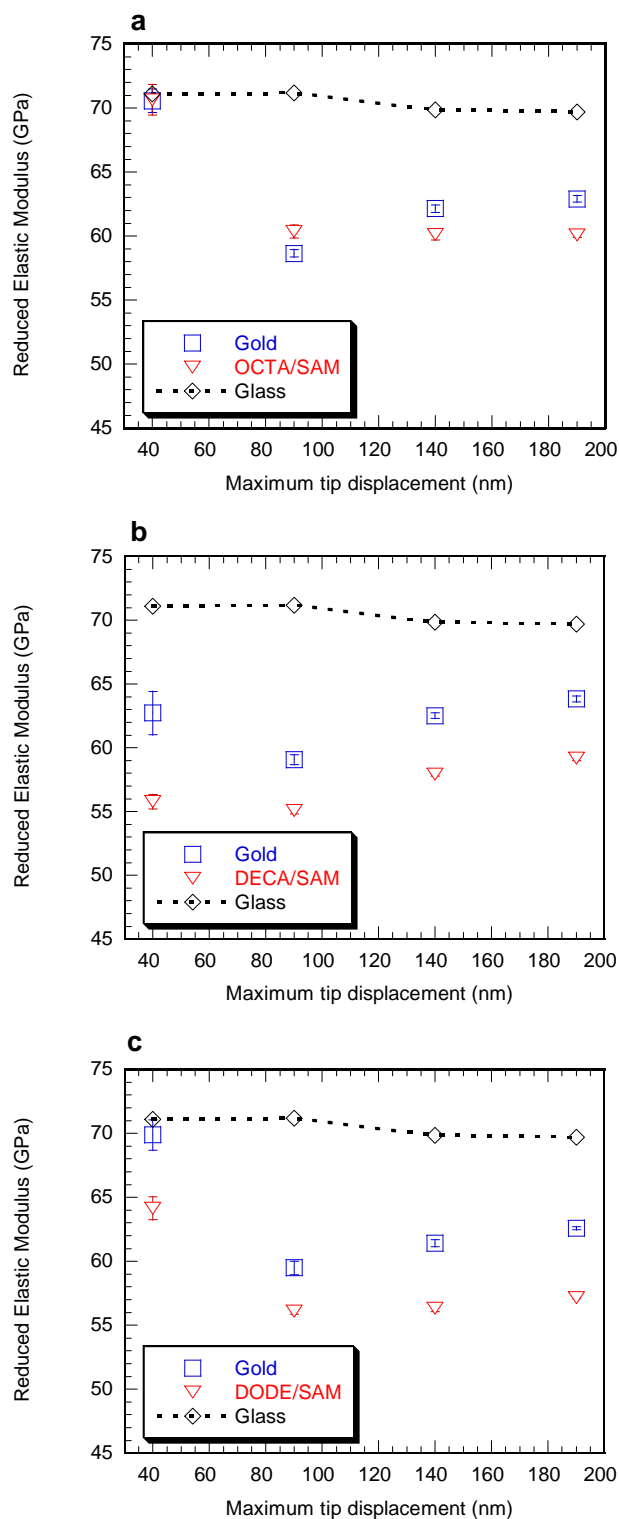


Figure 4.5. Oliver and Pharr's reduced elastic modulus for glass, evaporated gold on glass and (a) Octa/SAM, (b) Deca/SAM and (c) Dode/SAM grown on the corresponding gold surfaces as a function of maximum tip displacements. Error bars correspond to standard error.

4.4.2 Work of Indentation

During nanoindentation both the load and the displacement of the tip is monitored with high precision and accuracy^{72, 73}. In general, the response to the applied load is divided into an elastic-plastic loading followed by an elastic unloading. As shown in Figure 4.6 the net plastic area enclosed by the load-displacement curve represents the energy lost due to plastic deformation and stored elastic strain for residual stresses within the material. During unloading, work is then done by the system as the material elastically recovers.

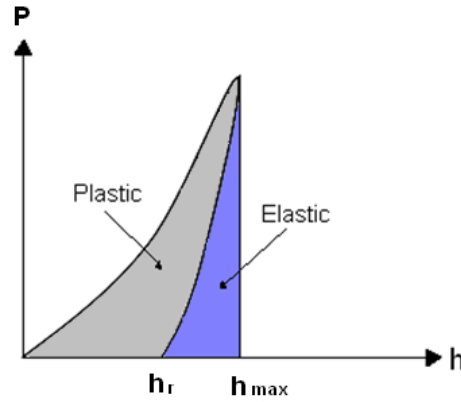


Figure 4.6 The plastic and elastic areas enclosed by the load-displacement curve.

The load-displacement curve obtained from nanoindentation can be considered equivalent to a force-distance curve and therefore by integration under the curve the work of indentation can be found. The total work done by the indenter, W_{tot} , to cause both elastic and plastic deformation when the indenter reaches maximum depth, h_{max} is given by:

$$W_{tot} = \int_0^{h_{max}} P dh \quad (4.4)$$

Integration under the load-displacement curves were numerically found using the trapezoid rule. Basically, the trapezoid rule works by approximating the area under the curve as the sum of very small trapezoids. The plastic (W_p), elastic (W_e) and total (W_{tot}) works of indentation were calculated from all the load-displacement nanoindentation curves. Integration under the loading curve gives W_{tot} , while integration under the unloading provides W_e . The difference between W_{tot} and W_e is the plastic work (W_p) of indentation.

Figure 4.7a, b and c compares the total works of indentation from the Octa/SAM, Deca/SAM and Dode/SAM with the work values for just the Au. The resulting W_{tot} are always less when indenting the SAMs compared to only the Au. As shown in Figure 4.8 the difference in the W_{tot} is larger for the shallow indents (40 nm deep) where the difference in W_{tot} is in average 8%, 20% and 15% for the Octa/SAM, Deca/SAM and Dode/SAM respectively.

The plastic work (W_p) was also evaluated and it was always less for the three different SAMs than for the Au at all four maximum displacements (Figure 4.7d, e, and f). As shown in Figure 4.9, the difference is more dramatic for the Deca/SAM and Dode/SAM where those decreased the W_p in some cases by 15% (e.g. Dode/SAM; 40 nm) and 20% (e.g. Deca/SAM; 40 nm, 190 nm). The plastic work (W_p) of indentation is physically related to the hardness⁷⁴ of an ideal plastic material, thus for a completely elastic contact the W_p is zero⁷⁵. In Section 4.4.1 the analysis of Oliver and Pharr gave H_{OP} values that showed the longer chain SAMs (Deca/SAM and Dode/SAM) both decreased the hardness of their respective underlying gold films and that the effect was more pronounced for the shallow indents (40 nm deep) where the hardness of the Au was

reduced by 23% by the Deca/SAM and 22% by the Dode/SAM. Thus, the work of indentation analysis and the Oliver and Pharr analysis show a similar effect with the SAM layer lowering hardness in both cases. It should also be noted that this effect is present at larger depth as well as shallow displacements (40 nm).

In the case of the W_e (Figure 4.7g, h, and i), the energy recovered elastically (W_e) is always less for the SAMs indented 40 nm deep. A percent of difference of 13%, 15% and 19% was found for the Octa/SAM, Deca/SAM and Dode/SAM. However, for the deeper indents (90, 140 and 190 nm) the difference in W_e is not as significant when standard error is considered.

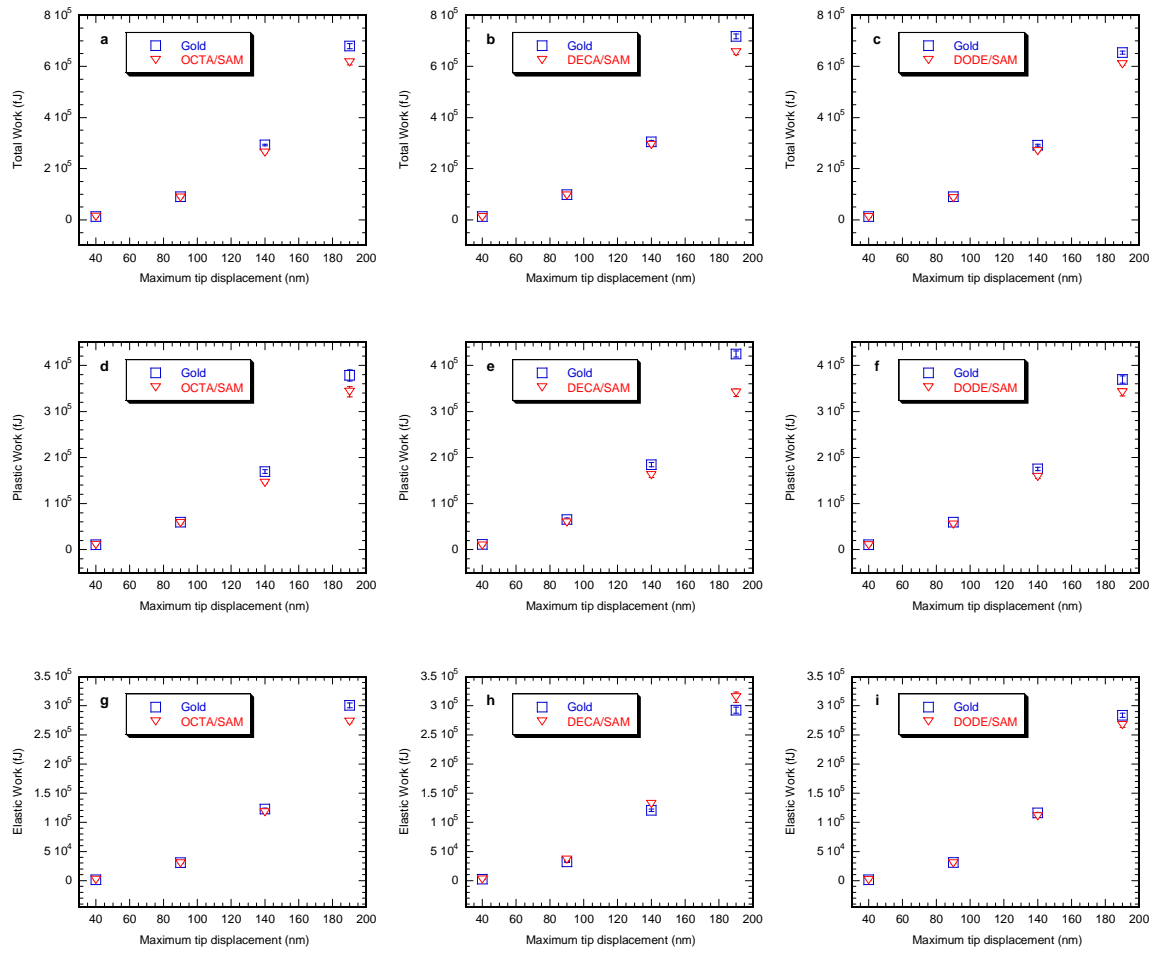


Figure 4.7 Values for works of indentation obtained by integration of the load-displacement curves by the trapezoid rule.

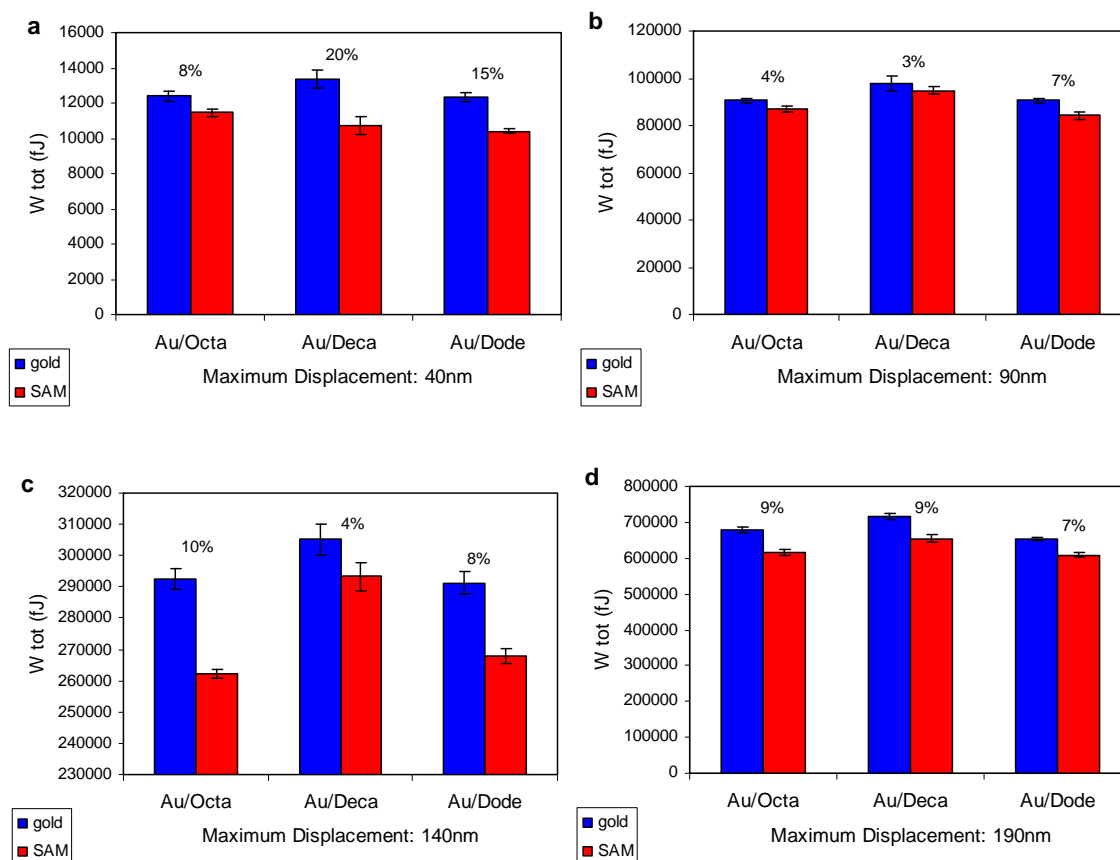


Figure 4.8 Comparison between the total work of indentation (W_{tot}) in femto Joules for Au(111) and Au(111) modified with different SAMs for maximum tip displacements of (a) 40 nm, (b) 90 nm, (c) 140 nm, and (d) 190 nm. Error bars correspond to standard error.

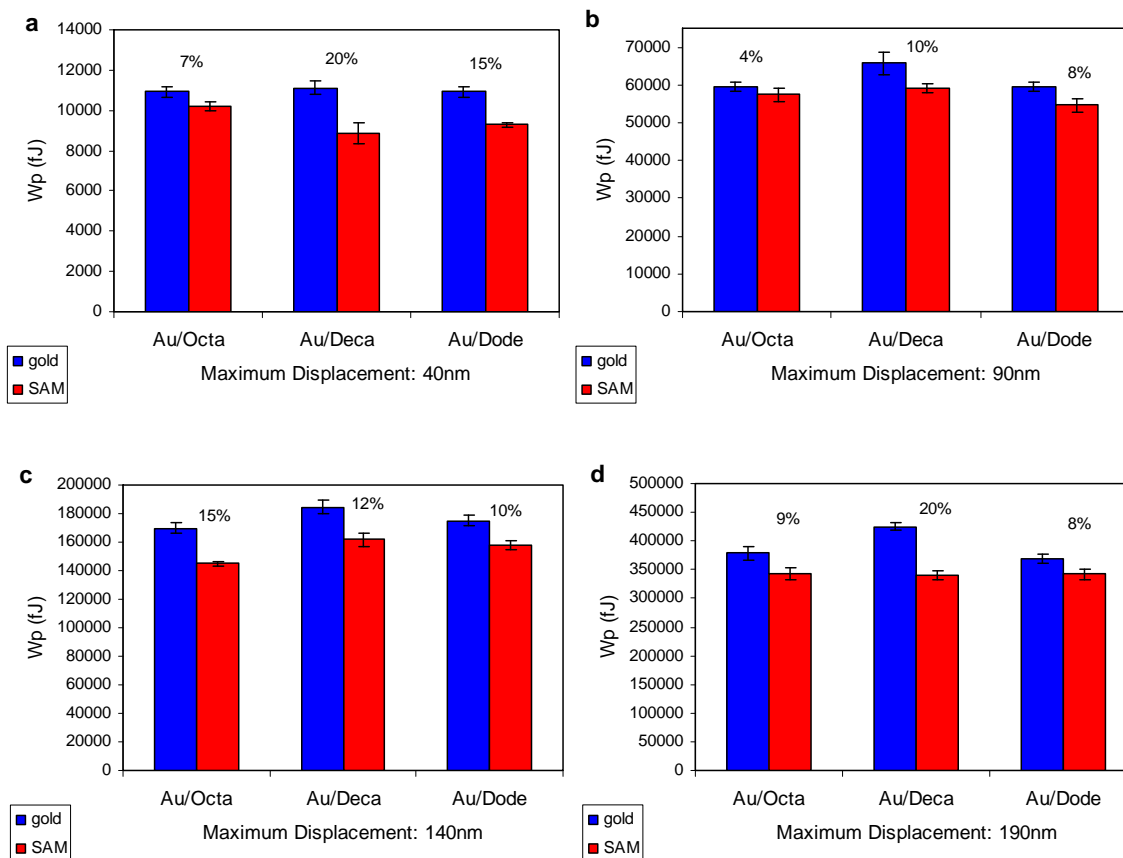


Figure 4.9 Comparison between the plastic work of indentation (W_p) in femto Joules for Au(111) and Au(111) modified with different SAMs for maximum tip displacements of (a) 40 nm, (b) 90 nm, (c) 140 nm, and (d) 190 nm. Error bars correspond to standard error.

From the load-displacement curves it is possible to calculate the total energy lost due to plastic deformation, but it is important to remember that in addition to plasticity heat is also dissipated in the process of indentation. The exact energy dissipated as heat is hard to approximate. The SAM layer may reduce the heat by lowering the top surface friction. This is likely to be negligible compared to the plasticity dependence. All the calculated work values can be found in Appendix D.

4.5 Effect of Chain Length on the Nanomechanics of Alkanethiol Self-Assembled Monolayers

The effect of a ~ 1 nm thick SAM on the mechanical behavior at depths up to 190 nm is surprising, but it should not be. It is known that SAMs can have a large impact on surface stress and this has been shown to impact elastic behavior in thin films. The present results suggest it may also affect plastic behavior.

The results discussed in the previous section showed that SAM chain length has an effect on the mechanical properties. In a recent study by Desikan et al.⁷⁶ the nanomechanical properties of alkanethiol SAMs were investigated using a bending microfabricated cantilever. The bending of a gold-coated cantilevers was monitored in situ during SAM formation. The difference in cantilevers surface stress was related to the alkanethiol adsorption coverage. Their results showed that adsorption of shorter chain alkanethiols on a gold coated cantilever resulted in larger surface stress values. In their paper it was concluded that shorter chain SAM increases the packing density by increasing the number of thiol-gold bonds. Conversely, a similar study by Berges et al.⁶ reported different results. In Berges paper the surface stress induced by the adsorption of alkanethiol SAM increased with increasing chain length. Godin et al.⁵ also studied the surface stress induced during the formation of SAM and concluded that the surface stress is not dependent on chain length. It is clear that the SAM formation kinetics and thermodynamics still are under debate. Many factors can influence the packing density of SAMs. Some of them are the concentration of the solution, purity of the SAM, and also the nature of the underlying gold.

We believe that longer alkane chains will produce denser packed SAMs. Van der Waals interactions between the hydrocarbon chains will help the monolayer to pack better and be more stable. Our hardness results show more SAM dependence for the twelve carbon SAM than the eight carbon SAMs which is consistent with dodecanethiol forming a better (denser) SAM. The effects of the SAM might be explained by changes in the contact geometry with longer chains better spreading the nanoindentation load and changing the contact area which results in a decrease in the hardness. Another, explanation could be related to how the SAM affects surface energy and surface stress. To distinguish between these further studies detailed in the following section, were undertaken.

5 RESIDUAL NANOINDENTATION IMPRESSION ANALYSIS BY ATOMIC FORCE MICROSCOPY

5.1 Influence of Pile-up on the Indentation Contact Area

In conventional indentation experiments, the area of contact is measured directly by imaging the residual impression in the sample upon removal of the load. One of the distinguishing attributes of nanoindentation is the ability to measure the mechanical properties from the load-displacement curve without direct measurement of the projected area of contact. However, when indenting elastic/plastic materials, the surface of the sample may either sink-in or pile-up around the indenter affecting the nanoindentation test data.

When indenting soft metals, such as gold, pile-up commonly occurs. Normally, standard nanoindentation hardness analysis procedures only take into account the contact area below the surface. The influence of pile-up on the measured hardness and elastic modulus by the standard analysis of the load-displacement curves was investigated by Bolshakov and Pharr using finite element simulations⁷⁷. Their results showed that depending on the extent of the pile-up the mechanical properties can be dramatically miscalculated. For instance, when pile-up is large, the projected contact area is underestimated by much as 60%, leading to an overestimation of the hardness and reduced elastic modulus. Pharr et al. have also shown that the extent of the pile-up depends on the strain hardening of the material. The accuracy of the hardness and elastic modulus depends on how well the equations used for H and E_r describe the indentation

deformation behavior. However, equations 4.1 and 4.2, both introduced in Section 4.3, were originally derived from a purely elastic solution to the indentation of an elastic half-space obtained by Sneddon²⁶ in 1965.

$$H = \frac{P_{\max}}{A} \quad (4.1)$$

$$S = \frac{dP}{dh} = \frac{2}{\sqrt{\pi}} E_r \sqrt{A} \quad (4.2)$$

If the material is analyzed as having a purely elastic contact it is considered that the material around the indenter does not show pile-up. For elastic/plastic contacts material around the indenter may either sink-in or pile-up. For some glasses and hard ceramics the plastic zone is typically contained within the boundaries of the contact and sink-in predominates. In contrast, when indenting soft metals, such as gold, piling up is expected. The effect of piling-up and sinking-in on the area of contact is shown in Figure 5.1. For the same maximum tip displacement, h_{\max} , the actual area of contact can be significantly greater for pile-up than the one calculated using the Oliver and Pharr analysis discussed in Section 2.7.1. Conversely, the contact area can be less than calculated if there is sink-in.

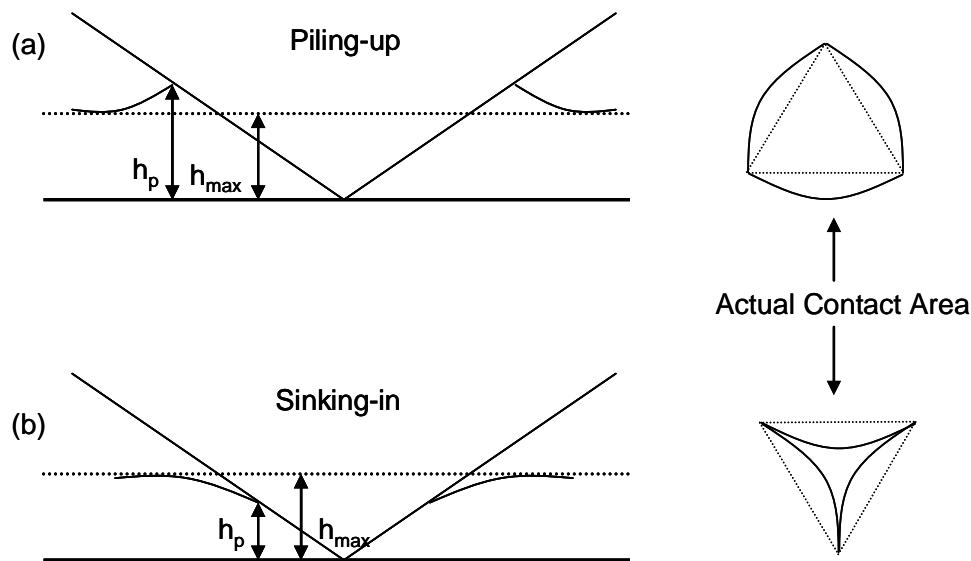


Figure 5.1 Effect of piling-up (a) and sinking-in (b) on the area of contact, h_p for the same maximum depth h_{max} . Adapted from Fischer-Cripps Nanoindentation, 2004²⁸.

It is generally accepted that when indenting soft, fcc metals like gold the material favors the plastic flow on the surface around the indent, leading to pile-up. For that reason, pile-up must be considered when studying the effect of a SAM layer on the mechanical properties of an underlying gold film. Atomic force microscopy was used to measure and compare the extent of the pile-up around indents on evaporated gold films (~20 nm) and the same gold surfaces modified with alkanethiol SAMs of different chain lengths. In section 5.7.1, it will be described how AFM images were analyzed using the Section analysis in the NanoScopeTM software to calculate the real nanoindentation contact areas. This gives more accurate hardnesses and elastic moduli values than those obtained in Section 4.4.1 using the Oliver and Pharr method.

5.2 Atomic Force Microscopy

Scanning Probe Microscopy (SPM) consists of a family of microscopes where a sharp probe is scanned across a surface while surface/sample interactions are monitored. The two primary forms of SPM are the Scanning Tunneling Microscope (STM) and Atomic Force Microscope (AFM). The first SPM developed was a Scanning Tunneling Microscope in 1982 by Binnig, Rohrer, Gerber and Weibel at IBM in Zurich, Switzerland. In 1986 Binnig and Rohrer won the Nobel Prize in Physics for this invention. The first Atomic Force Microscope (AFM) was developed in 1986 by Binnig, Quate and Gerber by a collaboration between IBM and Stanford University⁷⁸. Currently, SPMs are widely used in a variety of different disciplines. Information such as three-dimensional morphology imaging, surface roughness, conductivity, friction, magnetic field, and the mechanical properties among others can be obtained.

The AFM got its name from the interaction between the sample and the probe on the atomic level. Basically, the AFM scans surfaces and creates three dimensional images of the tip interaction with the surface. There are two main AFM operation modes; contact and tapping (or intermittent contact) mode. All the experiments discussed in this thesis were performed using the contact mode of operation, for that reason only this particular technique will be discussed.

In contact mode the AFM operates by scanning a tip attached to the end of a cantilever across the surface while the change in the cantilever deflection is monitored by a reflected laser beam from a small mirror on the cantilever onto a set of photodiodes. While the tip moves across the sample the cantilever bends in accordance to sample's surface topography. A piezoelectric scanner under the sample moves it in x-y (and z).

Additionally, a feedback loop maintains a constant cantilever deflection by vertically (z direction) moving the scanner at each x-y data point. The distance the scanner moves vertically is stored by the computer to form the topographical image of the surface. In this mode the AFM is operating as a nanoscale profilometer. More details about the principles of AFM can be found in the literature⁷⁹.

One of the advantages of combining nanoindentation data and AFM is the capability of measuring the contact area that it is used in the basic models of contact and adhesion⁸⁰. Given that the residual indentation impression can be imaged with nanometer resolution, the effect of pile-up around contacts in the plastic region can be distinguished and quantitatively studied.

5.3 Experimental Methods

AFM was used for imaging the nanoindentation residual impressions performed with the HysitronTM at 40 nm, 90 nm, 140 nm and 190 nm maximum tip displacements on Octa/SAM, Deca/SAM, Dode/SAM and their respective clean Au(111) substrates. All AFM experiments were performed using a Digital Instruments NanoScopeTM IV Scanning Probe Microscope. Operation took place in ambient environment.

Contact mode AFM was used because it has a range of advantages for gold compared to tapping mode. In practice, samples with extreme changes in vertical topography, such as indentation pile-up, can be scanned more easily in contact mode. Also, contact AFM provides images with better resolution.

For contact mode AFM it is necessary to use a cantilever which is soft enough to be deflected by very small forces and has a high enough resonant frequency that it is not susceptible to room vibrations. To accomplish these requirements, cantilevers for contact mode are short and thin, to provide high resonant frequency and a small force constant. All images were collected using non-conductive Si₃N₄ Veeco NanoProbe tips, model #NP-S20 with a spring constant of 0.06 N/m.

For all the experiments the feedback laser was aligned, the photodetectors adjusted to center the laser deflection, the tip was located under the microscope and the sample surface was focused. The following scan parameters were used for all images: scan rate was set to 0.3 Hz; tip velocity 1.80 $\mu\text{m/s}$; integral gain 0.1; proportional gain 0.2; and scan size to 3 μm x 3 μm . After approaching the sample, the cantilever force was calibrated and reduced to avoid scratching the surface with the tip and to maintain a constant imaging force between the different samples.

After imaging, the AFM tip was used as an ultra-low nanoindentation device to obtain force-displacement curves on the pile-up regions. This was performed to determine if delamination of the gold from the glass occurred during SAM formation. Delamination would give a highly compliant pile-up, whereas a solid pile-up due to plastic deformation will be very low compliance relative to the AFM cantilever (stiffness: 0.06 N/m). Note that stiffness is proportional to $1/\text{compliance}$.

5.4 Results and Discussions

5.4.1 Nanoindentation AFM Impression Images

The atomic force microscope was used to image the Berkovich indenter impressions. Figure 5.2 gives you an idea about how the indents from the different maximum displacements look on the gold surface. To assist in finding the nanoindents they were performed at a location identified by an arrow of indents. Four indents from each maximum displacement were centered with the AFM scanner and imaged using a $3\ \mu\text{m} \times 3\ \mu\text{m}$ image size. A total of 16 indents were imaged from each sample (three different SAMs and their three respective Au substrates).

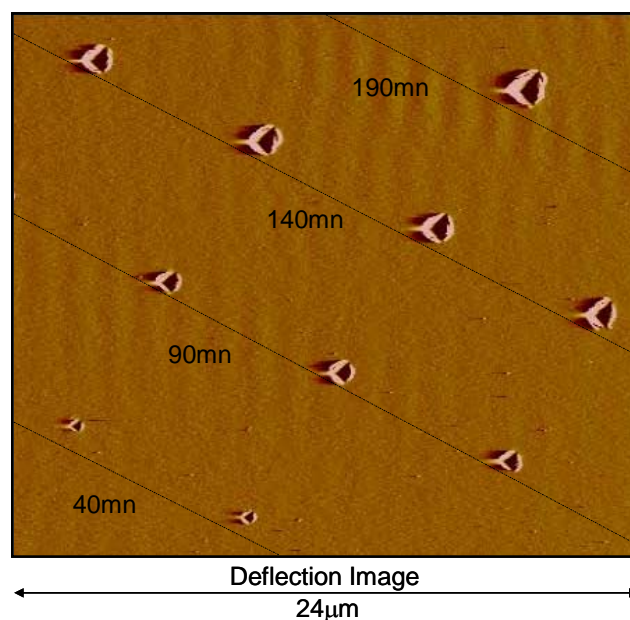


Figure 5.2 AFM deflection image of indents from the four different maximum tip displacements; 40 nm, 90 nm, 140 nm and 190 nm on the Au substrate (sample L4).

AFM characterization of the residual nanoindentation impressions showed substantial differences between the Au with SAM and Au alone. The most striking difference is the surface of the pile-up around the indenter is much greater when the SAM is present especially for the 10 and 12 carbon SAMs (decanethiol and dodecanethiol). The volume of the pile-up also is visibly much greater when indenting the SAM compared to just the Au. The dependence of the pile-up on the SAM becomes more pronounced as the indents become deeper. This is a very surprising result since surface effects, for instance due to a SAM ~ 1 nm thick, typically diminish with increasing indent depth. AFM deflection images for the indents performed on the Octa/SAM (Figure 5.3), Deca/SAM (Figure 5.4), Dode/SAM (Figure 5.5) and their respective gold substrates are shown below. The respective AFM height images can be found in Appendix E.

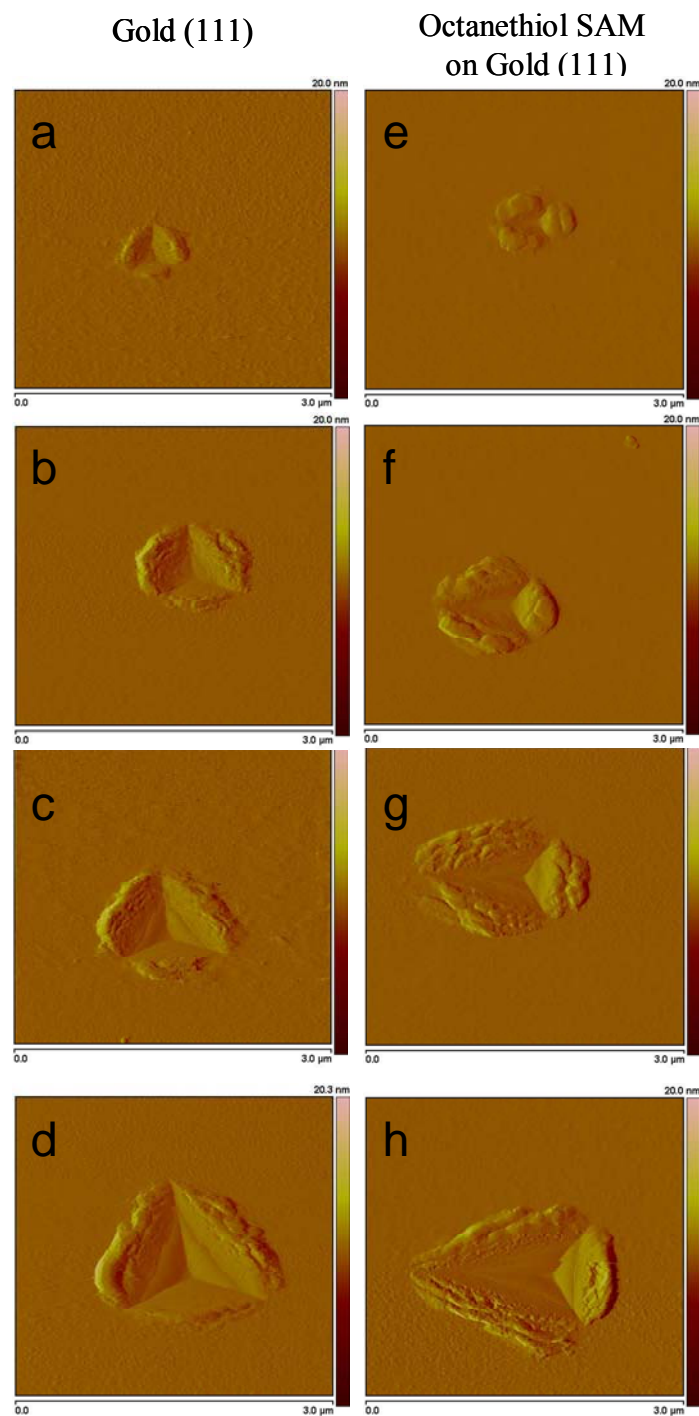


Figure 5.3 Representative AFM deflection images of residual nanoindentation impressions on Au (a, b, c, & d) and octanethiol SAM grown on the same Au (e, f, g & h). The maximum indenter displacements are respectively, 40 nm (a & e), 90 nm (b & f), 140 nm (c & g) and 190 nm (d & h).

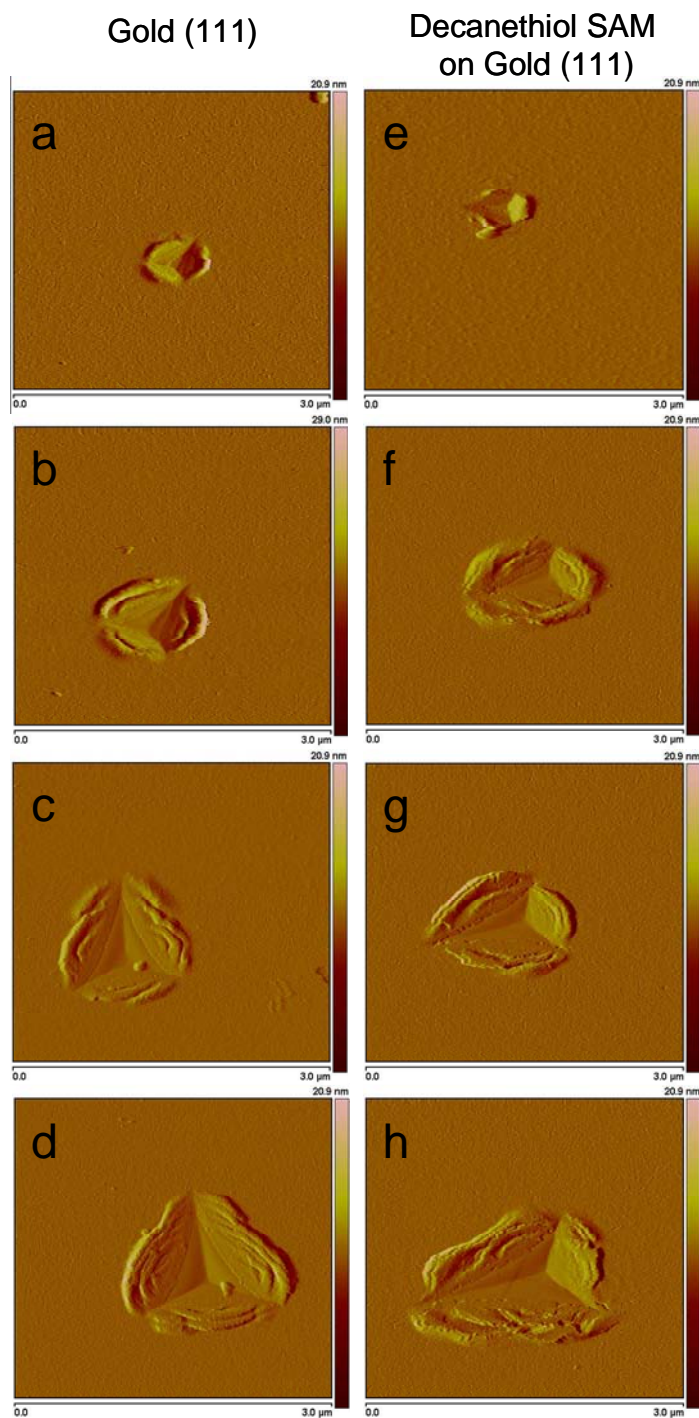


Figure 5.4 Representative AFM deflection images of residual nanoindentation impressions on Au (a, b, c, & d) and decanethiol SAM grown on the same Au (e, f, g & h). The maximum indenter displacements are respectively, 40 nm (a & e), 90 nm (b & f), 140 nm (c & g) and 190 nm (d & h).

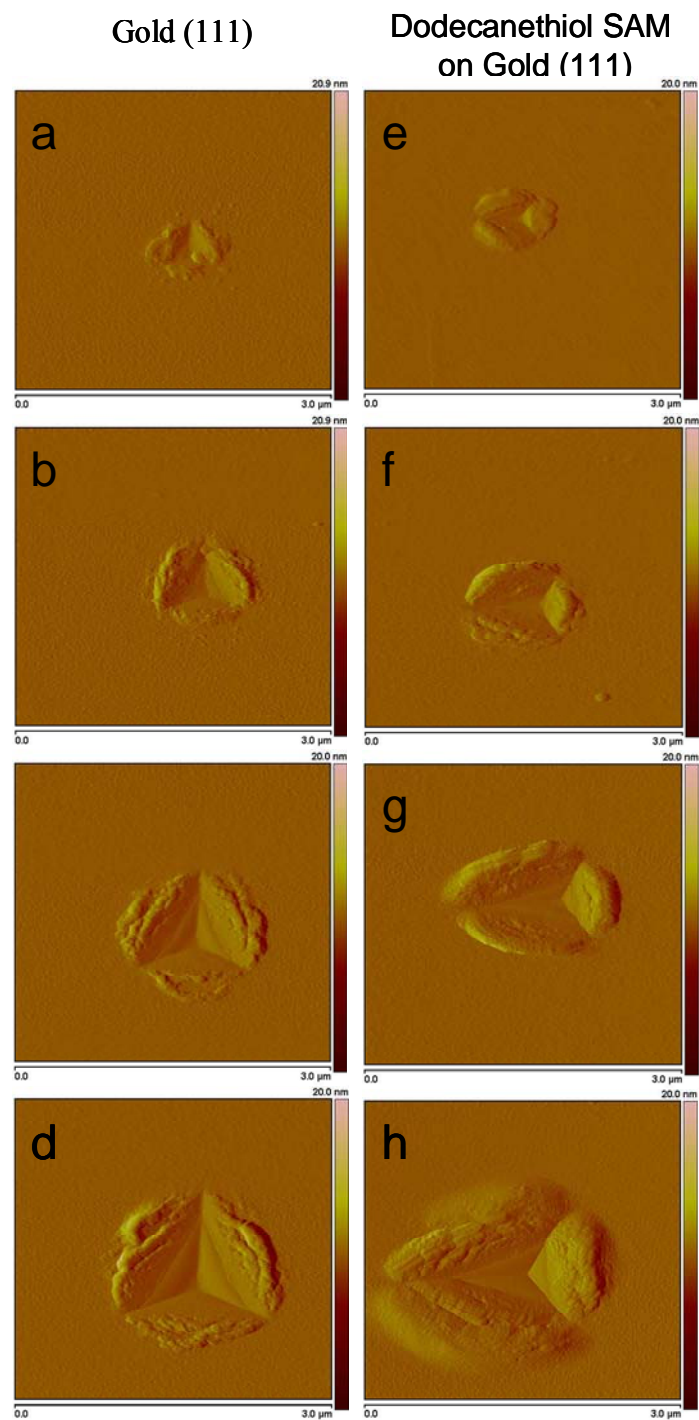


Figure 5.5 Representative AFM deflection images of residual nanoindentation impressions on Au (a, b, c, & d) and dodecanethiol SAM grown on the same Au (e, f, g & h). The maximum indenter displacements are respectively, 40 nm (a & e), 90 nm (b & f), 140 nm (c & g) and 190 nm (d & h).

Differences in the plastic deformation when indenting the Au(111) surface and the modified Au with the SAMs suggest an effect from strain hardening. It was noted by Tabor⁸¹ that strain hardening reduces pile-up, and that materials that cannot strain harden (fully strain hardened prior to indentation) tend to show large pile-ups. More recently the work of Pharr et al.⁷⁷ found a similar dependence of pile-up on strain hardening for nanoindentation. Loading and unloading creates an impression formed by plastic deformation. This introduces dislocations into the material causing a strain hardening effect and residual stress⁸². From nanoindentation load-displacement data it is very difficult to determine and quantify the effect of strain hardening in the residual impressions. AFM data shows that Au films covered with SAMs increase pile-up and hence reduce the strain hardening effect for the soft metal. Plain gold seems to compact due to introduction of dislocations more under the load of the indent, whereas gold with the SAM layers prefers to flow upwards showing higher and wider pile-ups. The differences in the pile-up for the indented Au and SAM/Au open a new window for the study in the field of chemomechanics where the effect of surface chemistry is related to dislocation mechanics.

The Figures below (Figure 5.6, Figure 5.7, Figure 5.8, Figure 5.9, Figure 5.10 and Figure 5.11) display comparative AFM 3-dimensional plot views between the indented gold substrate and the Deca/SAM and Dode/SAM. The selected images display color coded height information showing higher and wider pile-ups when the SAM is present on the gold substrate. A quantitative analysis of the pile-ups surface area will be discussed in Section 5.5.3.

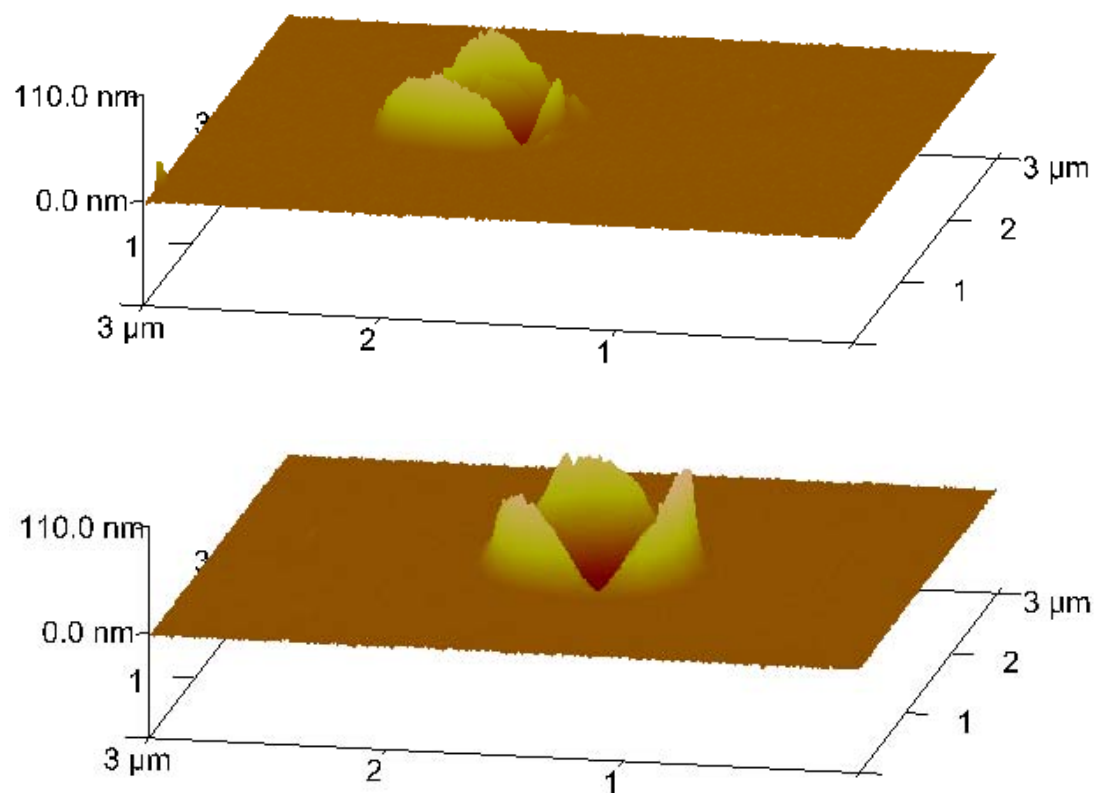


Figure 5.6 AFM 3-dimensional image of a 90 nm displacement controlled nanoindentation of Au (top) and Deca/SAM (bottom) grown of the same Au substrate.

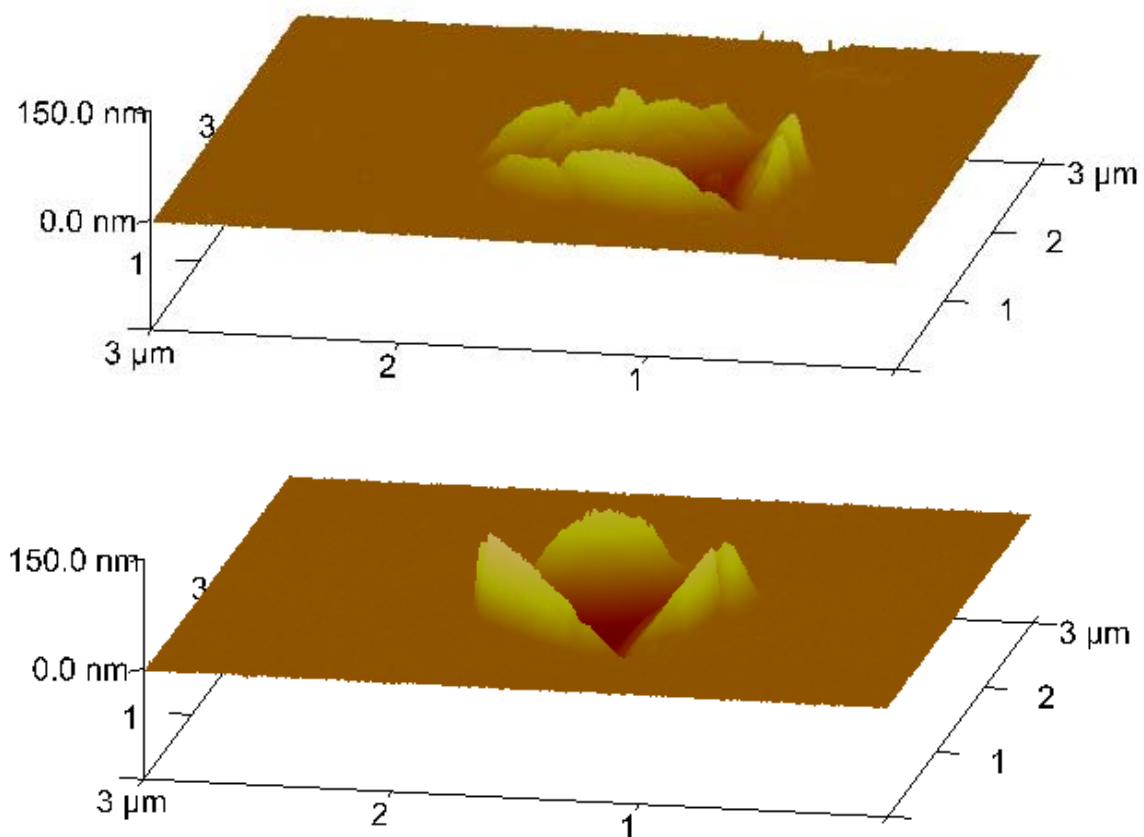


Figure 5.7 AFM 3-dimensional image of a 140 nm displacement controlled nanoindentation of Au (top) and Deca/SAM (bottom) grown of the same Au substrate.

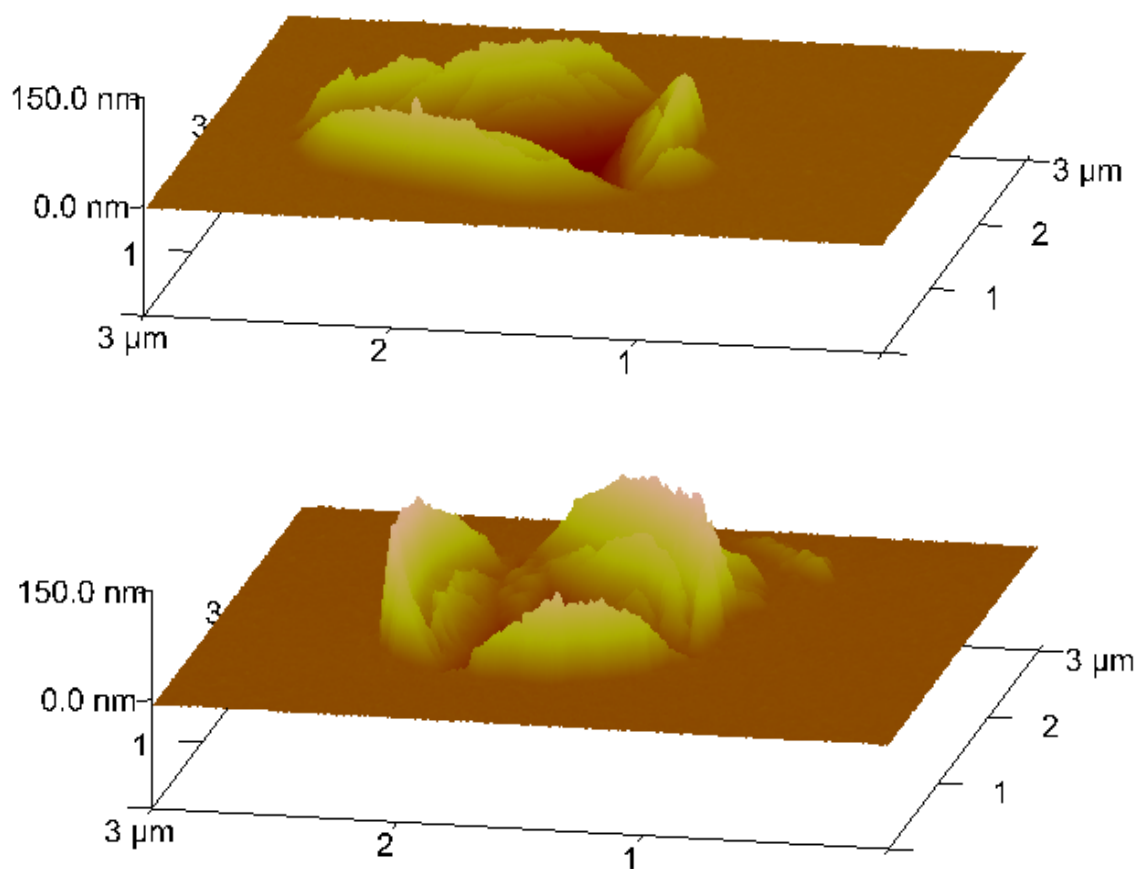


Figure 5.8 AFM 3-dimensional image of a 190 nm displacement controlled nanoindentation of Au (top) and Deca/SAM (bottom) grown of the same Au substrate.

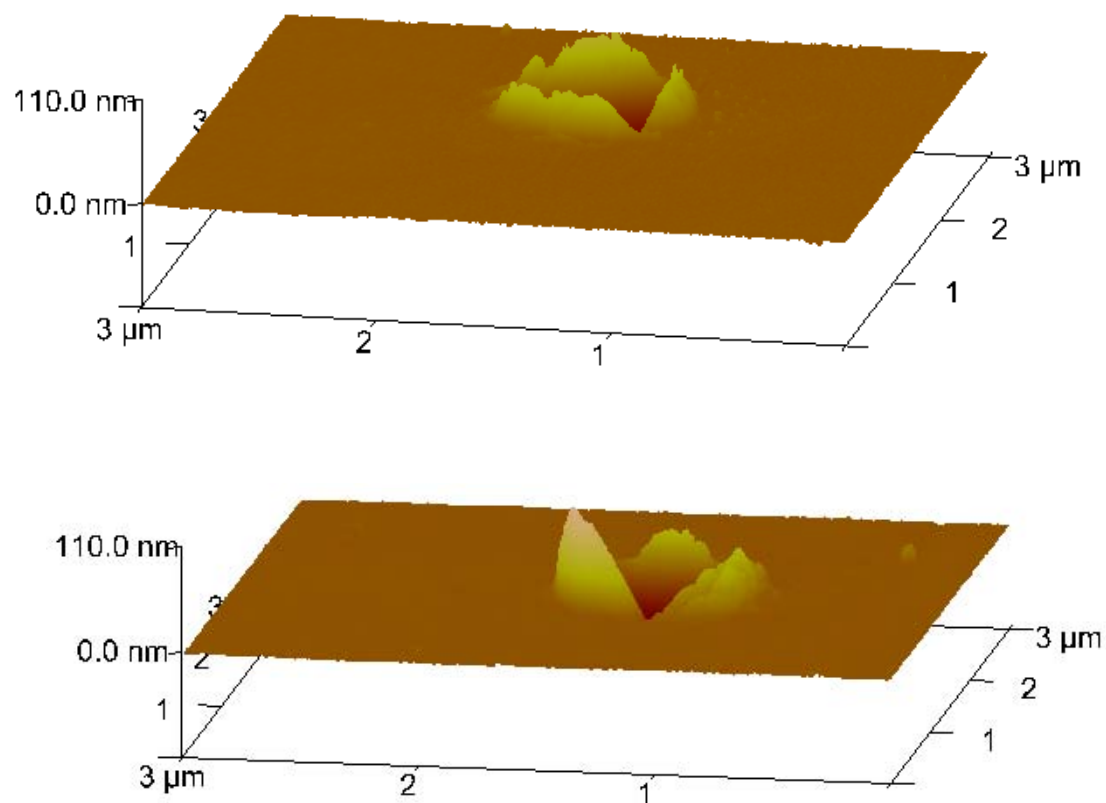


Figure 5.9 AFM 3-dimensional image of a 90 nm displacement controlled nanoindentation of Au (top) and Dode/SAM (bottom) grown of the same Au substrate.

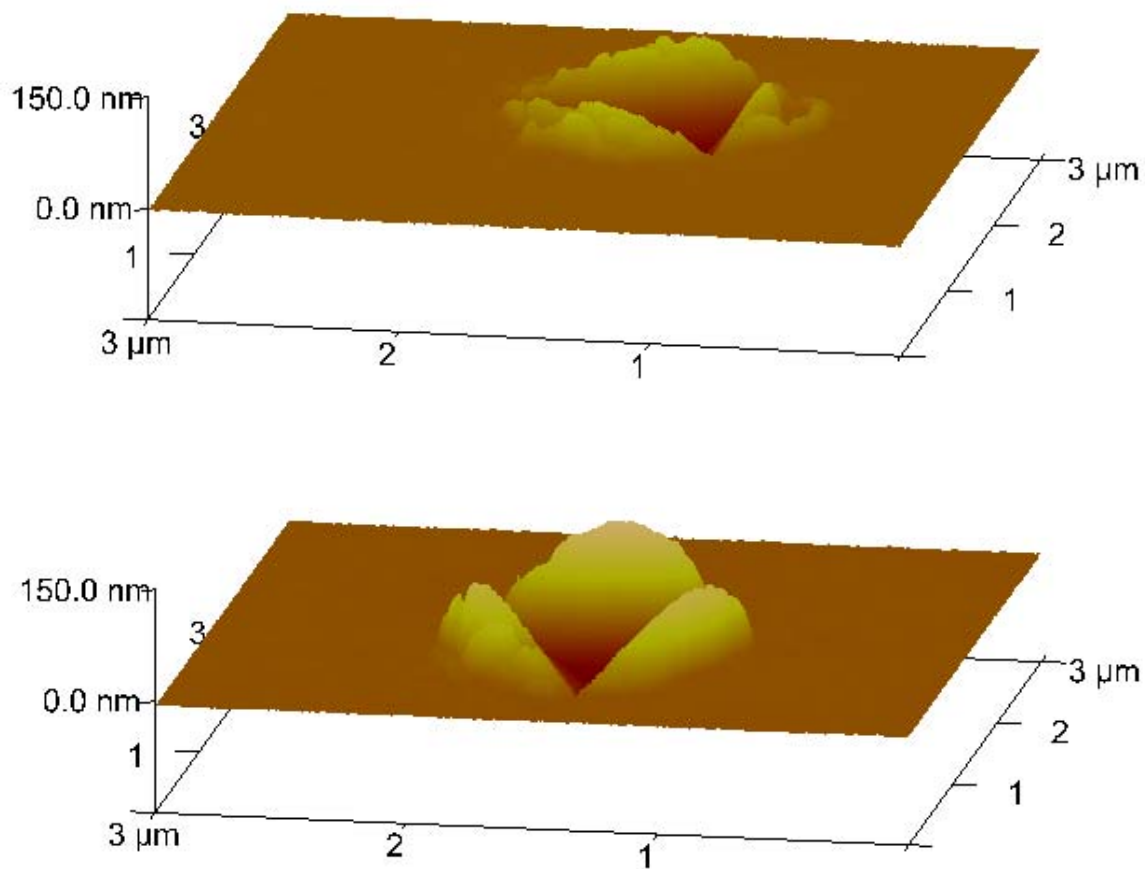


Figure 5.10 AFM 3-dimensional image of a 140 nm displacement controlled nanoindentation of Au (top) and Dode/SAM (bottom) grown of the same Au substrate.

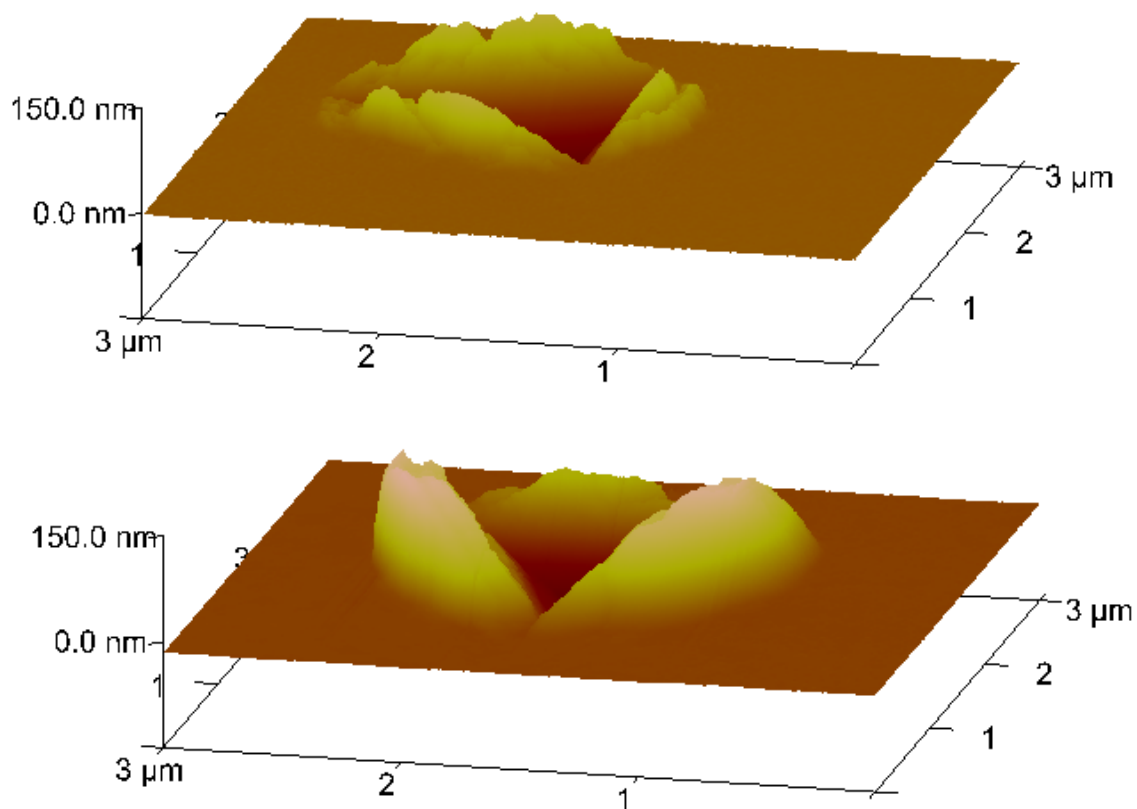


Figure 5.11 AFM 3-dimensional image of a 190 nm displacement controlled nanoindentation of Au (top) and Dode/SAM (bottom) grown of the same Au substrate.

5.4.2 Force Measurements

Force measurements were performed using the tip of the AFM while holding the x-y scanner position on top of the pile-ups. Figure 5.12 shows a representative AFM force curve performed on a 190 nm maximum tip displacement impression. The force curve is composed by the cantilever deflections, in nanometers, as a function of the scanner's vertical position (Z), in nanometers as well.

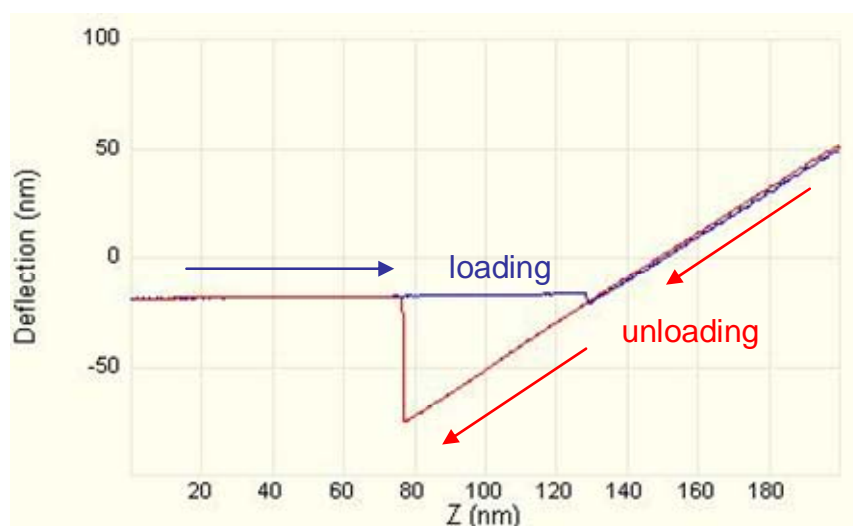


Figure 5.12 AFM cantilever deflection as a function of scanner displacement both in nanometers. The blue curve corresponds to the loading of the tip and the red curve to the unloading.

When the curve in Figure 5.12 suddenly rises it means the tip is in contact with the surface. As the scanner is moved vertically in a way such that it is in contact and later pushing the surface, the cantilever is simultaneously deflected. A linear approximation was used to calculate the slope of the portion of the force curve where the tip is in contact with the sample. The slope of the curve is equals to 1.0 meaning that the displacement of the scanner, while in contact with the surface, is equals to the deflection of the cantilever.

That is, the AFM tip causes no deflection or deformation of the materials and, hence, the pile-up is very stiff in comparison to the cantilever (0.06 N/m). This suggests that delamination of the gold has not occurred since a delaminated layer would be very compliant. In the case of delamination, air pockets underneath the surface, would allow the tip to be displaced vertically more than it is deflected.

5.5 Effect on Surface Area

This section discusses the mathematical approach used to calculate total surface area and the maximum pile-up height created by the different nanoindentation experiments on evaporated gold and different length alkanethiol SAMs discussed in detail in Section 4.2. The following approach is based on the analysis and processing of the residual nanoindentation impressions by atomic force microscopy.

5.5.1 Numerical Definition of Surface Area

Double integrals can be applied to compute the surface area over a region of a differentiable function of two variables. To better understand this proposition assume that the function $z=f(x,y)$ has continuous partial derivatives f_x and f_y in a region R of the x - y plane. The region R can be partitioned by grids with lines parallel to the xy coordinate axes. Each rectangle is vertically projected in R . The area of the rectangles in R is $A=DyDx$ being Dx and Dy the length of the sides of the rectangles. However the area of the partitions in z is not $DyDx$ since they are not rectangles. The corresponding surface can rather be approximated as a parallelogram $ABCD$.

The two adjacent sides of the parallelogram in vector form are defined by:

$$AB = Dx \, i + f_x(x,y)Dx \, k \quad (5.1)$$

and

$$AC = f_y(x,y)Dy \, i + Dy \, k \quad (5.2)$$

The area of one parallelogram patch is defined by:

$$A_{parallelogram} = \|AB \times AC\| \quad (5.3)$$

To compute the area of the parallelogram we need to find the cross product

$$\|AB \times AC\| = \begin{vmatrix} i & j & k \\ Dx & 0 & f_x(x,y)Dx \\ 0 & Dy & f_y(x,y)Dy \end{vmatrix} \quad (5.4)$$

Then

$$\begin{aligned} A_{parallelogram} &= \|AB \times AC\| = \left\| - (f_y(x,y)DyDx)i - (f_x(x,y)DyDx)j + (DyDx)k \right\| \\ &= \sqrt{f_y(x,y)^2 (DyDx)^2 + f_x(x,y)^2 (DyDx)^2 + (DyDx)^2} \\ &= \sqrt{f_y(x,y)^2 + f_x(x,y)^2 + 1} \, Dx Dy \end{aligned} \quad (5.5)$$

To calculate the surface area over the entire z we need to sum all the parallelograms areas and take the limit as the rectangle size approaches zero. This results in a double Riemann sum (a double integral). Thus the definition of surface area assuming that $z=f(x,y)$ is a differentiable surface over a region R is defined by

$$A_{surface} = \iint_R \sqrt{f_x(x,y)^2 + f_y(x,y)^2 + 1} \, Dx Dy \quad (5.6)$$

Detailed information about double integrals and the numerical definition of surface area can be found elsewhere^{83, 84}.

5.5.2 Surface Area Calculations

One of the most important features of atomic force microscopy is its capability to measure quantitatively spatial dimensions. A Matlab code was created to analyze and measure the total surface area of the residual nanoindentation impressions based on the double integral method discussed in Section 5.5.1.

Image Preparation

In order to estimate surface area values from AFM images all the AFM images were flattened with the NanoScopeTM 6.13R1 software using a first order polynomial fit. The flatten command basically is a filter that modifies the data by removing tilt from the image and deleting low frequency noise. During flattening the software removes the Z offset between scan lines, and the tilt in each scan line, by calculating a first order, least-squares fit for the unmasked segment then subtracting it from the scan line.

In order to load the AFM images with Matlab all the AFM images after flattening were exported as an ASCII text file within the NanoScopeTM software. The Matlab code can be found in Appendix F.

5.5.3 Results and Conclusions

The change in surface area was calculated from the difference between the surface area of a $3\text{ }\mu\text{m} \times 3\text{ }\mu\text{m}$ flat surface and the same area indented. By doing that the change in the surface area corresponds to the new surface area created by nanoindentation (both the contribution from the pile-up and contact from the Berkovich indenter). The area of the plain surface is equals to $(5.86)^2 \times 512 \times 512$. The number 5.86 corresponds to the

actual length of each pixel in the 512 by 512 AFM image. The total surface area of all the AFM images of the residual impressions from the different SAMs and gold substrates were calculated using the Matlab code discussed above.

Figure 5.13 compares the change in surface area when indenting the Octa/SAM, Deca/SAM and Dode/SAM compared to the gold substrate alone as a function of maximum tip displacement. On average the new surface area created (Δ surface area) by indenting the Deca/SAM and Dode/SAM compared to just their gold substrates decreased by 21% and 14% respectively for the shallow indents (40 nm deep). This effect can be explained by the effect of attracting forces between the Au in the surface and the indenter at the nanocontact. As previously stated, SAMs can be used to reduce attractive forces during indentation tests. One possible explanation is that the SAM layer is reducing the attractive forces and hence, the load. Thus, decreasing the plastic deformation of the underlying gold when indented 40 nm deep. For the shallow indents on the Octa/SAM the behavior was different from the other SAMs. When indenting the Octa/SAM 40 nm deep more surface area was created compared to when indenting the gold alone. This effect can be attributed to the ordering of the SAM packing due to the small chain length of only eight carbons.

As shown in Table 5.1, in the case of maximum tip displacements of 90 nm deep, the three different SAMs; Octa/SAM, Deca/SAM and Dode/SAM, increased the Δ surface area by 24%, 17% and 32% compared to the Δ surface area of their plain gold surfaces. For maximum tip displacements of 140 nm deep, again the three different SAMs increased the Δ surface area by 22%, 26% and 54% and for 190 nm deep by 71%, 37% and 82%.

Table 5.1 Percentage increase in surface area for indents with SAM layer compared to indents on clean Au(111). A decrease in the surface area was observed for Deca/SAM and Dode/SAM when indented 40 nm deep.

	40 nm	90 nm	140 nm	190 nm
Octa/SAM	34%	24%	22%	71%
Deca/SAM	↓ 21%	17%	26%	37%
Dode/SAM	↓ 14%	32%	54%	82%

It is difficult to compare the effect of the SAM on the plastic deformation as a function of SAM chain length since the gold used to grow the Deca/SAM was prepared in a different evaporator machine. This may have given a slightly different gold thickness which can dramatically change strain-hardening. Additionally, the time elapsed between SAM formation and indentation was different for each of the samples. Lio et al.⁸⁵ studies with STM and He-diffraction have seen some effect on the ordering of the SAM as a function of time therefore it is something to consider. What can be concluded is that unquestionably the SAM is affecting the gold plastic flow when subjected to an external load and that the effect on the plastic deformation is dependent on nanoindentation displacement. At shallow depth, the effects of modified surface adhesion may reduce the force on the surface and hence, reduce the extent of plastic deformation. In contrast, for the deeper indents the increase in the plastic flow (pile-up) when the SAM is present can be due to a variety of different reasons. First the increase in the plastic deformation can be an effect of dislocation nucleation induced by the SAM as seen in dislocation piling-up on an oxide layer. In addition, the SAMs lower the surface energy of the gold (as discussed in 3.6.2) making it easier to create new surface

so less work of indentation is needed. The SAM layer is known to lower the friction between the indenter tip and the surface, and it is known that lowering this friction may increase pile-up in ductile materials, such as gold though Tabor noted that friction has only a minor effect on plasticity. Finally, the SAM layer changes surface stress which may affect the image forces on dislocations.

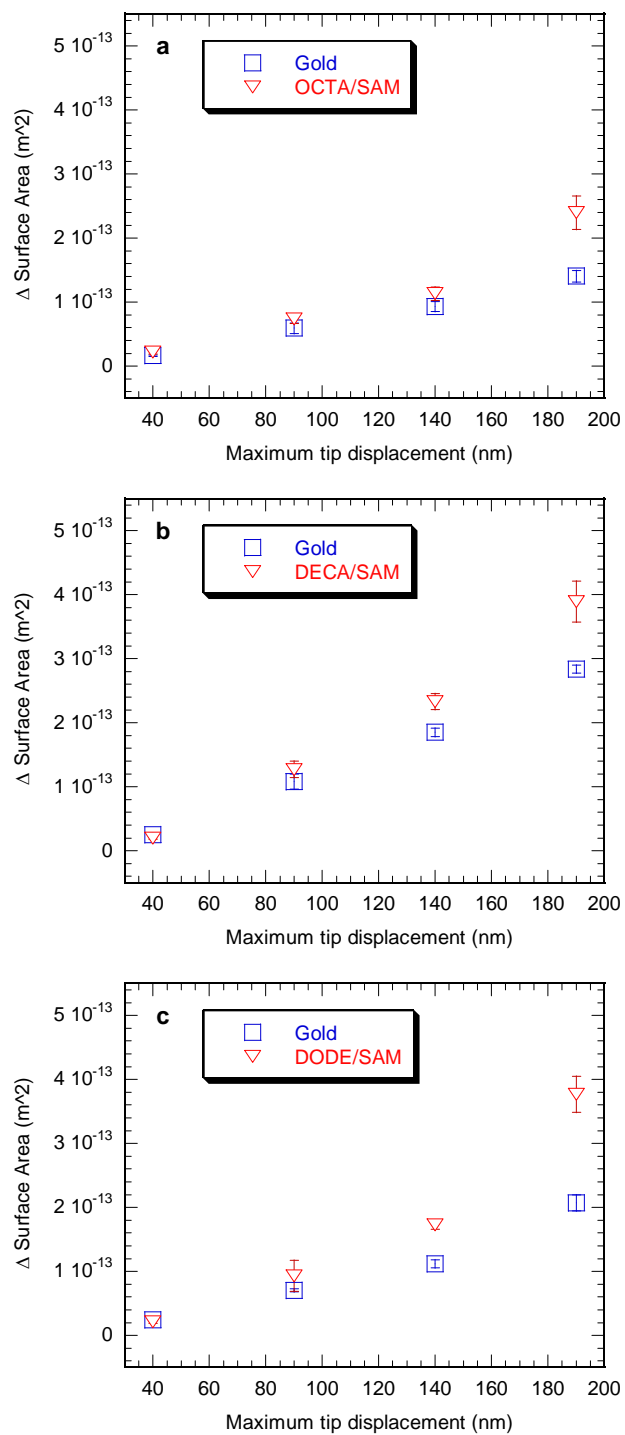


Figure 5.13 Comparison between new surface areas created during indentation of plain gold and modified gold with SAMs. Bars correspond to standard error.

The maximum pile-up heights were also measured from the AFM images with the Matlab code. The maximum nanoindentation pile-up heights of the Octa/SAM, Deca/SAM and Dode/SAM when indented 40 nm deep were in average 7%, 2% and 8% higher for the gold surfaces compared to when indenting the SAMs. These results were expected since the change in surface area (discussed previously) also showed that more new area was created when indenting the gold 40 nm deep compared to the surface modified with the SAM.

Table 5.2 Percentage increase in pile-up height for indents with a SAM layer compared to indents on clean Au(111).

	40 nm	90 nm	140 nm	190 nm
Octa/SAM	↓ 7%	↓ 23%	4%	13%
Deca/SAM	↓ 2%	18%	23%	23%
Dode/SAM	↓ 8%	10%	47%	20%

As shown in Table 5.2, for the deeper indents, as before, the trend is different. When displacing the tip 90 nm, 140 nm and 190 nm deep the material that plastically flowed and was deposited on the surface around the indentation site leading to pile-up, showed to be higher when the SAMs were present compared to the Au alone. For tip displacements of 90 nm the Deca/SAM and Dode/SAM showed in average pile-up heights 18% and 10% higher compared to the Au substrate. In the case of maximum displacements of 140 nm and 190 nm deep the Octa/SAM, Deca/SAM and Dode/SAM increased the pile-up heights by 4%, 23% and 47% and 13%, 23% and 30% respectively.

The effect of the SAM on the plastic flow increased in average with SAM chain length and indentation displacement. The maximum pile-up heights results for all the experiments are presented in Figure 5.14. The numerical values for all the experiments can be found in Appendix H.

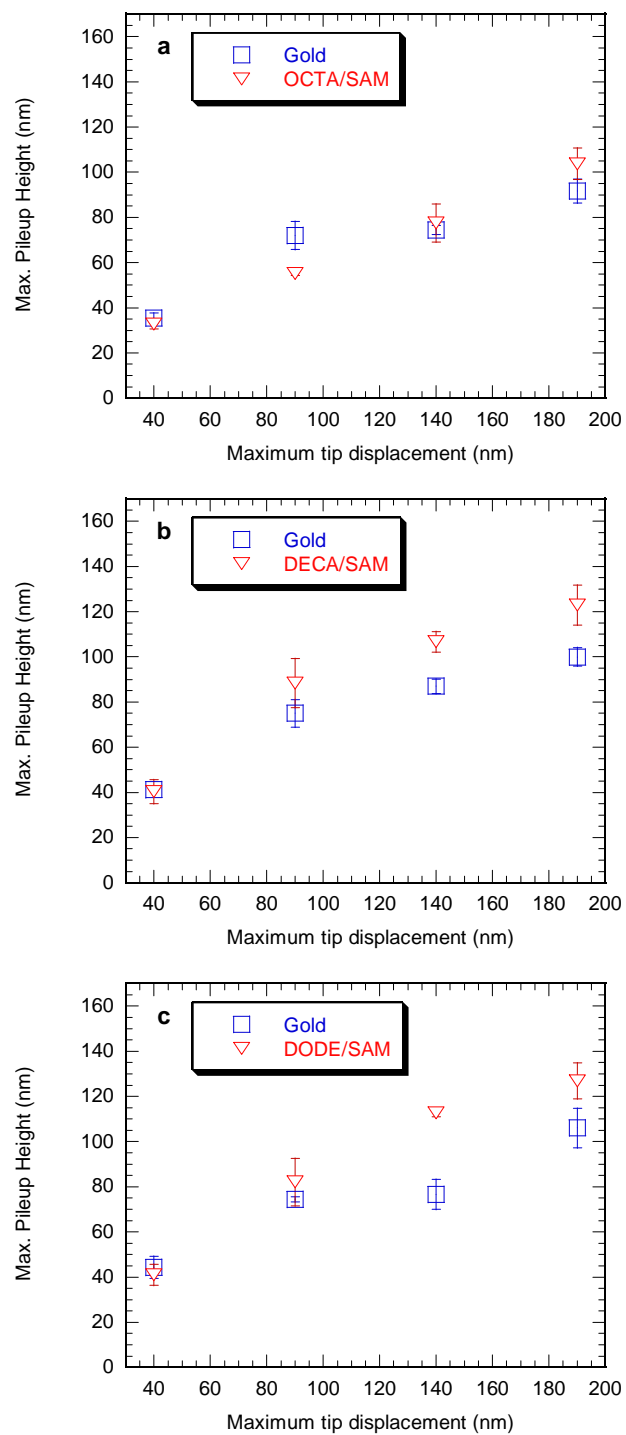


Figure 5.14 Comparison between maximum nanoindentation pile-up heights for (a) Octa/SAM, (b) Deca/SAM and (c) Dode/SAM compared to the pile-up height of their respective indented gold substrates. Bars correspond to standard error.

5.6 Projected Area of Contact

In nanoindentation the projected contact area is estimated from the plastic depth of penetration (h_p). However when pile-up is large, the area of the impression deduced from the Oliver and Pharr³¹ analysis can be underestimated leading to an overestimation of the hardness and elastic modulus. The main reason why H and E_r approximations from nanoindentation load-displacement curves fail to properly describe the plastic and elastic behavior is because of assumptions regarding contact geometry. Pile-up of the material around the indenter which in reality is also in contact with the indenter is not accounted by the Oliver and Pharr method.

To obtain better approximations of the H and E_r contact areas were estimated from the AFM images using the Section analysis in the NanoScopeTM software. Nanoindentation residual impressions were subjected to quantitative horizontal analysis. For contact area approximations each of the three pile-ups around the indent were considered as semi-ellipses and the area inside the “triangle” was calculated using the Heron of Alexandria formula as shown in Figure 5.15.

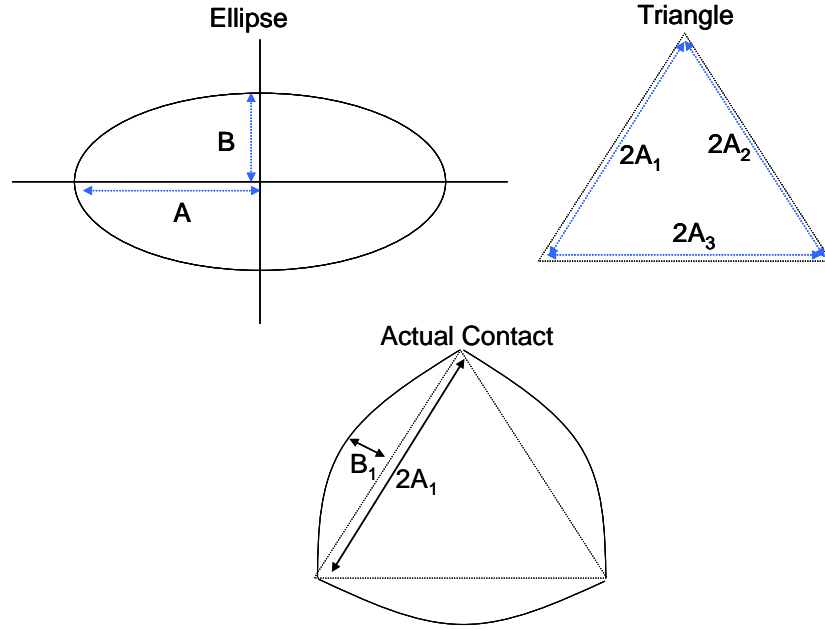


Figure 5.15 Geometrical figures utilized for contact area approximations from AFM nanoindentation residual impression.

The area of an ellipse is defined by:

$$A_{ellipse} = \pi A B \quad (5.7)$$

And the Heron of Alexandria formula for the area of triangle is

$$A_{triangle} = \sqrt{S(S-2A_1)(S-2A_2)(S-2A_3)} \quad (5.8)$$

Where S is defined by:

$$S = \frac{(2A_1 + 2A_2 + 2A_3)}{2} \quad (5.9)$$

By combining these geometrical figures the real contact area can be approximated by the contact areas contributed by the pile-ups:

$$A_{pileups} = \frac{A_1 B_1 \pi}{2} + \frac{A_2 B_2 \pi}{2} + \frac{A_3 B_3 \pi}{2} \quad (5.10)$$

Thus the total contact area can be approximated by:

$$A_{\text{contact area}} = A_{\text{pileups}} + A_{\text{triangle}} \quad (5.11)$$

Figure 5.16 shows a partial scene of the Section analysis in the NanoScope™ software performed on a 190 nm maximum displacement indent on a decanethiol SAM on Au (~20 nm thick). The horizontal distance measured on blue and red correspond to the distances $2A_1$ and B_1 both shown in Figure 5.15.

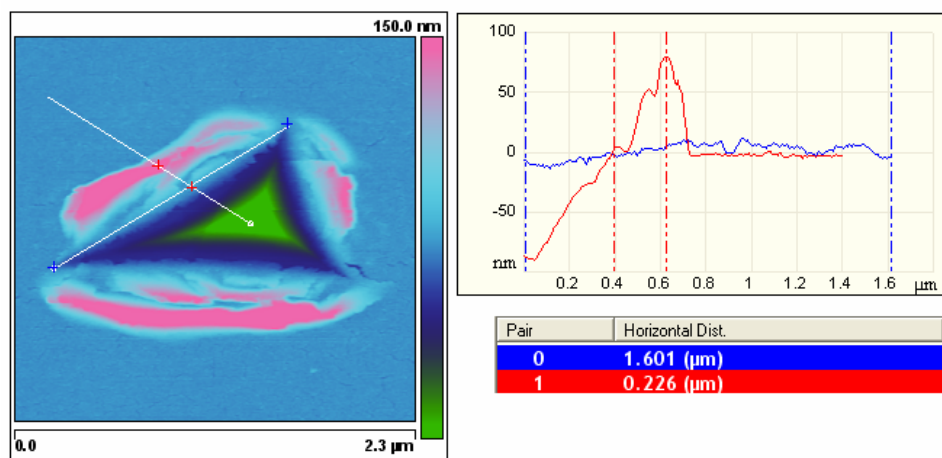


Figure 5.16 Partial scene of NanoScope software showing sectioning analysis for measuring horizontal distances used for contact area approximations.

Section analysis was performed to the three sides of the impression of the Berkovich indent. All the AFM images of indents on gold, octanethiol, decanethiol, and dodecanethiol SAMs were subjected to sectioning analysis. All the measured values of $2A_1$ and B_1 and the corresponding contact areas for all the indents can be found in Appendix I.

5.7 Results and Conclusions

5.7.1 Hardness from AFM Images

Since hardness is related to contact area errors in the Oliver and Pharr hardness are caused by not accounting for pile-up. The hardness results computed using the true areas of contact (H_{AFM}) are presented in Figure 5.17. As seen before with the Oliver and Pharr analysis the hardness increases with indenter displacement approaching the value of the glass substrate for the deeper displacements. An increase of 21% and 5% in H_{AFM} was observed when indenting the Octa/SAM and Dode/SAM compared to the H_{AFM} of the plain gold substrate when indented 40 nm deep. Then for the deeper indents (140 nm and 190 nm) the Octa/SAM decreased H_{AFM} of the gold by 10% and 8%. The Deca/SAM decreased H_{AFM} of the gold by 18%, 30% 10% and 26% when indenting 90 nm, 140 nm and 190 nm deep. The Dode/SAM also decreased H_{AFM} of its perspective gold substrate by 18%, 17% and 25% for the maximum displacements of 90 nm, 140 nm and 190 nm.

Table 5.3 Percentage decrease in H_{AFM} for indents with a SAM layer compared to indents on clean gold.

	40 nm	90 nm	140 nm	190 nm
Octa/SAM	↑ 21%	↑ 9%	10%	8%
Deca/SAM	18%	30%	10%	26%
Dode/SAM	↑ 5%	18%	17%	25%

As expected the effect of the different SAMs on the hardness (plastic deformation) is more pronounced than when analyzing the data with the Oliver and Pharr

method, though their predictions are reasonably correct for most materials except the ones that do not strain hardened.

As seen in Figure 5.17, the H_{AFM} corresponding to the different gold samples (blue squares in Figure 5.17a, b and c) varies between samples. In the case of maximum tip displacement of 190 nm deep, the hardness of the gold substrates used for growing the Octa/SAM and Dode/SAM both have H_{AFM} of 3 GPa whereas the gold film used to grow the Deca/SAM has a H_{AFM} of 3.7 GPa. The hardness is likely to be extremely sensitive to Au thickness when strain hardening occurs. However, when the SAM is present the hardness for 190 nm deep indents is very similar for all the films. This is consistent with reduced strain hardening.

In conclusion, the SAM decreased the H_{AFM} of the underlying gold, significantly when indenting the different films 90 nm, 140 nm and 190 nm deep. The chemical adsorption of the SAM onto the Au(111) modifies the surface stress of the clean gold, which normally favors the reduction of surface area. Surface stress can have considerably influence on the plastic behavior of a metal. Nuzzo⁸⁶ reported in 1990 that the enthalpy of formation (adsorption) of alkanethiols on gold (111) is exothermic with values between 126-150 kJ/mol. Since the reaction is exothermic the enthalpy of formation can be considered as negative. Mathur et al. mentioned in a Nature Materials correspondence⁸⁷ that if the enthalpy of adsorption is large enough it can result in an effective negative surface energy. Surface energy might make a contribution to what we see in the hardness and AFM images. Reactive environments can effectively give a negative surface energy. It is probable that the adsorption of alkanethiols on Au(111) is

also giving a negative (compressive) surface stress which may favor the increasing the surface area when the surface is indented.

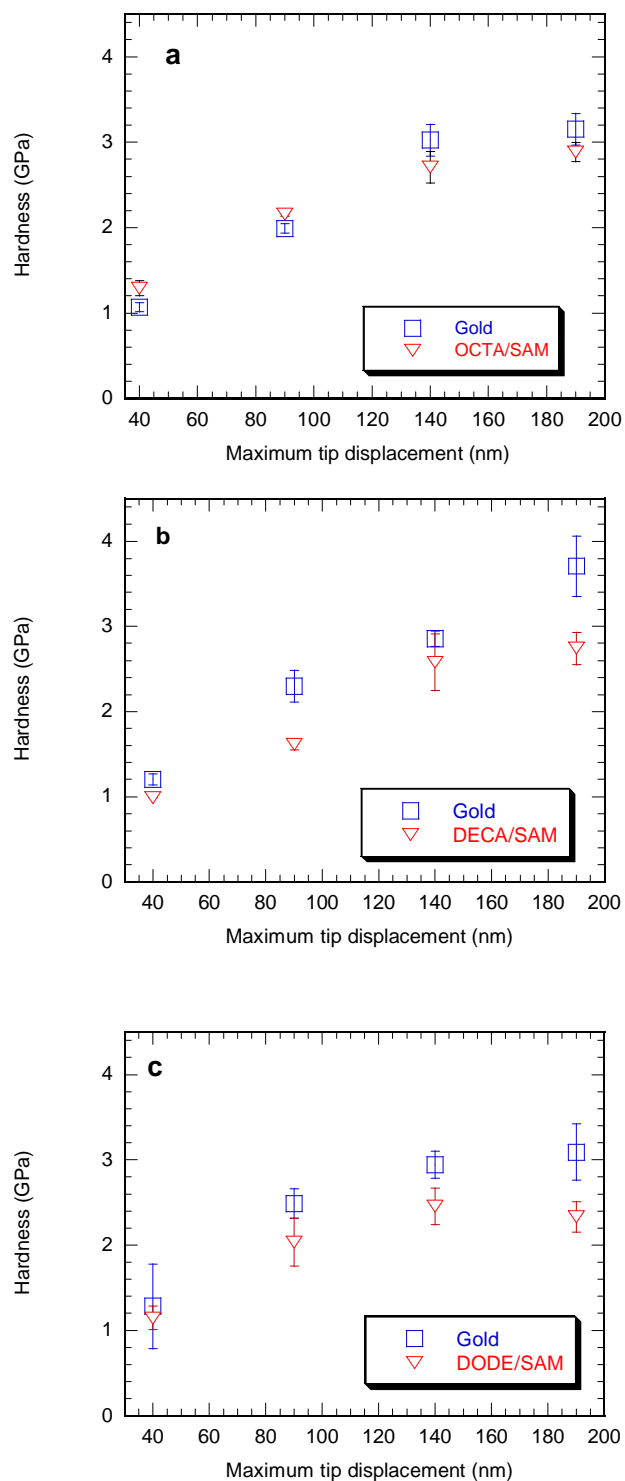


Figure 5.17 Comparison of hardness approximations (H_{AFM}) of gold and modified gold with SAM for (a) eight carbons SAM, (b) ten carbons SAM, and (c) twelve carbons SAM as a function of maximum nanoindentation displacements. Error bars correspond to standard error.

5.7.2 Reduced Elastic Modulus from AFM Images

Given that the interatomic forces determine the fundamental elastic behavior within metal crystals it is understandable that any restraint on the surface can modify the apparent mechanical properties to some extent. The chemical action of the alkanethiol SAM chemisorbed to the surface of gold modifies the surface stress of the gold and as a result it can also change the elasticity somewhat. The gold surface coated with a different material (the SAM) will have a more complex mechanical behavior than the gold alone. It seems likely that the elastic modulus of the two materials will average out in proportion to their relative areas within planes¹².

The calculated reduced elastic modulus based on the AFM contact areas (E_{AFM}) for the gold substrates and the different SAMs are plotted in Figure 5.18 as a function of nanoindentation maximum tip displacements (Figure 5.18(a) for Octa/SAM, (b) for Deca/SAM and (c) for Dode/SAM.). The reduced elastic moduli from AFM contact area also shows some dependence on indenter displacement especially for the shallow indents where the values are noticeably higher compared to deeper tip displacements.

Table 5.4 Percentage decrease in E_{AFM} for indents with a SAM layer compared to indents on clean Au(111).

	40 nm	90 nm	140 nm	190 nm
Octa/SAM	↑ 14 %	↑ 6 %	8%	8%
Deca/SAM	11%	21%	11%	19%
Dode/SAM	↑ 6%	11%	13%	19%

In the case of the Octa/SAM E_{AFM} increased by 14% and 6% when indenting the film 40 nm and 90 nm deep and decreased the modulus by 8% when indenting 140nm and 190nm deep. The Deca/SAM reduced E_{AFM} of the underlying gold film by 11%, 21%, 11% and 19% when indented 40 nm, 90 nm, 140 nm, and 190 nm deep. The Dode/SAM also increased E_{AFM} by 6% when indented 40 nm deep, while it decreased it by 11%, 13% and 19% for the maximum tip displacements of 90 nm, 140 nm and 190 nm. Tabulated data containing the averaged hardnesses and reduced elastic moduli obtained using the contact areas measured from the AFM images for both the Au films and modified Au with SAMs can be found in Appendix J.

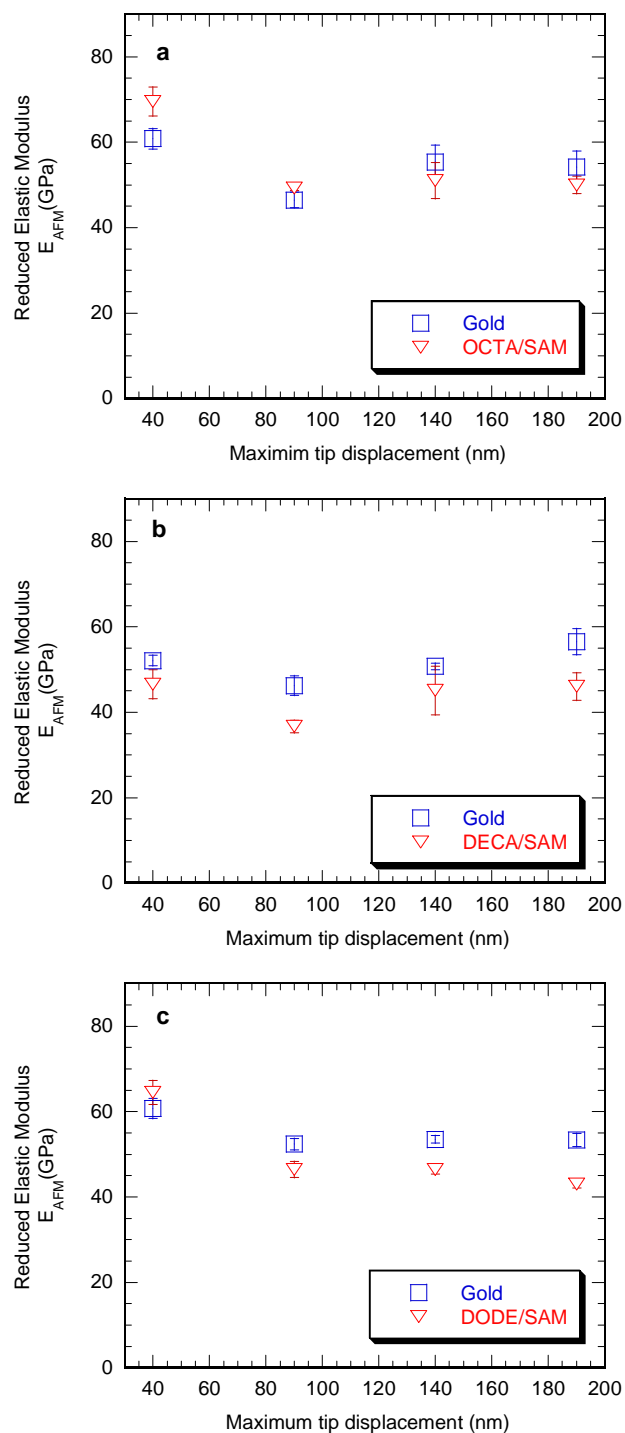


Figure 5.18 Comparison of reduced elastic modulus approximations of gold and modified gold with SAM for (a) eight carbons SAM, (b) ten carbons SAM, and (c) twelve carbons SAM as a function of maximum nanoindentation displacements. Error bars correspond to standard error.

5.7.3 Relationship between Hardness, Elastic Modulus and Work of Indentation

A relationship between the ratio of hardness to the elastic modulus and the ratio of irreversible work (permanent) to the total work of indentation was proposed by Cheng and Cheng⁸⁸ in 1989. Using this approach the ratio of hardness to elastic modulus can be found directly from the work of indentation instead of the maximum load and the slope of the unloading curve as used in the Oliver and Pharr method³¹. As previously stated this approach depends on estimating the contact area which is difficult to approximate when pile-up is present.

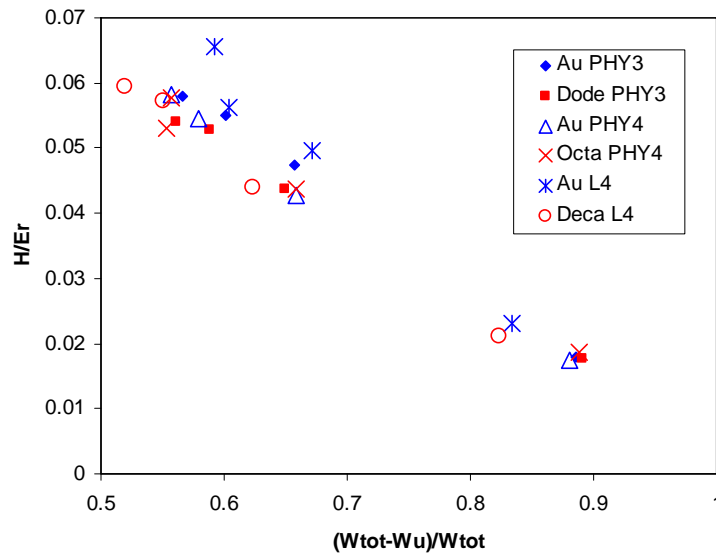


Figure 5.19 Ratio of hardness to reduced elastic modulus as a function of the permanent work (plastic) divided by the total work of indentation.

It is evident from Figure 5.19 that all the data lays approximately on a single curve. Consequently, as Cheng and Cheng proposed we can use the works of indentation to approximate the ratio of the hardness to the elastic modulus by:

$$\frac{H}{E_r} = \Pi_{\theta} \left(\frac{W_{tot} - W_e}{W_{tot}} \right) \quad (5.12)$$

where Π_{θ} is a dimensionless function.

Cheng and Cheng analysis does not suffer from the same problems as the Oliver and Pharr analysis when pile-up is present.

6 DISCUSSION AND GENERAL CONCLUSIONS

The freshly prepared gold and gold plus SAM films were subjected to a range of chemical and physical characterizations. The preferred gold film orientation obtained by evaporation of the gold onto clean glass substrates is usually the (111). This was confirmed by X-ray diffraction. A strong peak centered at a value of 2-theta of 38.55° confirmed that the (111) is the dominant orientation which is the preferred crystal face for alkanethiol SAM formation on gold. In addition, Raman spectroscopy and ellipsometry were employed to confirm the presence of the monolayers. In agreement with previous studies Raman peaks corresponding to the vibrations of CH_2 , CH_3 , and C-C were detected on the gold films modified with SAMs. An average thickness of 0.809 nm was obtained with ellipsometry for the decanethiol SAM which is in the range reported by other groups. Contact angle measurements were performed on the different chain length alkanethiol SAMs using three different measuring liquids. The Au(111) samples covered with the octanethiol SAM and dodecanethiol SAM increased the water contact angle of the underlying Au(111) from 79° to 95° and 87° respectively. Surface free energies were also calculated using the Owens-Wendt method. A decrease in the surface free energy of the underlying Au was reported as well when the different SAMs were present compared to the Au alone.

The hardness and reduced elastic modulus of the gold and modified gold films with different SAMs were calculated directly from the load-displacement curves using the Oliver and Pharr analysis. Additionally, since pile-up around the indent can affect the contact area and, hence, the measured value of hardness and reduced elastic modulus,

nanoindentation residual contact areas were measured from the AFM impression images. Comparing the corrected hardness (H_{AFM}) and reduced elastic modulus (E_{AFM}) with those derived from Oliver and Pharr (O&P) analysis provides information about how pile-up can lead to significant errors when estimating the contact area from the load-displacement curves. Table 6.1 compares the contact areas approximated using the Oliver and Pharr method with the areas directly measured with the AFM image analysis of the residual nanoindentation impressions of the indents performed on the dodecanethiol SAM. This particular example shows clearly the degree of underestimation of the contact areas when pile-up is present. Since hardness and contact area are related to each other, error in the Oliver and Pharr hardness is caused by not accounting for pile-up.

Table 6.1. Comparison between the projected areas of contact estimated from the Oliver and Pharr (O&P) method and areas approximated from the AFM images of the nanoindentation residual impressions on Dode/SAM. Negative % of difference corresponds to under estimation of the area of contact.

Max. tip displacement (nm)	Area of Contact From AFM images (nm ²)	Area of Contact From O&P Analysis	% diff
40	150627	124550	-21
40	131487	125277	-5
90	523889	326398	-61
90	554486	332222	-67
90	457925	325813	-41
90	412900	333712	-24
140	885797	648893	-37
140	882254	640367	-38
140	992426	638411	-55
140	1065107	638017	-67
190	1749235	1047560	-67
190	1810983	1027175	-76
190	1744285	1032473	-69
190	2037454	1051360	-94

The calculated hardness and elastic modulus for all the experiments are shown in Figure 6.1 and Figure 6.2. Both the hardness and reduced elastic modulus obtained with

the Oliver and Pharr analysis (without accounting for pile-up) are higher than the values estimated from the real contact areas. Additionally, the effects of the SAM on the plastic deformation of gold are clearer from the comparison of the hardnesses calculated from the AFM contact areas. By using the O&P, no significant difference in the hardness was seen between the Au and the Octa/SAM, however when introducing the effect of the pile-up on the contact area, the hardness was increased for the shallow indents by 20% when the Octa/SAM was present. The increase in the hardness for the shallow indents is consistent with the AFM images that showed less plastic deformation for this particular case.

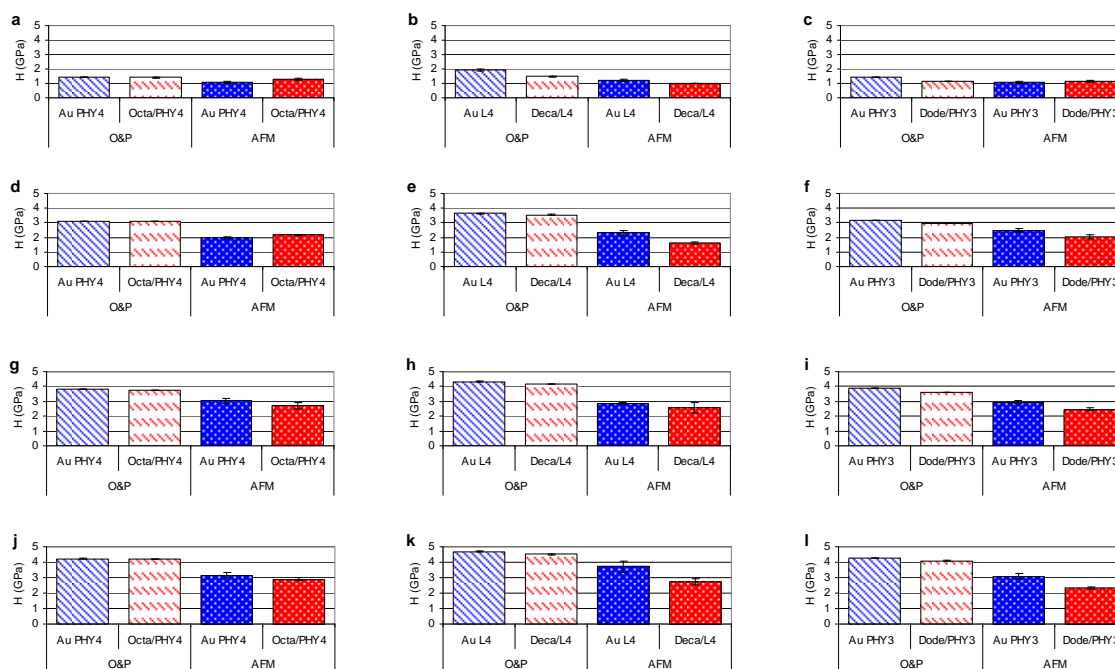


Figure 6.1 Comparison between hardnesses computed using the true contact areas and hardnesses computed using Oliver and Pharr analysis for (a, d, g and j) Octa/SAM, (b, e, h, and k) Deca/SAM and (c, f, i, and l) Dode/SAM and their respective gold substrates. The first row (a, b, and c) corresponds to 40 nm maximum tip displacement, the second row (d, e, and f) to 90 nm, the third (g, h, and i) to 140 nm and the fourth row (j, k, and l) to 190 nm. Error bars correspond to standard error.

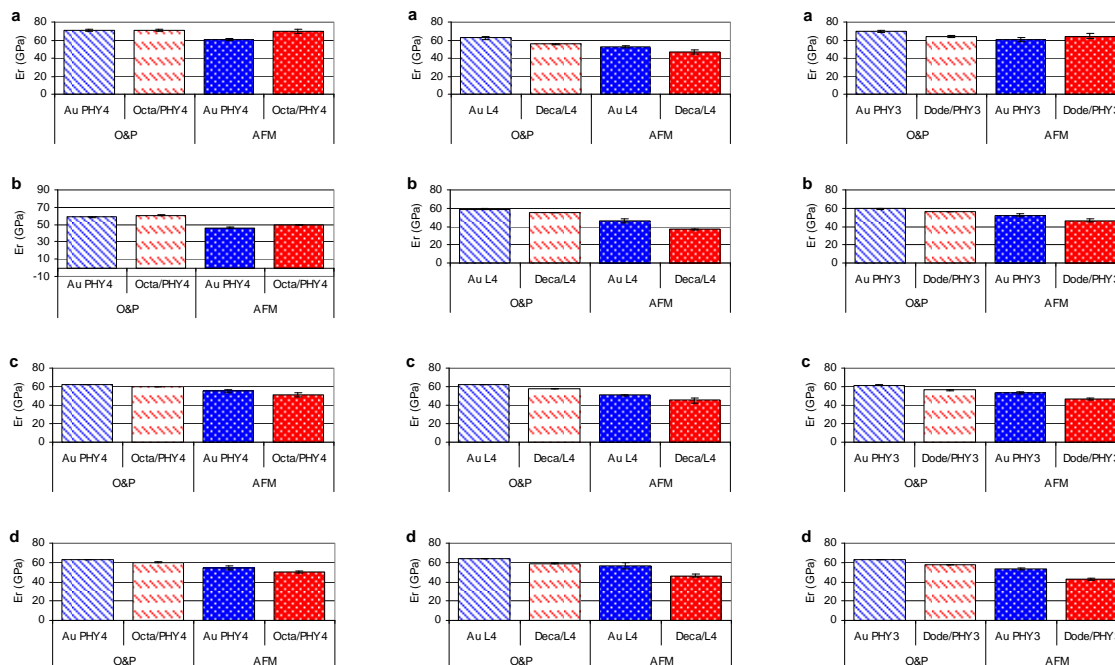


Figure 6.2 Comparison between reduced elastic moduli computed using the true contact areas and using Oliver and Pharr analysis for (a, d, g and j) Octa/SAM, (b, e, h, and k) Deca/SAM and (c, f, i, and l) Dode/SAM and their respective gold substrates. The first row (a, b, and c) corresponds to 40 nm maximum tip displacement, the second row (d, e, and f) to 90 nm, the third (g, h, and i) to 140 nm and the fourth row (j, k, and l) to 190 nm. Error bars correspond to standard error.

Even though the different SAM layers are a few nanometer thick (Deca/SAM: 0.890 nm measured with ellipsometry; Octa/SAM: and Dode/SAM: 0.74 nm and 1.25 nm respectively measured by Del Rio et al.⁸⁹) it was found that they have a significant effect on the reduced elastic modulus and hardness measured by nanoindentation. The elastic modulus of the system should not show a significant difference when the SAM is present since it is a tiny volume compared to the Au and the glass. A 1 nm thick layer of negligible stiffness would be expected to have little effect on contact stiffness at a depth of 190 nm. At shallow depths one way in which the SAM can modify the measured elastic modulus is by acting as a compliant elastic film and changing the elastic field

distribution from the Sneddon approximation used in the analysis and, hence, lowering the elastic modulus value. The contact between the gold surface and the SAM has a more complex geometry than the elastic half-space assumed by Sneddon. Specifically, pile-up effectively blunts the tip in terms of both contact area and stress distribution. Since gold and glass have similar elastic moduli there is no reason to expect a variation in the reduced elastic modulus of the Au/glass substrate with indent depth, or with the presence of the SAM layer, since it is negligible in volume compared to the gold and glass. Volume dependent models for elastic modulus, such as those based on the isostrain and isostress extremes, show that a 1 nm SAM can at most cause a change in contact compliance <1% for indents >100 nm.

Recent work by DelRio et al. measured the elastic modulus by atomic force microscopy of alkanethiols on gold. In their study, as the chain length n decreases from 18 to 5 the elastic modulus of the monolayer decreased from 1.0 to 0.15 GPa⁹⁰.

One of the most interesting and surprising results is the effect of surface chemistry on plastic deformation. When a solid is deformed work is performed against both the volume and surface forces. Under most conditions the volume strongly dominates over the surface. However, for solids of small extent, the surface term can become important. The SAM layer has been shown to have an effect on the hardness of the underlying gold surface and intriguingly the effect is different when indenting the sample 40 nm deep compared to the deeper maximum tip displacements. In the case of the shallow indents, on average the new surface area created (Δ surface area) by indenting the Deca/SAM and Dode/SAM compared to just their gold substrates decreased for only the shallow indents (40 nm deep). For all deeper indents Δ surface area increased for the SAM/Au compared

to Au alone. Additionally, the hardness was increased only when the Octa/SAM and Dode/SAM were indented 40 nm deep. This effect at shallow depth can be explained by the effect of attractive forces between the Au surface and the indenter at the nanocontact as described by the contact mechanics models JKR and DMT discussed before. As said before, when the indenter tip is in contact with the surface, there is an additional load due to adhesive forces. Commonly the JKR model which considers the contact to be adhesive and assumes the formation of a capillary neck is more appropriate for soft materials with high surface energy, such as gold. SAMs have been commonly used to decrease these attractive forces during indentation tests. One possible explanation for the increase in the hardness and decrease in the pile-up when the SAM is present (only in the case of 40 nm maximum displacement since the attractive forces will be small in comparison to the indent load at larger depths) is that the SAM layer is reducing the attractive forces between the nanoindenter tip and the gold surface. This decreases the plastic deformation of the underlying gold when it is indented.

To support the statement that the SAM layer reduces the attractive forces (only for the shallow indents) the case of the Dode/SAM, where it decreased the pile-up height by 8% and the Δ surface area by 14% when indented 40 nm deep compared to its gold substrate is evaluated. The JKR model modifies the Hertz model (the simplest; does not take into account external load; neglects adhesion between the indenter and the sample) by incorporating the formation of a capillary neck between the indenter tip and the sample due to adhesion forces in the contact area (even at zero load, and will persist as the tip is retracted).

The pull of force at which the tip separates from the surface and the neck is broken can be calculated by:

$$F_s = -3\pi R \gamma_s \quad (6.1)$$

where R is the radius of curvature of the tip and γ_s is the surface free energy. For a Berkovich tip R is usually between 100 nm - 200 nm. For the following calculation a value of 150 nm for R was assumed. The surface free energy of the gold γ_{gold} is taken as 0.790 J/m² (theoretical value) and for the Dode/SAM surface γ_{SAM} as 0.01932 J/m² (measured using the Owens-Wendt method). Using equation 6.1 the load at which the tip and the surface neck separates (F_s) is equals to -1.117 μN for the gold alone and -0.026 μN when the SAM layer is present.

The Hertz equation of contact area modified by JKR to take into account the surface energy effect is:

$$A = \pi \left(\frac{R}{K} \right)^{2/3} \left(P + 3\pi\gamma R + \sqrt{6\pi\gamma R P + (3\pi\gamma R)^2} \right)^{2/3} \quad (6.2)$$

where K is the elastic modulus (78 GPa for clean gold) and P is the applied force perpendicular to the surface. In the case when the tip is in contact with the surface and the applied load is zero (P=0), the contact area for clean gold is 8.4x10⁻¹⁶ m² and for the Dode/SAM 6.99x10⁻¹⁷ m².

For the deeper indents, 90 nm, 140 nm and 190 nm, the hardness of the underlying gold dramatically decreased when the SAM was present. A decrease in hardness is a direct indicator of an increase in the plastic deformation. In Chapter 5, AFM

characterization of the residual impressions showed a substantial difference in the indent geometry between Au with SAM (most dramatically for the Deca/SAM and Dode/SAM) and Au substrate alone. In the case of the deeper indents the greater pile-up heights and surface areas suggest an increase in the plastic deformation. However, the plastic work is less when the SAM is present as seen in the work of indentation analysis. Essentially, in the presence of the SAM there is more plastic deformation but less work was required to create new surface. Various factors can contribute to the effect of the SAM on the plastic deformation of the gold. The first one to be discussed is the surface free energy. The exothermic reaction of the SAM chemisorption reduces the surface free energy of the gold. Lowering the surface free energy of a substrate implies that less work per unit area is necessary to form new surface since exposing new atom releases energy. A theoretical value of 790 mJ/m^2 for the surface free energy of clean Au(111) has been calculated using the embedded atom method potentials as reported by Gumbsch²¹. The surface energy of our gold substrates covered with Octa/SAM and Deca/SAM were extracted using the Owens-Wendt method. A surface free energy of 21.63 mJ/m^2 for the Octa/SAM and 19.32 mJ/m^2 for the Deca/SAM were obtained using three different measuring liquids. It is possible that the effect of the SAM on the surface free energy of the gold contribute to the increase in the plastic flow during indentation. Since the SAMs lower the surface free energy of the gold then less work is required to create new surface. However, the difference between the work of indentation when indenting the SAM surfaces compared with the gold alone is too large to be explained alone by the difference between their surface free energies. Essentially the energy associated with creating the pile-up surface is different for the SAM/Au compared to the Au, but orders of magnitude

less than the difference in the work of indentation. Thus, a combination of things is more likely affecting the plastic deformation than surface energy alone. This is what brings us to the next factor that can be contributing to the effect on the plastic deformation: surface stress.

When considering solid surfaces, surface stress needs to be considered. The surface of gold is considered to be in tensile stress due to the fact that the surface atoms have a lower electron density. The atoms from the gold surface prefer to adopt a smaller equilibrium spacing normal to the surface than the bulk atoms in order to increase the local electron density (Figure 6.3a). An average tensile surface stress for clean gold of $1,175 \text{ mJ/m}^2$ was experimentally measured by electron diffraction by May and coworkers²². There is relatively little information concerning the mechanical properties of SAMs, particularly the nature of the surface stress. The previous reports of surface stress for alkanethiol monolayer formation that can be found in the literature^{6,7} include a study performed by Godin et al.⁵. This showed the surface stress induced by the formation of dodecanethiol SAM on Au(111) as it developed in real time. An induced compressive surface stress resulted from the formation of dodecanethiol SAM on Au(111). In their study the compressive surface stress was dependent on the size of the substrate gold grains, resulting in 510 mJ/m^2 for formation on the small grains (90 nm) and $15,900 \text{ mJ/m}^2$ on the large grains (600 nm). It is postulated that surface stress can also contribute to the increase in the plastic flow when indenting the gold surfaces covered with different SAMs. Clean gold has a tensile surface stress, meaning it wants to reduce its surface area. A tensile surface stress can be seen as giving repulsive image forces on dislocations (force which characterizes the interaction between the dislocation

and the free surface). Basically, if image forces are repulsive, dislocations won't egress at the surface, thus creating a strain hardening effect in the material, in this particular case, the gold substrate. In the contrary, the chemisorption of the alkanethiol molecules onto the gold causes the surface to have a compressive surface stress, as shown in Figure 6.3c, due to the chemical bond of the sulfurs in the SAM's head group with the surface gold atoms. It has been suggested that the SAM chain spacings are equal to $\sqrt{3}$ of the second nearest neighbor gold spacing. Thus the monolayer is indeed densely chemisorbed to the Au(111) hexagonal lattice. Chemisorption of the SAM changes the electron density of the gold surface layer reducing the density of atoms at the surface. After monolayer formation the gold atoms do not need to reduce the spacing to increase the electron density any more, in contrast the opposite is true and the surface is considered to be under a compressive stress. The compressive surface stress induced by the adsorption of the SAM has been found to be proportional to the number of molecules adsorbed and a slight dependence on the chain length.

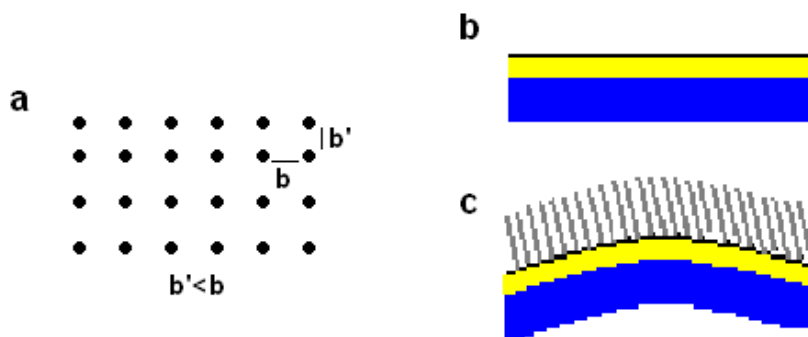


Figure 6.3 (a) Surface stress in gold surface. Surface atoms are strained, and the surface has a stress exerted on it by the underlying lattice. (b) Sketch showing a perpendicular cross section of the evaporated gold on glass and (c) the same surface under compressive surface stress caused by monolayer formation.

The effect of a surface layer on the plastic deformation can also be seen in dislocation nucleation induced by the SAM, a similar effect is seen in dislocation piling-up on an oxide layer. From the mechanical point of view, one of the fundamental parameters affecting the elastic/plastic deformation during nanoindentation is the strain hardening rate. Strain hardening, the strengthening of a metal by dislocation accumulation in the gold occurs during plastic deformation. Too many dislocations prevent new dislocations from nucleating, creating a resistance to dislocation formation. It is suggested from AFM data that the pile-up is more significant for the deeper indents when the SAM is present because the compressive surface stress introduced by the SAM adsorption favors dislocation to escape at the surface. When dislocations move to the surface the surface applies a force on the dislocation, the image force. The compressive surface stress induced by SAM formation reduces the dislocation density and helps dislocations to nucleate and increase the plastic flow. The SAM coated surface under compressive stress helps create new surface as the elastic separation of the atoms at the

surface enhances image forces. The exothermic reaction of the SAM also favors dislocations to escape to the surface. AFM images revealed that the clean gold substrates compacted more under the load of the indent, whereas gold with the SAM layers prefers to flow plastically showing higher and wider pile-ups. The volume of the pile-ups and the volume of the indent impressions (that is the empty volume created by the indent below the original surface as shown in Figure 6.4) were calculated from the AFM residual impressions performed with the nanoindenter at 90 nm, 140 nm and 190 nm maximum tip displacements on the different SAMs and their respective clean Au(111) substrates.

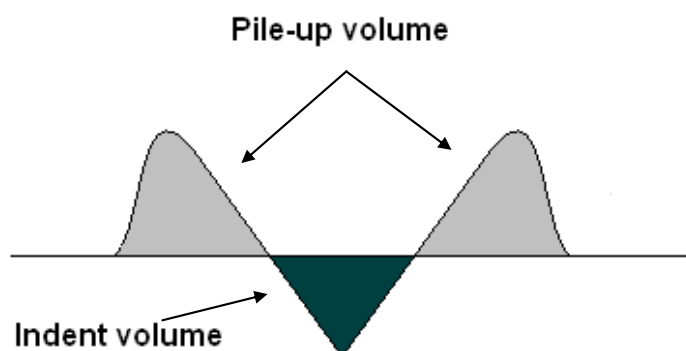


Figure 6.4 Scheme distinguishing the pile-up and indent volume.

It is well known that strain hardening leads to densification. Calculations of the ratio of the pile-up volume to the indent volume showed that more volume was compacted under the indentation of clean Au compared to the Au+SAMs. Thus, there is greater densification with the Au compared to the Au+SAMs making the argument of strain hardening valid. Figure 6.5 compares the pile-up volume created when indenting

the clean Au(111) substrate with the volumes created when indenting the same substrate after SAM inclusion. As shown in Figure 6.6 the extent of the pile-up volume increased by 52%, 105% and 206% when indenting the Dode/SAM 90 nm, 140 nm, and 190 nm deep compared to the clean Au substrate. Averaged pile-up volumes can be found in Appendix J.

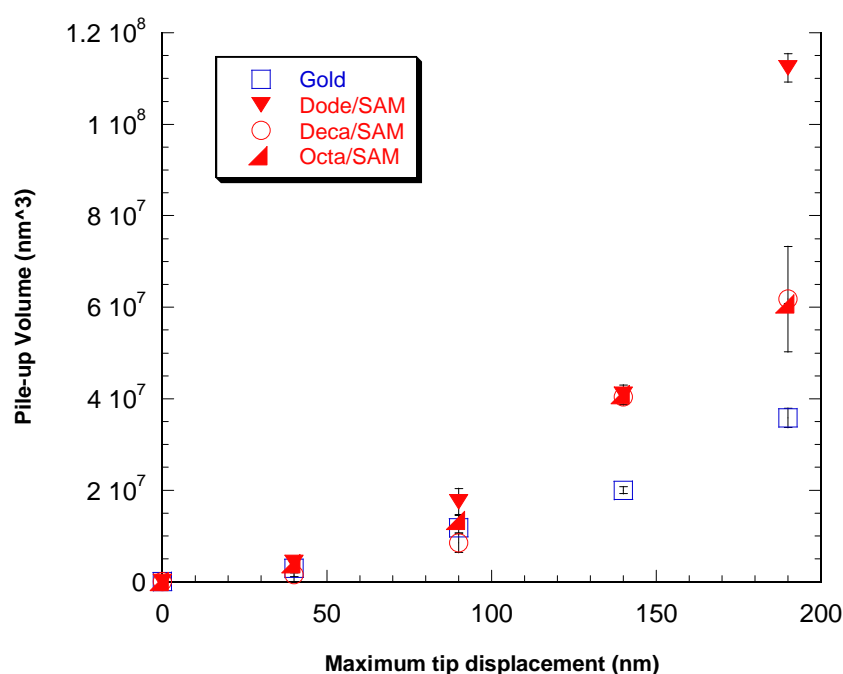


Figure 6.5 Comparison between pile-up volumes created during nanoindentation of clean Au and modified Au with Octa/SAM, Deca/SAM and Dode/SAM.

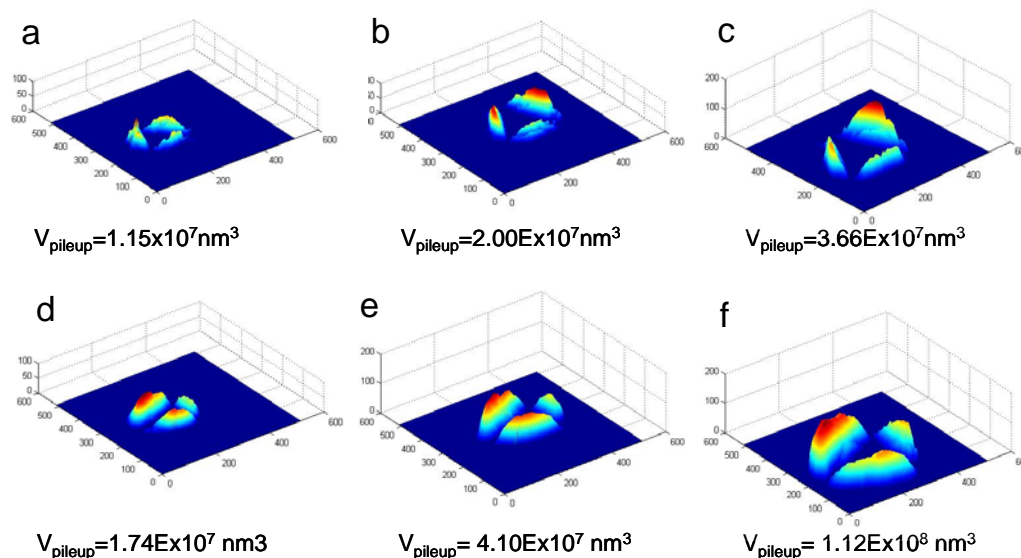


Figure 6.6 Three dimensional height profiles comparing the pile-up volume created during nanoindentation of clean Au (a, b, and c) and modified Au with Dode/SAM (d, e and f). Maximum tip displacements of (a and d) 90 nm, (b and e) 140 nm, and (c and f) 190 nm.

This study has been able to show some of the effects of surface chemistry on mechanical properties. It is extremely hard to study chemomechanical effects. For a given experiment considerable variability was obtained in preliminary studies between the results from different gold films. Strain hardening is extremely dependent on gold thickness and a small change in this can give a significant change in plasticity. That is why for every SAM system discussed in this thesis the mechanical properties of the SAM system is directly compared with the mechanical properties of the respective underlying gold substrate. To minimize any gold thickness gradient introduced by the positioning inside the gold evaporator, after gold deposition, each sample was marked using the nanoindenter, near the center of the sample. Indents on the gold sample were performed 50 μm apart from the mark and after AFM the same sample was covered with the SAM. The Au+SAM samples were indented 50 μm from the indents performed on just the Au

so the thickness was the same. Some other factors that can affect the results are the environmental humidity and the time elapsed between SAM formation and nanoindentation test. He-diffraction and STM studies have indicated that it takes a few days after the sample has been taken out of the solution for the SAM to complete ordering.

SAM chain length seems to also play an important role in the nanomechanics of the SAMs on Au. Our findings suggest that longer chain lengths lead to stronger intermolecular van der Waals attractions between the alkane chains giving better packed monolayers. The mechanical effect of the SAM in our results showed less difference between the gold and the Octa/SAM (the shorter length SAM investigated) than the Dode/SAM. This can be explained as a result of a decrease in the packing density and order in the Octa/SAM compared to the Dode/SAM. Short chain length SAMs such as octanethiol can be considered to have a relatively unordered architecture whereas the SAM with a longer chain, dodecanethiol, forms a monolayer with a higher degree of ordering. Several studies have studied and shown the SAM chain dependence on packing and ordering by contact angle measurements, STM and AFM^{91, 92, 46}. The Deca/SAM showed similar results to the Dode/SAM.

Many new and intriguing questions have emerged through this research. In the near future, it will be very valuable and interesting to study the effect of the grain size of the gold substrate on the SAM packing density, and consequently, the mechanical effect in the gold when subjected to an external load. Additionally, a supplementary study of the effect of gold thickness on the mechanical properties could be undertaken since it is expected to influence greatly the strain hardening rate. Finally, functionalized SAMs

with different terminal groups can help better understand the effects of surface adhesion and surface free energy, this is potentially a way to control surface properties while simultaneously studying mechanical behavior.

7 ADDITIONAL WORK

7.1 Self-Assembled Monolayer Photopolymerization

7.1.1 Introduction

SAMs potential as ultrathin protective films and for various technical applications arises from many of their qualities such as strong adhesion to the substrate and the ability to change their terminal group, chain length and degree of cross-linking within the layers.

The creation of nanostructures by crosslinking and polymerization of the SAM terminal group using ultra violet light was studied. Polymerization of exposed vinyl tails containing a double carbon bond by photopolymerization and cross-linking was attempted. These nanostructures intended to serve as templates on porous membranes for studies of cells on controlled substrates.

The photoinduced polymerization of thiol-acrylate under UV light has been previously achieved by Lecamp et al⁹³. Later, photopolymerization of thiol-allyl-ether and thiol-acrylate coatings using photoinitiators and visible light was accomplished by Burget et al⁹⁴. Our goal was to combine some of these achievements and recreate the polymerization, but in a controlled way using SAMs that are chemically bonded to the surface as the foundation for three dimensional structures. The ultimate objective was to have a polymerizable SAM that could be patterned with a Near Field Optical Microscope (NSOM).

7.1.2 Materials and Methods

Glass coverslips were sonicated for eight minutes with acetone, methanol and ethanol. A 20 nm thick gold film was evaporated on the clean coverslips using highly pure gold pellets. Thiols terminated in the vinyl group $[\text{HS}-(\text{CH}_2)_9-\text{CH}=\text{CH}_2]$ with molecular weight of 186.36 g/mol and a density of 0.84 g/mL (at 24° C) were obtained from ProChimia (Poland). A 1.5 mM solution of ethanolic vinyl terminated alkanethiols was prepared in a dark room to avoid polymerization of the molecules before SAM formation. The resulting gold coated films were immersed for 24 hours in the solution. Monolayer adsorption was carried out in a glass weighting bottle. Raman measurements were performed over the spectral range of 80 to 3250 Raman shift/ cm^{-1} using a Renishaw inVia Spectrometer. A 785 nm laser on regular mode was focused on 10 different regions using a Leica microscope with a 50x0.75 NA objective. Only 10% of the total power of the laser (total power: 300 mW) was used, 1200 I/mm (633/780) grating and a 10 second exposure time. The surface topography was imaged using an atomic force microscope (NanoScope IV). All procedures were performed in the dark. A nine watt ultra violet lamp including two different wavelengths was used to polymerize the monolayer. Three samples were exposed to different sources of UV light. The photochemical reactions were carried out in a dry state. The first sample was exposed for 10 minutes to midday sun light, the second sample to 1 minute and then 4 minutes to 368 nm wavelength U.V. and the third sample was exposed to 254 nm U.V. light for 2 minutes. Raman spectroscopy and atomic force microscopy were performed after each exposure.

7.1.3 Results and Conclusions

Figure 7.1 shows a Raman spectrum corresponding to the vinyl terminated SAM on Au(111) showing the Au stretch, CH₂ rock twist, CH₂ scissor, C-C stretch, and C=C vibrations. The presence of the C=C peak confirms that there is a vinyl SAM on the gold substrate.

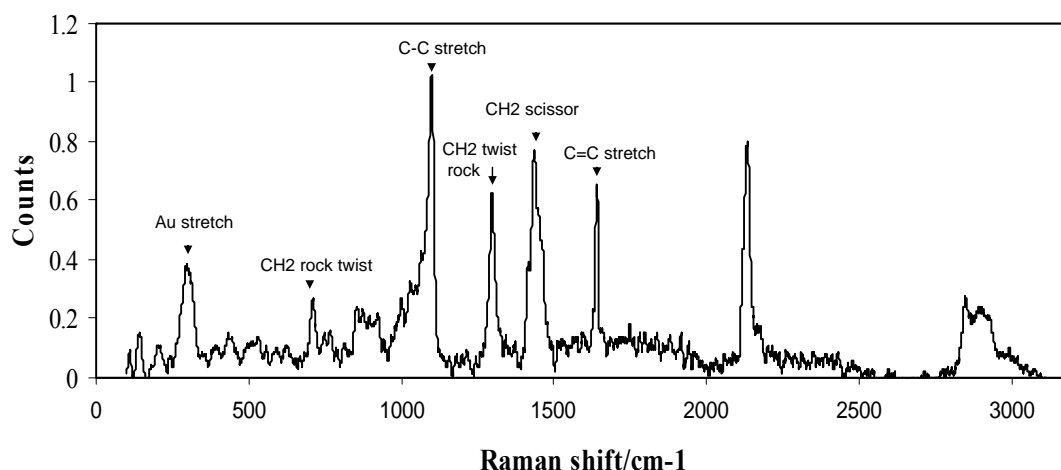


Figure 7.1 Raman spectrum of vinyl terminated SAM on evaporated gold film.

The intensity (counts) of all the Raman spectra were normalized with respect to the C-C (1098 shift/cm⁻¹) vibration. Figure 7.2 shows the averaged normalized spectra focused on the C=C stretching vibration for the vinyl terminated SAM kept in the dark and the vinyl/SAMs exposed to the different sources of illumination. In blue (Figure 7.2), the higher peak corresponds to the sample never exposed to any source of UV light. Then in red, a lower peak corresponds to the vinyl/SAM exposed for 1 minute to 368 nm. A decrease in the C=C intensity with respect to the C-C vibration corresponds to the breaking of the C=C bond due to a photochemical reaction. The same sample was later exposed to four more minutes under the 368 nm light (light green curve in Figure 7.2).

However, little difference is seen in the intensity. The lower peak in Figure 7.2 (dark green curve), corresponds to the vinyl/SAM exposed for 10 minutes to midday sun light.

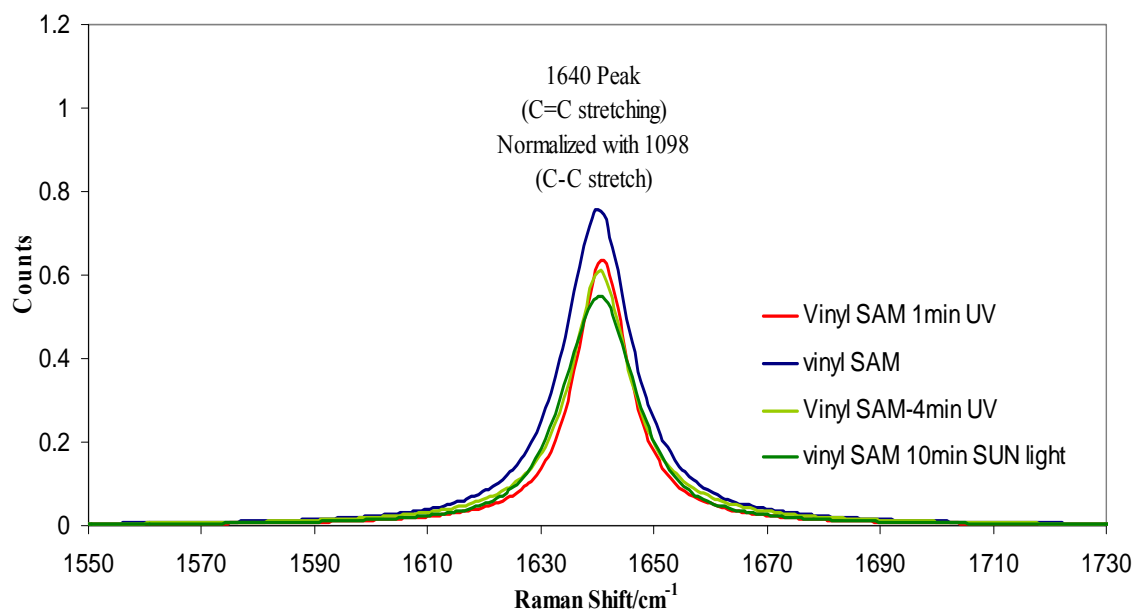


Figure 7.2 Normalized Raman spectra showing bond dissociation of the 1640 shift/cm⁻¹ (C=C stretching).

After 10 minutes of sun exposure the C=C vibrations intensity decreased to 0.55 counts compared to 0.80 counts for the vinyl/SAM never exposed to UV. Figure 7.3 shows three dimensional AFM height images of the topography of the vinyl/SAM and the photopolymerized surface after four minutes of UV (368 nm) light. The average image roughness (Rq value) decrease from 0.495 nm for the vinyl/SAM to 0.282 nm after exposure to UV.

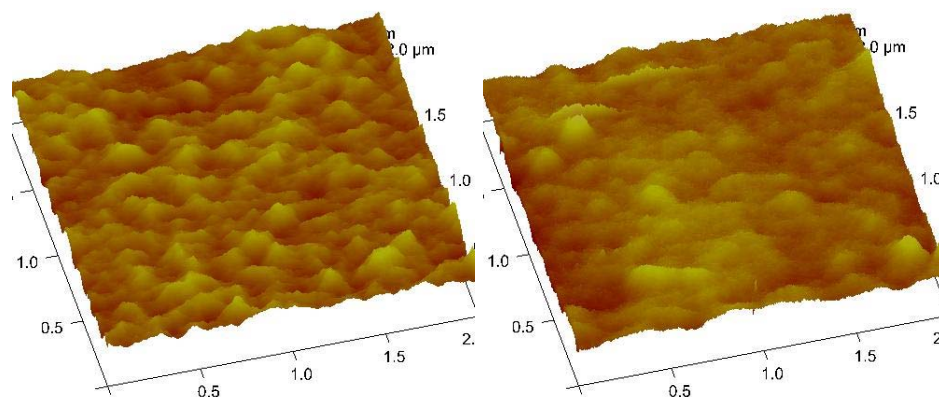


Figure 7.3 AFM three dimensional images ($2\ \mu\text{m} \times 2\ \mu\text{m}$) of vinyl terminated SAM (left) kept in the dark during and (right) same sample after 4 minutes of U.V. light exposure ($\lambda=368\ \text{nm}$).

The photopolymerization of the vinyl SAM was also attempted in situ during AFM imaging. AFM experiments were conducted in the dark with only a safe red light for illumination. The vinyl/SAM kept in the dark was imaged with the AFM. The top part of Figure 7.4 shows a $1\ \mu\text{m} \times 1\ \mu\text{m}$ topography and 3D AFM image corresponding to the unexposed vinyl/SAM. After imaging, the sample was exposed for two minutes to 254 nm energy. The same area of the sample was re-scanned after UV exposure (Figure 7.4 bottom).

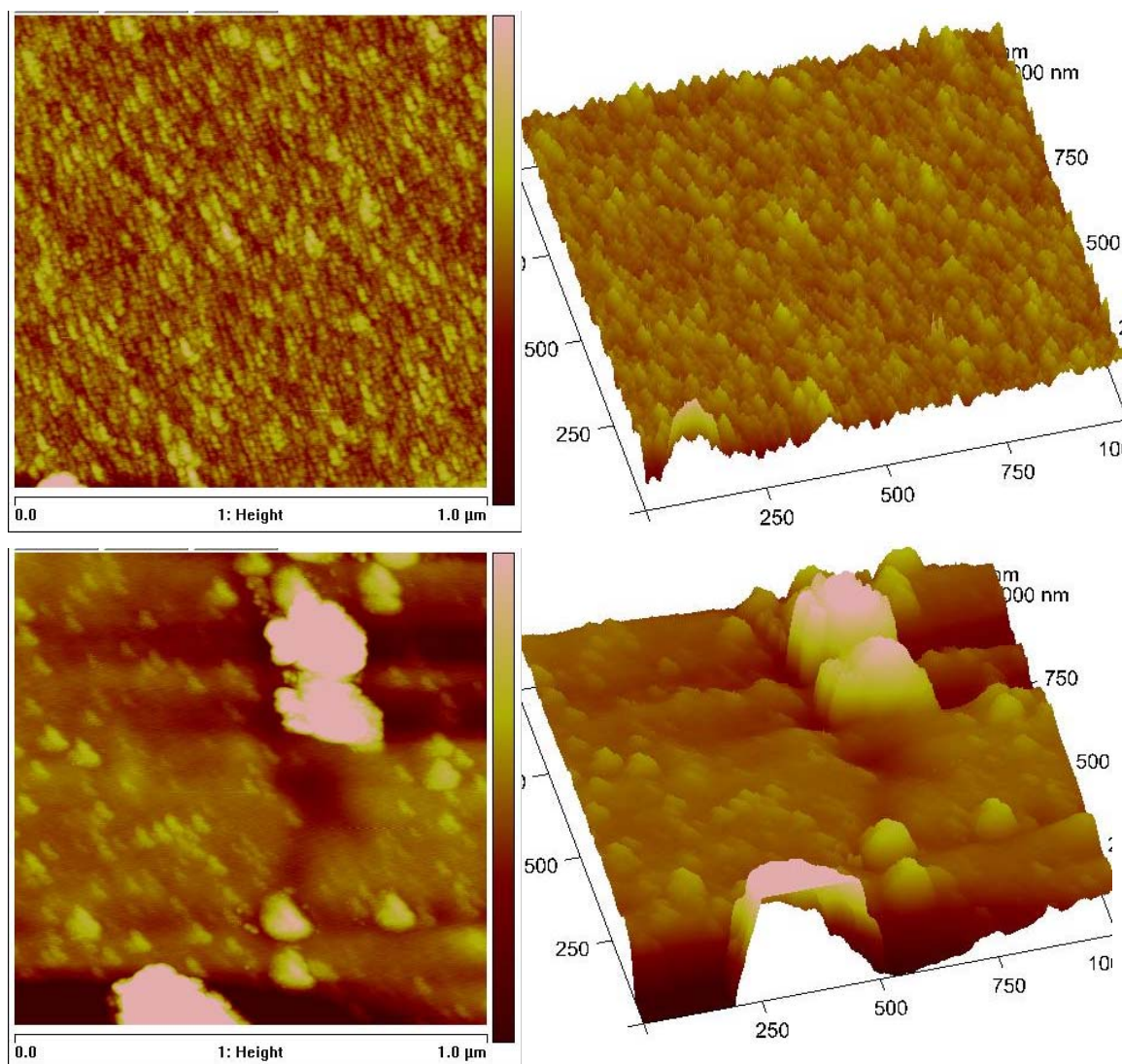


Figure 7.4 AFM height and three dimensional images of (top) a vinyl terminated SAM on gold and (bottom) the same area of the vinyl SAM after 2 minutes of in situ ultra violet ($\lambda=254$ nm) exposure. Color contrast corresponds to height for a maximum height (white) of 10 nm.

The energy of the 254 nm laser (4.88 eV) was too high for the polymerization of the vinyl/SAM. As can be seen in Figure 7.4, the vinyl layer has formed large mounds. This suggests the photons from the lamp are powerful enough to penetrate the monolayer and break the Au-S bonds (145 kJ/mol) that make the monolayer. Agglomeration of the polymerized molecules give rise to the large mounds visible in the AFM image. For the

longer wavelength, 368 nm (3.37 eV), the energy of the source is very similar to the $\text{CH}_2=\text{CHCH}_2$ double bond dissociation energy of 3.5 eV⁹⁵.

This project did not produce the uniform polymerization of the vinyl SAM that was anticipated. Instead the SAM layer was found to polymerize as discrete agglomerated mounds or to resist polymerization. Given the results of the preliminary studies it was considered not to continue with the project.

7.2 Proliferation and Mineralization of Human Osteosarcoma Cells on Different Polyarylates and Polycarbonates Substrates

7.2.1 Introduction

This work was done in the Cell Biology & Neuroscience Department as a part of an Integrative Graduate Education and Research Training (IGERT) founded by NSF. The goal of this research was to characterize *in vitro* the response of human osteosarcoma cells to various polymer substrates and to establish a correlation between cellular response and polymer chemistry/structure. In this particular project mineralization by a human osteosarcoma cell line, Saos-2, grown on various polymers was examined. The biodegradable and biocompatible polymers examined are members of the "polyarylate" and "polycarbonates" combinatorial library developed in Dr. J. Kohn's research group at Rutgers University⁹⁶. Alizarin Red-S assay was used to compare the extent of mineralization by the Saos-2 cells on each of the substrates.

7.2.2 Materials and Methods

Tyrosine-derived polyarylate- and polycarbonate-coated glass coverslips were prepared in Kohn's lab at Rutgers University. Chemico-physical properties affecting polymer flexibility, protein adhesion and degradation were altered by the inclusion of desaminotyrosyl-tyrosine (DT), poly(ethylene glycol) (PEG), and iodine (I₂) into the backbone of the poly(DTE carbonate), and by alterations in the pendent chain and diacid component of the polyarylate family of polymers. The details about design, synthesis, characterization and applications of these two families of tyrosine-derived polycarbonates and polyarylates have been described elsewhere⁹⁶.

Polyarylate coverslips were attached to the wells of a 24-well tissue culture plate using silicone grease. Four identical plates were prepared and labeled with a code (Table 7.1). Polycarbonate coverslips were also attached to the wells of a 24-well tissue culture plate, again using silicone grease and four identical plates were prepared and labeled with a code (Table 7.1). All the plates were sterilized by exposure to U.V. light.

Table 7.1 Polyarylate Series. Code number and polymer.

Code	Polyarylate
1	Poly(DTE suberate)
2	Poly(DTB suberate)
3	Poly(DTH suberate)
4	Poly(DTO suberate)
5	Poly(DTD suberate)
6	Poly(DTE succinate)
7	Poly(DTH succinate)
8	Poly(DTD succinate)
9	Poly(DTE dodecandioate)
10	Poly(DTH dodecandioate)
11	Poly(DTD dodecandioate)
12	Poly(DTH adipate)
13	Poly(DTH sebacate)
PLGA	Poly(DL-lactate co-glycolate)
PLA	Poly(DL-lactate)
TCP	Tissue Culture Plastic-Control

Table 7.2 Polycarbonate Series. Code number and polymer.

Code	Polycarbonates
1	Poly(DTE Carbonate)
2	Poly(DTE-co-4% PEG _{IK} Carbonate)
3	Poly(DTE-co-8% PEG _{IK} Carbonate)
5	Poly(DTE-co-10% DT carbonate)
7	Poly(DTE-co-10% DT-co-4% PEG _{IK} Carbonate)
8	Poly(DTE-co-10% DT-co-8% PEG _{IK} Carbonate)
9	Poly(I ₂ DTE Carbonate)
10	Poly(I ₂ DTE-co-4% PEG _{IK} Carbonate)
11	Poly(I ₂ DTE-co-8% PEG _{IK} Carbonate)
13	Poly(I ₂ DTE-co-10% I2DT _{IK} Carbonate)
14	Poly(I ₂ DTE-co-10% I2DT-co-4% PEG _{IK} Carbonate)
15	Poly(I ₂ DTE-co-10% I2DT-co-8% PEG _{IK} Carbonate)
17	PLGA-resomer 506 (Boehringer Ingelheim)
PLLA	PLLA-resomer L 206
TCP	Tissue Culture Plastic-Control

Saos-2 cells (ATCC HTB-85) were initially cultured in eight 24-well plates on top of polyarylate- and polycarbonate-coated coverslips in 500 μ L of HAM's F-12 medium supplemented with 10% fetal bovine serum, 10 mM Hepes pH 7.5, plus penicillin and streptomycin, and glutamine. When the cultures were confluent, 10 mM β -glycerolphosphate, 10 mM dexamethasone (DEX), and 50 μ g/mL ascorbic acid were added to induce mineralization⁹⁷. The addition was repeated at every medium change until the end of the experiment. All drugs were prepared as sterile working solutions in the growth medium on the day of the experiment. Cultures were grown at 37 °C in a humidified 5% CO₂ atmosphere with routine medium change.

Alizarin red is a dye, which binds selectively to calcium salts and is widely used for calcium mineral histochemistry. Every week the medium of one plate was removed and the culture wells were briefly washed with 500 μ L of phosphate buffered saline (PBS) and then fixed for 10 min in ice-cold 99.8% methanol. Cultures were rinsed again with 500 μ L of PBS and stained for 10 min with 500 μ L of 1% alizarin red-S. Cultures were then rinsed five times with distilled water followed by a 15 min wash with PBS, to remove the stain not associated with calcium mineral deposits. A de-staining procedure was followed using 10% cetylpyridinium chloride in sodium phosphate, pH 7.0 for 15 min in order to measure the optical absorbance. Absorbance measurements were done with an Universal Microplate Reader, Biotek, Inc, with a wavelength of 570 nm.

7.2.3 Results and Conclusions

All Saos-2 cultures on *polyarylate-coated* coverslips formed calcium phosphate mineral with minimal disparity between each of them. As shown in Figure 7.5, all Saos-2 cultures on *polycarbonate-coated* coverslips formed calcium phosphate mineral.

However, low light absorbance was obtained in polycarbonate substrates with 4% and 8% PEG. PEG 8% resulted in poor cell attachment and little spreading. In contrast, no significant variations were obtained on the *polycarbonate* cultures where PEG is also present in 4% and 8% When iodine (I_2) is incorporated it seems to suppress the effect of PEG. It is possible that the iodine may work to suppress the PEG by steric hindrance rather than making the polymer more hydrophobic. The presence of DT strongly suppresses the effects of PEG. These experiments were completed as part of a lab rotation and need to be repeated before firm conclusions can be drawn.

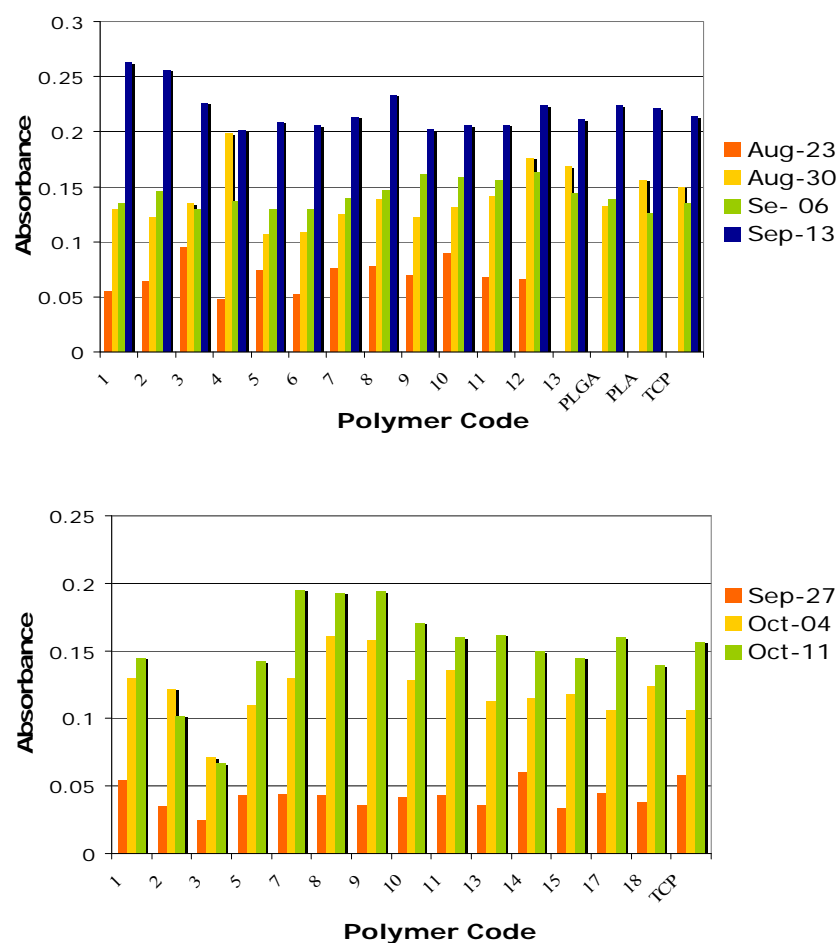


Figure 7.5 Saos-2 mineralization on (top) polyarylate-coated coverslips and (bottom) polycarbonate-coated coverslips.

7.3 Mechanical Characterization of Pharmaceutical Compacts and Single Crystals

7.3.1 Introduction

During the summer of 2006 I had the opportunity to work as a summer intern in the Department of Analytical Research and Development at Bristol-Myers Squibb. During the internship I worked on a project measuring the mechanical properties of pharmaceutical compacts and drug single crystals.

Drug product performance, including dissolution rates, tablet hardness and content uniformity, are affected by the mechanical properties of the active pharmaceutical ingredients (APIs) and excipients. The physical nature of powders is different from solid bodies, in that powders can flow, imparting powders with some rheological properties typical of liquids. On the other hand, powders also show phenomena typical for solids, including permanent deformation (plastic), reversible deformation (elastic), and brittle fracturing of particles. Thus, the behavior of powders during pharmaceutical processing is often very complicated. For instance, during tablet compaction, particle flow, plastic and elastic deformation, and brittle fracture can each occur. The process of compaction involves subjecting the materials to stresses causing them to undergo deformation. The reaction of a material to a deformation stress is dependent on the mechanical properties of that material. Therefore there is a need to accurately measure a material's mechanical properties in order to predict the compaction behavior of a material in a pharmaceutical formulation.

Various methods were employed to characterize the mechanical properties of two well characterized pharmaceutical compounds, sucrose and acetaminophen. Three techniques were evaluated for reproducibility and discrimination of mechanical

properties between the test materials, and also as potential methods for the mechanical characterization of other Bristol-Myers Squibb active pharmaceutical ingredients. The reduced elastic modulus, stiffness and hardness of sucrose and acetaminophen (APAP) single crystals were measured using nanoindentation. Standard compression tests of large single crystals were employed to measure the tensile strength and Young's modulus of the crystals from the stress versus strain curves. In addition the applicability of ellipsoidal yield functions to measure the yield strength of powder compacts, as suggested by Oyane and Shima, was also explored⁹⁸.

7.3.2 Materials and Methods

Acetaminophen (SigmaUltra, $\geq 99.0\%$) and Sucrose (BioChemika Ultra, $\geq 99.5\%$ HPLC) were obtained from Sigma-Aldrich. Both sucrose and acetaminophen crystal are monoclinic. The crystal form of acetaminophen and sucrose ($P2_1$) were determined using powder X-ray diffraction. Various methods were used to grow large sucrose and acetaminophen single crystals, with the goal of preparing crystals large enough to run nanoindentation and simple compression experiments. Some factors considered during the crystal growth optimization included the solubility of the compound in the solvent, the effect of seeding, mechanical agitation, and time. Sucrose single crystals were grown using two different techniques, which were found to produce equivalent crystals that were useful for the experiments reported in this study. The first method employed was the vapor diffusion technique. A saturated solution of sucrose was prepared using distilled water as the solvent. A second solvent was placed in a larger beaker. The second solvent, methanol, was selected based on low sucrose solubility and low boiling

point compared to water. The beaker containing dissolved sucrose in water was placed inside the beaker containing methanol, with the whole systems being sealed with laboratory wrapping film (Parafilm M, Pechiney Plastic Packaging, Chicago IL.). Slow diffusion of methanol into water caused the crystals to nucleate and grow. The solvent diffusion technique, also called the layering technique, was used as well for the sucrose crystallization. In this method, sucrose was dissolved in distilled water. The saturated solution was placed in a test tube. Methanol was then slowly poured into the tube so that discrete-layers were formed. Sucrose crystals grew as the methanol diffused into the aqueous layer. For the acetaminophen crystallization it was found that the most suitable method to produce large crystals was by preparing a supersaturated solution of APAP in distilled water and allowing the water to evaporate. Photomicrographs of the crystals were obtained using a Leica MZ9.5 stereomicroscope coupled to a Zeiss AxioCam digital camera (Figure 7.6).

Simple compression experiments of sucrose and acetaminophen crystals were performed with a single-column compression tester (Zwicki-Line, Zwick-Roell, Ulm, Germany). The instrument's stiffness was measured and subtracted from the compression test results. The instrument was programmed with a pre-load force of 0.1 N and a test speed of 4 mm/min. Maximum loads of 50 N were applied to each of 48 sucrose crystals and 66 acetaminophen crystals. The tensile strengths of the single crystals were calculated by the following equation:

$$\text{crystal tensile strength} = \frac{F_f}{A_0} \quad (7.1)$$

where F_f is the applied force at fracture perpendicular to the sample and A_0 is the original cross-sectional area before any load was applied. The slopes of the linear segment of the stress-strain plots were analyzed to obtain the elastic modulus using Hook's law.

$$\sigma = E \varepsilon \quad (7.2)$$

where E is the Young's modulus and ε is the deformation strain.

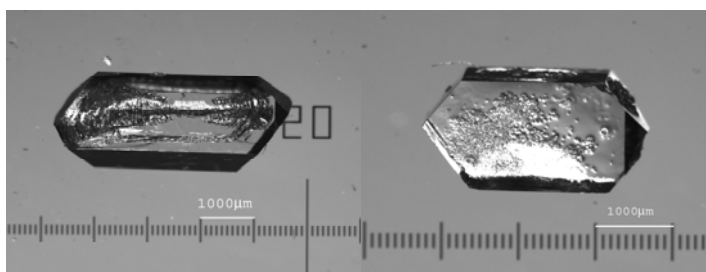


Figure 7.6 Photomicrograph of acetaminophen (left) and sucrose (right) crystal.

Nanoindentation experiments were performed using a Triboindenter (Hysitron, Minneapolis, MN) in load control mode. Acetaminophen and sucrose single crystals were selected for mounting using light microscopy analysis. Selection for use was based on the observed quality of the crystals. Crystal orientation (001) was maintained with respect to the indenter. All samples were tested in a dry state. Fused silica was used to calibrate the indenter. The crystals were indented with a Berkovich diamond indenter using a 10 second loading time, followed by a 2 second hold, and concluding with a 10 seconds unloading time. A maximum load of 1000 μN was applied to the crystals.

To apply the plasticity theory proposed by Shima and Oyane, tablets in the shape of cylinders with 0.25 inch diameter and relative densities (ρ) of 0.46-0.92 were obtained from acetaminophen and sucrose powders by closed-die compaction using the Zwicki-

Line as well. The relative densities (ρ) of the tablets were calculated from the following relationship:

$$\rho = \frac{\rho_t}{\rho_c} = \frac{m_t / V_t}{\rho_c} \quad (7.3)$$

where ρ_t , m_t , and V_t are the tablets density, mass and volume and ρ_c is the compound density (specific gravity). For acetaminophen ρ_c was taken to be 1.29 g/cm³ and for sucrose 1.59 g/cm³. Magnesium stearate was used as a lubricant on the die surfaces to reduce powder sticking to the die walls and punch faces. Throughout the duration of each compaction test, the relative density of the tablets was recorded as a function of machine load. After powder compaction, the tablets were recompressed, unconfined using the Zwicki-Line pre-programmed for 5 N pre-load and 10 mm/min test speed. The experiments were stopped right after tablet failure. The fracture stress corresponding to the different densities were recorded and plotted as well.

The following equations were used to calculate the yield strength theoretically

$$f = a(1 - \rho)^m \quad (a > 0, m < 0) \quad (7.4)$$

$$p = S \rho^n (f^2 + 4/9)^{1/2} \quad (7.5)$$

$$\sigma = S \rho^n / (1 + 1/9 / f^2)^{1/2} \quad (7.6)$$

where a , m , f , n , and S are constants determined experimentally, ρ is the relative density, p is the predicted hydrostatic pressure during confined compression, and σ is the predicted fracture stress during unconfined compression. The initial values for constants a , m , S , and n were set to 1, -1, 1000, and 2 respectively. A Microsoft Excel macro was

used to determine the best values for each constant by curve fitting to the experimental results.

7.3.3 Results and Conclusions

Using simple compression experiments on single crystals a Young's modulus of 36.9 GPa and 12.6 GPa were obtained for sucrose and acetaminophen respectively. Results are shown in Table 7.3. The tensile strength range is presented as well.

Table 7.3 Tensile strength and Young modulus (E) of acetaminophen and sucrose single crystals using simple compression experiments.

	APAP n=8	Sucrose n=19
Tensile Strength (MPa)	0.1-3.4	1.1-8.3
Young's Modulus (GPa)	12.6±1.4	36.9±3.2

During nanoindentation the maximum penetration depth for acetaminophen and sucrose were about 281 nm and 189 nm respectively. The Stiffness, Young modulus and hardness of the samples were evaluated from the load vs displacement curves using the Oliver-Pharr. Results are shown in Table 7.4

Table 7.4 Average values of stiffness, reduced Young's modulus and hardness of 66 acetaminophen and 48 sucrose single crystals obtained by nanoindentation.

Acetaminophen				Sucrose		
	S ($\mu\text{N/nm}$)	Er (GPa)	H (GPa)	S ($\mu\text{N/nm}$)	Er (GPa)	H (GPa)
Measured	15.52 \pm 0.76	11.5 \pm 0.7	0.64 \pm 0.02	31.6 \pm 0.4	33 \pm 1	1.4 \pm 0.1
Literature	22.6 \pm 5.4 ^{99,100}	8.4 ^{100,101}	0.421 ^{100,101}	82 ^{99,100}	32.3 _{100,101}	0.645 ^{100,101}

Using the plasticity theory for porous sintered metals, we were able to predict the compaction pressure (p) and fracture stress (f) for the different tablet densities produced for this study from the constants a , m , and S which were obtained experimentally by the compression of acetaminophen and sucrose powders and compacts. See table Table 7.5.

Table 7.5 Applied plasticity theory for sucrose and acetaminophen using a 1.25 inches die for closed-die compression.

Constants	Acetaminophen	Sucrose
a	2.064	2.248
m	0.702	1.366
S (N/mm ²)	26.425	37.083
n	9.039	7.224

Appendix A Berkovich Indenter

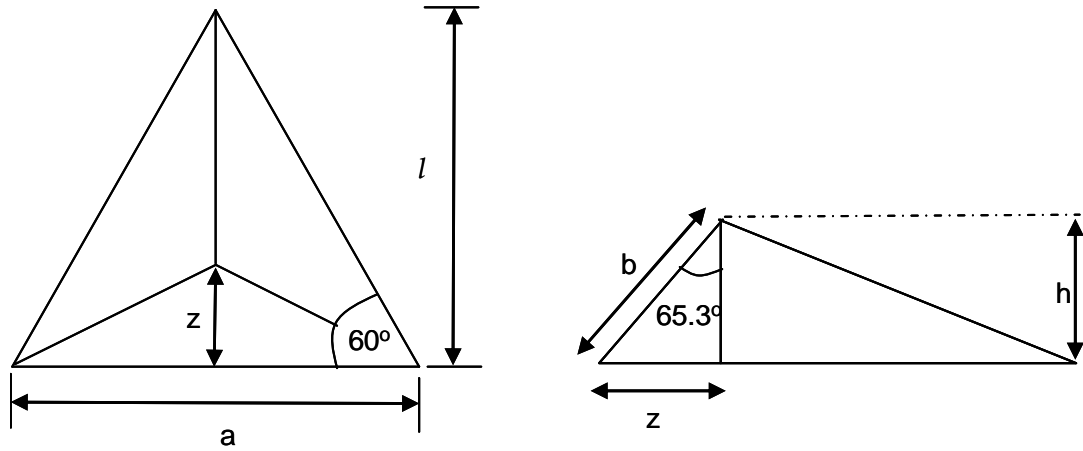


Figure A.1 Berkovich tip Geometry.

Projected Area

$$\tan 60 = \frac{l}{a/2}$$

$$l = \frac{\sqrt{3}}{2} a$$

$$\begin{aligned} A_{proj} &= \frac{al}{2} \\ &= \frac{\sqrt{3}}{4} a^2 = 0.433a^2 \end{aligned}$$

$$\cos 65.27 = \frac{h}{b}$$

$$h = \frac{a \cos 65.3}{2\sqrt{3} \sin 65.3}$$

$$= \frac{a}{2\sqrt{3} \tan 65.3}$$

$$a = 2\sqrt{3}h \tan 65.3$$

$$A_{proj} = 3\sqrt{3}h \tan^2 65.3$$

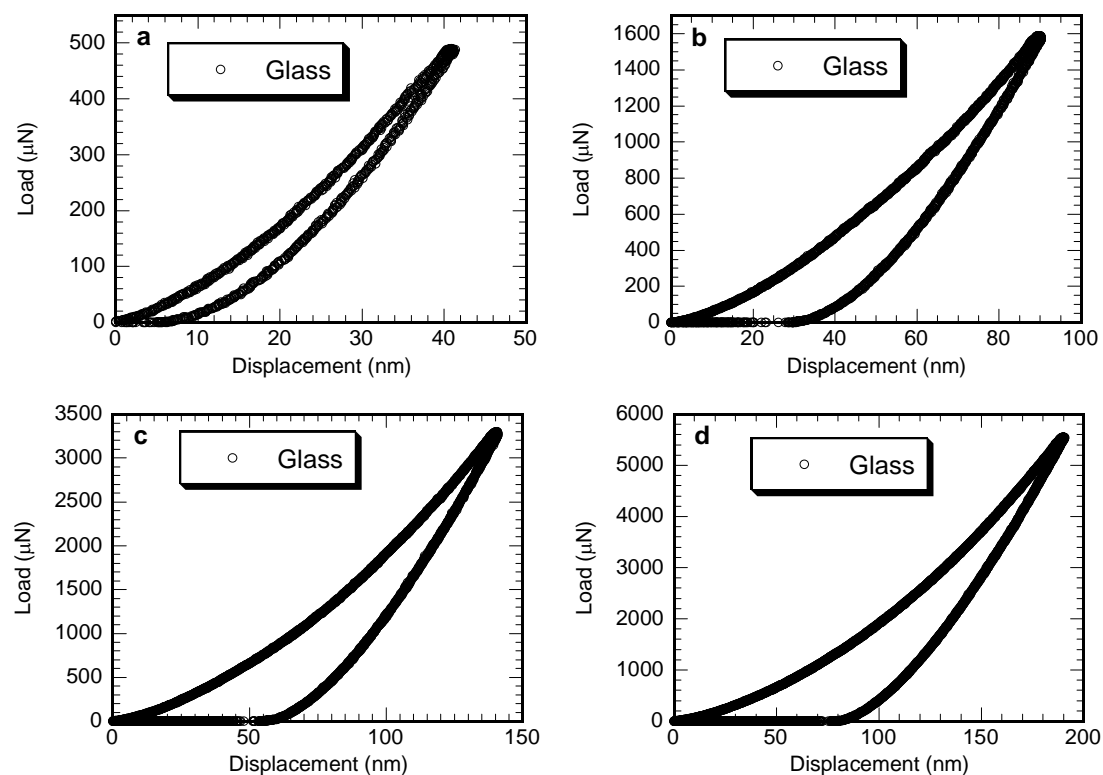


Figure A.2 Characteristic load-displacement curves for glass (coverslip) substrate. Nanoindentation experiments performed using displacement control mode with maximum displacements of (a) 40 nm, (b) 90 nm, (c) 140 nm, and (d) 190 nm.

Appendix B Contact Angle

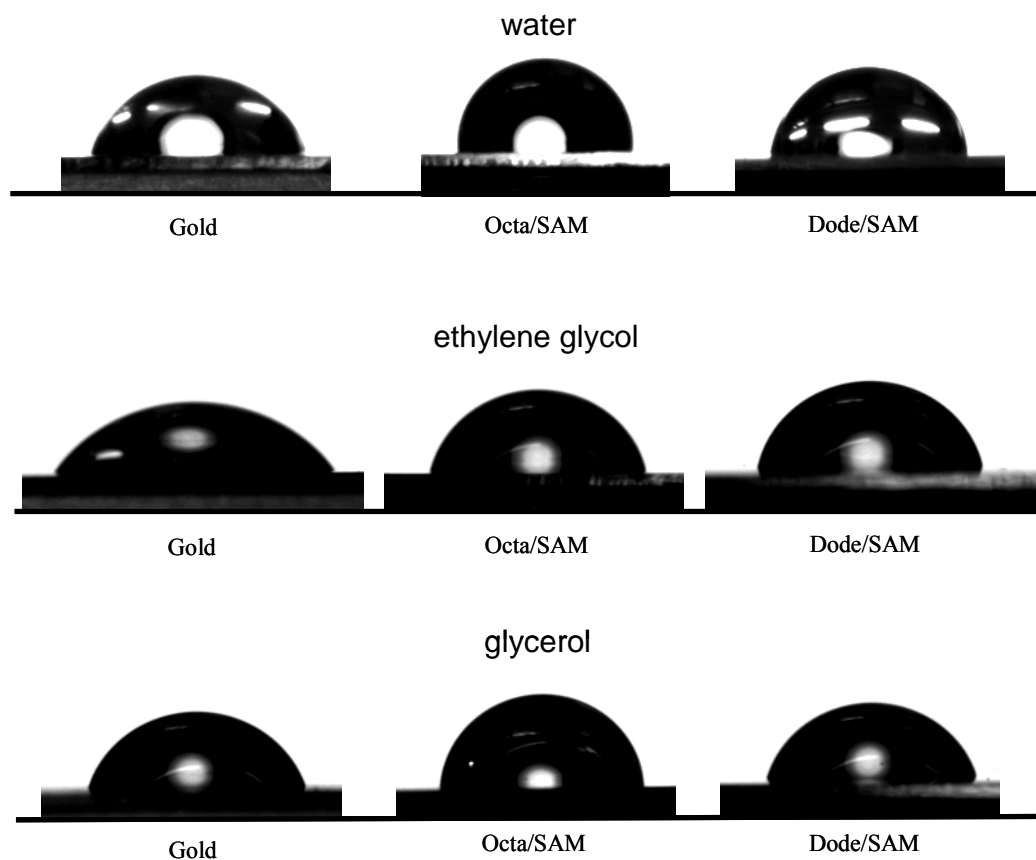


Figure B.1 Images of contact angles on gold, octanethiol SAM and dodecanethiol SAM using water, ethylene glycol and glycerol as measuring liquids.

Alkanethiol Self-Assembled Monolayers Thicknesses

Table B.1 Alkanethiol thicknesses measured by ellipsometry assuming refractive index of 1.50.
*Value measured by ellipsometry. [§]Results reported by Del Rio, 2009.

$[\text{CH}_3(\text{CH}_2)_{n-1} \text{SH}]$	Thickness (nm)
n=5	0.38 [§]
n=8	0.74 [§]
n=10	0.809 [*]
n=12	1.25 [§]
n=18	2.03 [§]

Appendix C

Oliver and Pharr Hardness and Reduced Elastic Modulus

Table C.1 Averaged Oliver and Pharr Hardness (H) for eight carbons alkanethiol SAM and respective Au(111) film on glass.

Max tip displacement (nm)	PHY4 Au H (GPa)	Standard Error	PHY4 Octa/SAM H (GPa)	Standard Error	% difference
40	1.41	0.02	1.40	0.02	0.75
90	3.11	0.007	3.12	0.01	-0.33
140	3.80	0.008	3.75	0.01	1.35
190	4.23	0.01	4.18	0.005	1.21

Table C.2 Averaged Oliver and Pharr Hardness (H) for ten carbons alkanethiol SAM and respective Au(111) film on glass.

Max tip displacement (nm)	L4 Au H (GPa)	Standard Error	L4 Deca/SAM H (GPa)	Standard Error	% difference
40	1.93	0.09	1.49	0.03	22.9
90	3.63	0.02	3.55	0.02	2.3
140	4.33	0.02	4.18	0.02	3.5
190	4.70	0.01	4.52	0.02	3.8

Table C.3 Averaged Oliver and Pharr Hardness (H) for twelve carbons alkanethiol SAM and respective Au(111) film on glass.

Max tip displacement (nm)	PHY3 Au H (GPa)	Standard Error	PHY3 Dode/SAM H (GPa)	Standard Error	% difference
40	1.43	0.002	1.13	0.016	21.0
90	3.17	0.009	2.94	0.02	7.3
140	3.87	0.01	3.63	0.01	6.3
190	4.28	0.01	4.09	0.02	4.4

Table C.4 Averaged Oliver and Pharr reduced elastic moduli (Er) for eight carbons alkanethiol SAM and respective Au(111) film on glass.

Max tip displacement (nm)	PHY4 Au Er (GPa)	Standard Error	PHY4 Octa/SAM Er (GPa)	Standard Error	% difference
40	70.6	0.9	70.6	1.2	-0.11
90	58.7	0.3	60.4	0.5	-2.93
140	62.1	0.3	60.1	0.4	3.27
190	62.9	0.3	60.1	0.2	4.47

Table C.5 Averaged Oliver and Pharr reduced elastic moduli (Er) for ten carbons alkanethiol SAM and respective Au(111) film on glass.

Max tip displacement (nm)	L4 Au Er (GPa)	Standard Error	L4 Deca/SAM Er (GPa)	Standard Error	% difference
40	62.7	1.7	55.8	0.6	11.08
90	59.1	0.4	55.1	0.3	6.75
140	62.5	0.2	57.9	0.1	7.32
190	63.8	0.2	59.2	0.2	7.27

Table C.6 Averaged Oliver and Pharr reduced elastic moduli (Er) for twelve carbons alkanethiol SAM and respective Au(111) film on glass.

Max tip displacement (nm)	PHY3 Au Er (GPa)	Standard Error	PHY3 Dode/SAM Er (GPa)	Standard Error	% difference
40	70	1.19	64.2	0.91	8.20
90	59.5	0.52	56.1	0.22	5.70
140	61.4	0.27	56.3	0.26	8.24
190	62.6	0.12	57.1	0.08	8.66

Appendix D

Work of Indentation

Table D.1 Total, plastic and elastic works of indentation for Au(111) and Octa/SAM, Deca/SAM and Dode/SAM obtained from numerical integration of the nanoindentation load-displacement curves. Values for work are in $\mu\text{N}/\text{nm}$.

Max. tip displacement (nm)		PHY4			L4			PHY3		
		Au	Octa	%diff	Au	Deca	%diff	Au	Dode	% diff
		Average	Average		Average	Average		Average	Average	
40	Wp	10914	10182	7	11112	8838	20	10938	9286	15
	We	1484	1284	13	2226	1889	15	1407	1137	19
	Wtot	12399	11466	8	13338	10727	20	12345	10423	15
		PHY4			L4			PHY3		
		Au	Octa	%diff	Au	Deca	%diff	Au	Dode	% diff
		Average	Average		Average	Average		Average	Average	
90	Wp	59567	57410	4	65709	59164	10	59510	54599	8
	We	30977	29700	4	32141	35718	-11	31014	29562	5
	Wtot	90544	87109	4	97850	94882	3	90524	84162	7
140		PHY4			L4			PHY3		
		Au	Octa	%diff	Au	Deca	%diff	Au	Dode	% diff
		Average	Average		Average	Average		Average	Average	
	Wp	169568	144980	15	184392	161727	12	175166	157553	10
	We	122907	117356	5	120700	131640	-9	116028	110383	5
	Wtot	292475	262336	10	305092	293368	4	291195	267937	8
190		PHY4			L4			PHY3		
		Au	Octa	%diff	Au	Deca	%diff	Au	Dode	% diff
		Average	Average		Average	Average		Average	Average	
	Wp	378326	342725	9	424692	340492	20	369571	341686	8
	We	300694	272621	9	292526	314574	-8	283823	266970	6
	Wtot	679019	615346	9	717218	655066	9	653394	608656	7

Appendix E

Atomic Force Microscopy of Residual Nanoindentation Impressions

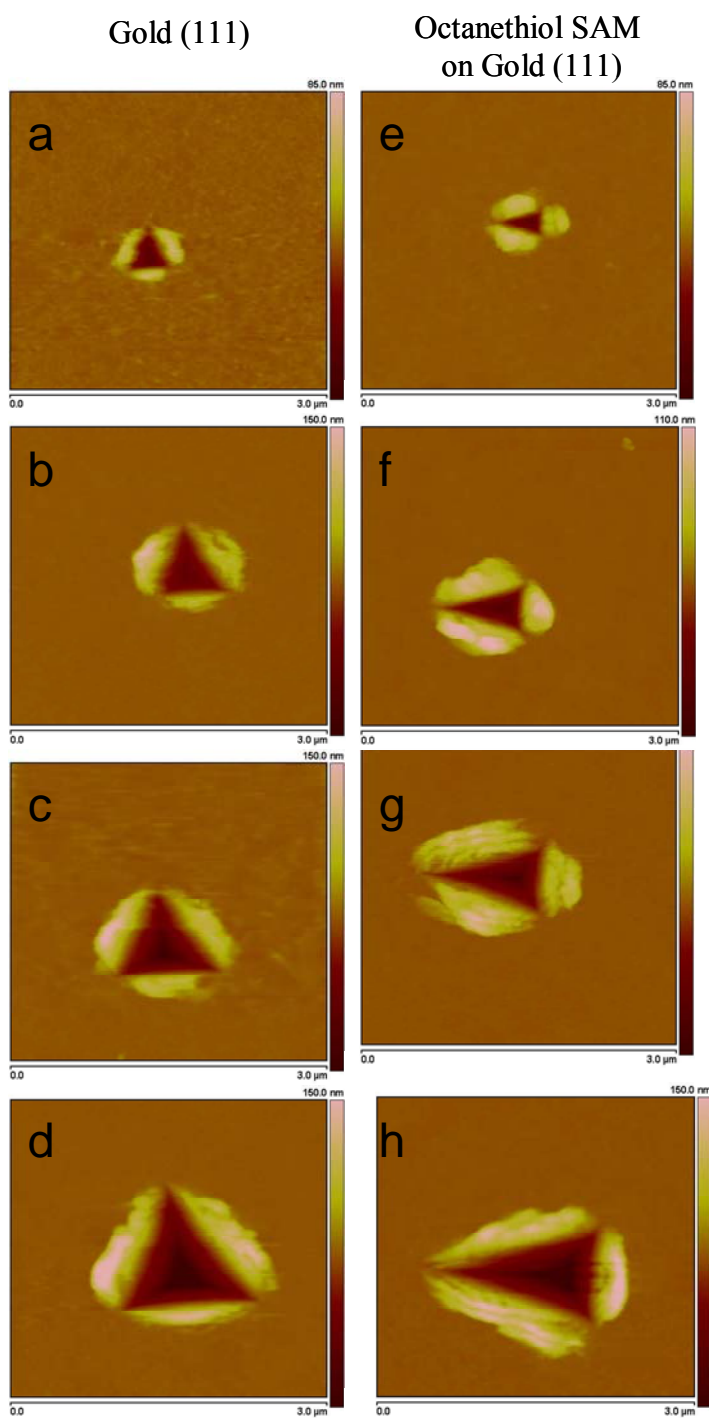


Figure E.1 Representative AFM height images of residual nanoindentation impressions on Au (a,b,c, and d) and octanethiol SAM grown on the same Au (e, f, g and h). Maximum indenter displacements of 40 nm (a and e), 90 nm (b and f), 140 nm (c and g) and 190 nm (d and h).

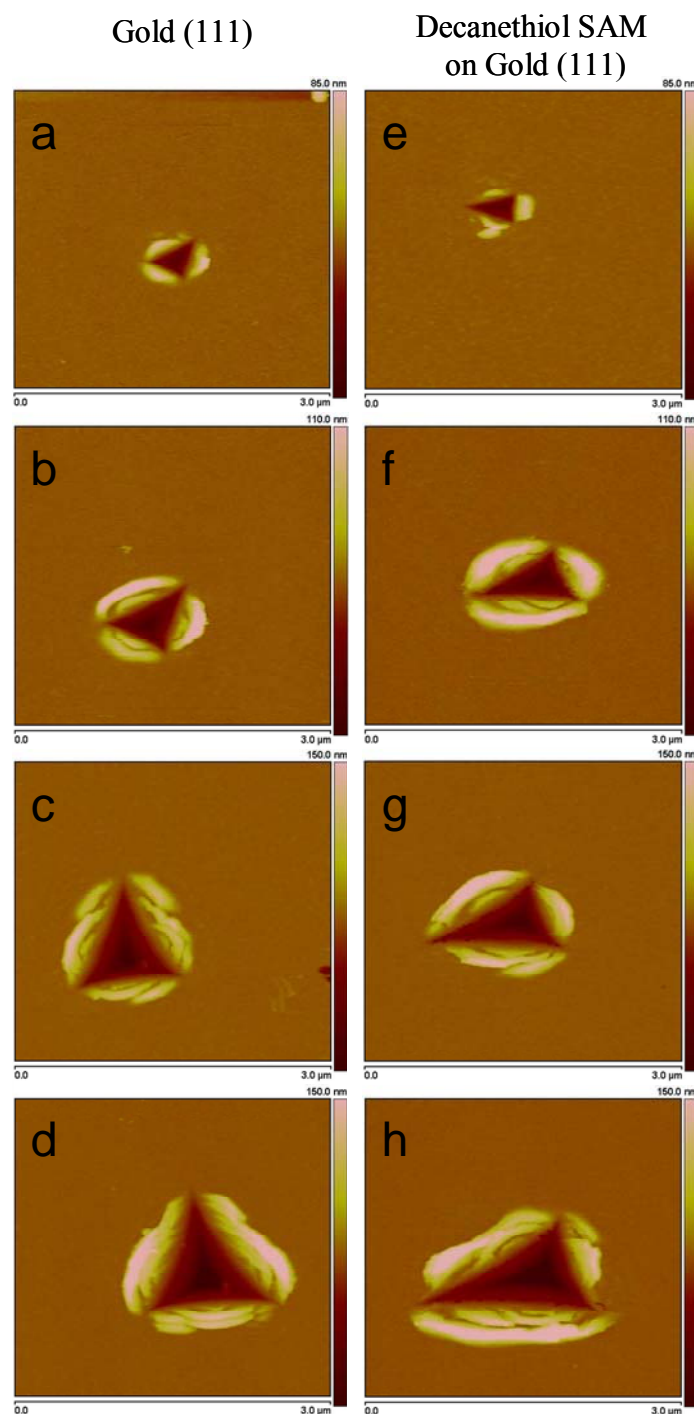


Figure E.2 Representative AFM height images of residual nanoindentation impressions on Au (a,b,c, and d) and decanethiol SAM grown on the same Au (e, f , g and h). Maximum indenter displacements of 40 nm (a and e), 90 nm (b and f), 140 nm (c and g) and 190 nm (d and h).

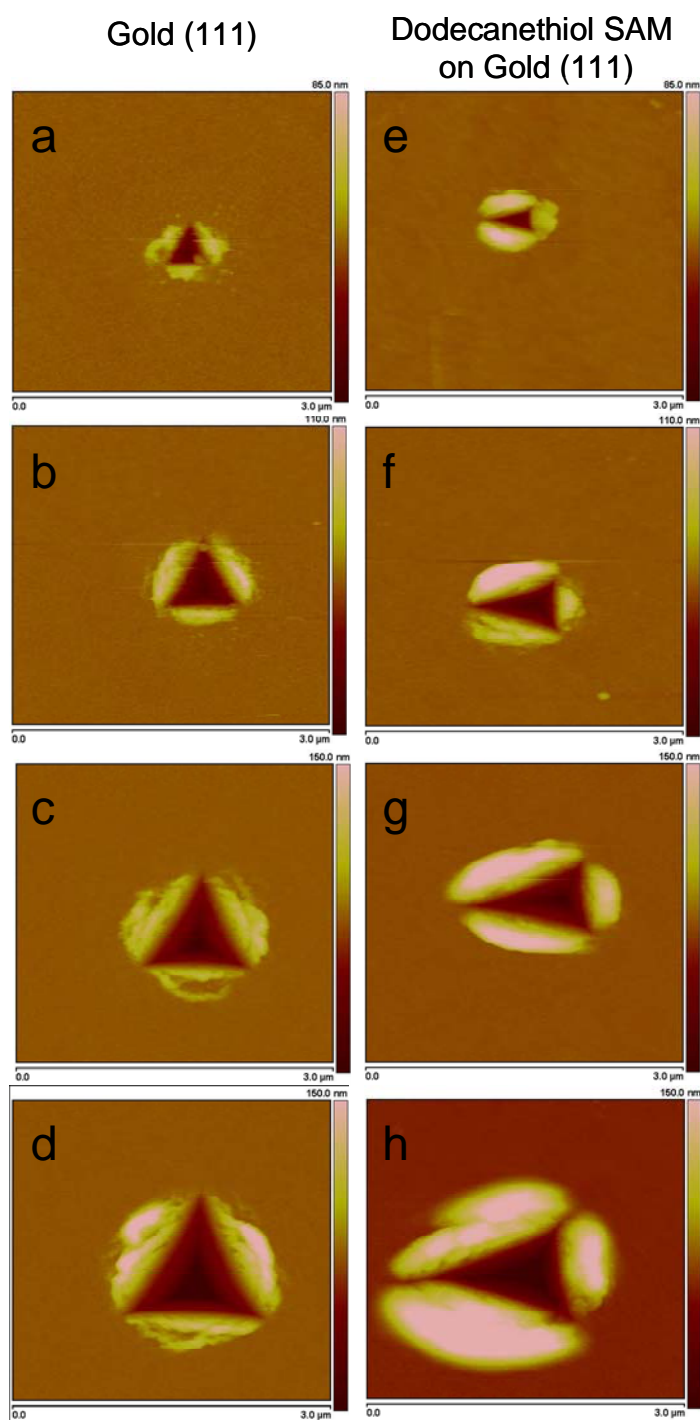


Figure E.3 Representative AFM images of residual nanoindentation impressions on Au (a,b,c,d) and dodecanethiol SAM grown on the same Au (e, f, g and h). Maximum indenter displacements of 40 nm (a and e), 90 nm (b and f), 140 nm (c and g) and 190 nm (d and h).

Appendix F

Surface Area Calculations: Matlab Code

The first step in the code consists of importing the ASCII text file of the nanoindentation residual impression AFM image into Matlab software. The resolution of the recorded contact mode AFM images were set to 512x512, meaning 512 pixels in 512 lines. Thus, the ASCII file contains 262,144 numbers that correspond to the z-positions in the 512 x 512 matrix (heights in the xy plane).

The second step consists in converting the loaded file into a 512x512 matrix as shown in step 2 in Figure F.1. In step 3 a circle is created and positioned in such a way that the indent is inside the circle. All height data outside the indent ($\text{Data} > \text{Radius}$) is zeroed. Step three was introduced into the code to eliminate dust particles sometime recorded during AFM image recordings. For the 40 nm, 90 nm, 140 nm and 190 nm maximum displacement indents on gold and SAM/gold radiuses of 75, 105, 140 and 178 pixels were consistently used respectively.

In the fourth step, the surface area is calculated by numerical double integration of the two variables xy following the mathematical analysis discussed in 5.5.1. Note that D_x and D_y , the lengths of the pixels in x and y, are both equal to 5.859375 given that all AFM images are 3 μm x 3 μm .

```

%load ASCII file%
dataAFM=load('phy4_octa_200_005.txt');

%matrix 512*512%
afmimg=zeros(512,512);
i=1;
for m=1:512
    for n=1:512
        afmimg(m,n)=dataAFM(i);
        i=i+1;
    end
end

figure;imagesc(afmimg); colorbar
pause

%circle around indent
if (1==1)
    xr=200;
    yr=235;
    r=178;
    for j=1:512
        for i=1:512
            Radius=sqrt((i-xr)^2+(j-yr)^2);
            if (Radius>r)
                afmimg(i,j)=0.0; %0.0.....to verify the circle put 10
            end
        end
    end
    figure;imagesc(afmimg); colorbar
    pause
end

area(1:3)=0.0;
dfx=zeros(512,512);
dfy=zeros(512,512);

dx=5.859375;
dy=5.859375;

dfx(2:511,1:512)=(afmimg(3:512,1:512)-afmimg(1:510,1:512))/(2*dx);
dfy(1:512,2:511)=(afmimg(1:512,3:512)-afmimg(1:512,1:510))/(2*dy);
dfx(1,1)=(afmimg(2,1)-afmimg(1,1))/dx;
dfy(1,1)=(afmimg(1,2)-afmimg(1,1))/dy;
dfx(1,512)=(afmimg(2,512)-afmimg(1,512))/dx;
dfy(1,512)=(afmimg(1,512)-afmimg(1,511))/dy;
dfx(512,1)=(afmimg(512,1)-afmimg(511,1))/dx;
dfy(512,1)=(afmimg(512,2)-afmimg(512,1))/dy;
dfx(512,512)=(afmimg(512,512)-afmimg(511,512))/dx;
dfy(512,512)=(afmimg(512,512)-afmimg(512,511))/dy;

small_area=sqrt(dfx.*dfx+dfy.*dfy+1);

```

Step 1**Step 2****Step 3****Step 4**

Figure F.1 Matlab code for surface area calculation using double integral method.

To calculate the surface area of only the pile-up around the indent a critical number was introduced, as shown in step fifth in Figure F.2. This critical number serves

as a baseline for the code to differentiate between heights that correspond to pile-up from heights from the surface roughness or indent contact (negative surface). In steps sixth, seventh and eighth the total surface area and pile-up surface area is calculated using the height values inside the previously defined circle in step 3. For the total surface area all heights inside the circle are considered whereas for the pile-up surface area only heights greater than the critical number are considered.

<pre>%Critical Number to determine pileup critic=2.5 figure;imagesc((afmimg<-critic)+(afmimg>critic));colorbar pause</pre>	Step 5
<pre>for test=1:2 %Total Area Calculation if (test==1) area(test)=dx*dy*sum(sum(small_area)); end</pre>	Step 6
<pre>%Pileup Area, Z=f(x,y) > critical number if (test==2) figure;imagesc(afmimg>critic);colorbar pause temp=small_area.*(afmimg>critic); area(test)=dx*dy*sum(sum(temp)); end</pre>	Step 7
<pre>end total_area=area(1) pile_up=area(2)</pre>	Step 8

Figure F.2 Partial scene from Matlab code for surface area and volume calculations using double integral method.

Appendix G

Change in Surface Area

Table G.1 Average delta surface area for Octa/SAM and gold substrate. Negative % difference correspond to increase in Δ Surface Area.

Max tip displacement (nm)	PHY4 Au Δ Surface Area (m ²)	Standard Error	PHY4 Octa/SAM Δ Surface Area (m ²)	Standard Error	% difference
40	1.63E-14	1E-15	2.19E-14	3.08E-15	-34
90	5.94E-14	8.13E-15	7.39E-14	7.28E-15	-24
140	9.31E-14	7.66E-15	1.13E-13	1.08E-14	-22
190	1.41E-13	9.13E-15	2.40E-13	2.59E-14	-71

Table G.2 Average delta surface area for Deca/SAM and gold substrate. Negative % difference correspond to increase in Δ Surface Area.

Max tip displacement (nm)	L4 Au Δ Surface Area (m ²)	Standard Error	L4 Deca/SAM Δ Surface Area (m ²)	Standard Error	% difference
40	2.52E-14	1.95E-15	1.99E-14	2.00E-15	21
90	1.08E-13	1.15E-14	1.27E-13	1.31E-14	-17
140	1.85E-13	6.33E-15	2.33E-13	1.26E-14	-26
190	2.84E-13	6.17E-15	3.89E-13	3.20E-14	-37

Table G.3 Average delta surface area for Dode/SAM and gold substrate. Negative % difference correspond to increase in Δ Surface Area.

Max tip displacement (nm)	PHY3 Au Δ Surface Area (m ²)	Standard Error	PHY3 Octa/SAM Δ Surface Area (m ²)	Standard Error	% difference
40	2.47E-14	1.80E-15	2.13E-14	2.57E-15	14
90	7.06E-14	2.35E-15	9.30E-14	2.42E-14	-32
140	1.12E-13	6.44E-15	1.73E-13	7.05E-15	-54
190	2.07E-13	1.26E-14	3.77E-13	2.82E-14	-82

Appendix H

Maximum Nanoindentation Pile-up Heights

Table H.1 Average maximum pile-up heights for Octa/SAM and gold substrate.

Max tip displacement (nm)	PHY4 Au Max. pileup height (nm)	Standard Error	PHY4 Octa/SAM Max. pileup height (nm)	Standard Error	% difference
40	35.43	2.25	32.84	2.33	7.33
90	72.01	6.23	55.14	0.91	23.42
140	74.39	1.99	77.52	8.42	-4.21
190	91.66	5.25	103.71	7.03	-13.15

Table H.2 Average maximum pile-up heights for Deca/SAM and gold substrate.

Max tip displacement (nm)	L4 Au Max. pileup height (nm)	Standard Error	L4 Deca/SAM Max. pileup height (nm)	Standard Error	% difference
40	41.23	0.04	40.28	5.28	2.29
90	75.02	6.07	88.38	10.93	-17.81
140	86.99	3.16	106.67	4.52	-22.62
190	99.90	4.10	122.83	8.83	-22.95

Table H.3 Average maximum pile-up heights for Dode/SAM and gold substrate.

Max tip displacement (nm)	PHY3 Au Max. pileup height (nm)	Standard Error	PHY3 Dode/SAM Max. pileup height (nm)	Standard Error	% difference
40	44.29	4.89	40.96	4.66	7.52
90	74.35	1.11	82.09	10.49	-10.41
140	76.66	6.68	112.69	1.68	-46.99
190	106.00	8.71	126.93	8.03	-19.74

Appendix I

Projected Contact Area from AFM

Table I.1 Tabulated Results from horizontal sectioning of AFM images from residual nanoindentation impressions on Gold (111) (Sample PH4). Total contact areas calculated from trigonometry approach.

Sample Max disp/indent	Sample:PHY4_Au_40						Areas Semi- ellipse
Au_40_004	2A1	0.393	A1	0.1965	B1	0.059	0.01821
	2A2	0.413	A2	0.2065	B2	0.163	0.05287
	2A3	0.394	A3	0.197	B3	0.053	0.01640
	S	0.6				Total Area ellipses (μm^2)	0.08748
	Area triangle (μm^2)	0.06917		Total Area (nm^2)	156653.52		
Au_40_005	2A1	0.475	A1	0.2375	B1	0.126	0.04700
	2A2	0.478	A2	0.239	B2	0.095	0.03566
	2A3	0.366	A3	0.183	B3	0.076	0.02184
	S	0.6595				Total Area ellipses (μm^2)	0.10451
	Area triangle (μm^2)	0.08051		Total Area (nm^2)	185027.3		
Au_40_006	2A1	0.433	A1	0.2165	B1	0.086	0.02924
	2A2	0.411	A2	0.2055	B2	0.071	0.02291
	2A3	0.4	A3	0.2	B3	0.065	0.02042
	S	0.622				Total Area ellipses (μm^2)	0.07258
	Area triangle (μm^2)	0.074207		Total Area (nm^2)	146792.53		
	Sample:PHY4_Au_90						
Au_90_006	2A1	0.748	A1	0.374	B1	0.262	0.15391
	2A2	0.814	A2	0.407	B2	0.127	0.08119
	2A3	0.677	A3	0.3385	B3	0.089	0.04732
	S	1.1195				Total Area ellipses (μm^2)	0.28243
	Area triangle (μm^2)	0.237112		Total Area (nm^2)	519546.77		
Au_90_007	2A1	0.745	A1	0.3725	B1	0.26	0.15213
	2A2	0.775	A2	0.3875	B2	0.178	0.10834
	2A3	0.647	A3	0.3235	B3	0.1	0.05081
	S	1.0835				Total Area ellipses (μm^2)	0.31129
	Area triangle (μm^2)	0.222236		Total Area (nm^2)	533528.1		

Au_90_008	2A1	0.709	A1	0.3545	B1	0.271	0.15090
	2A2	0.77	A2	0.385	B2	0.145	0.08769
	2A3	0.611	A3	0.3055	B3	0.102	0.04894
	S	1.045				Total Area ellipses (μm^2)	0.28754
	Area triangle (μm^2)	0.20471		Total Area (nm^2)	492252.88		
	Sample:PHY4_Au_140						
Au_140_000	2A1	1.024	A1	0.512	B1	0.207	0.16647
	2A2	0.965	A2	0.4825	B2	0.158	0.11975
	2A3	0.943	A3	0.4715	B3	0.083	0.06147
	S	1.466				Total Area ellipses (μm^2)	0.34770
	Area triangle (μm^2)	0.412048		Total Area (nm^2)	759749.28		
Au_140_001b	2A1	1.187	A1	0.5935	B1	0.176	0.16407
	2A2	1.14	A2	0.57	B2	0.174	0.15579
	2A3	0.978	A3	0.489	B3	0.195	0.14978
	S	1.6525				Total Area ellipses (μm^2)	0.46965
	Area triangle (μm^2)	0.515666		Total Area (nm^2)	985319.95		
Au_140_003	2A1	0.983	A1	0.4915	B1	0.266	0.20536
	2A2	1.002	A2	0.501	B2	0.143	0.11253
	2A3	0.974	A3	0.487	B3	0.083	0.063493
	S	1.4795				Total Area ellipses (μm^2)	0.38139
	Area triangle (μm^2)	0.42108		Total Area (nm^2)	802473.83		
Au_140_003b	2A1	0.912	A1	0.456	B1	0.265	0.18981
	2A2	0.968	A2	0.484	B2	0.126	0.09579
	2A3	0.97	A3	0.485	B3	0.088	0.06704
	S	1.425				Total Area ellipses (μm^2)	0.35265
	Area triangle (μm^2)	0.389879		Total Area (nm^2)	742529.12		
Au_140_004	2A1	1.07	A1	0.535	B1	0.195	0.16387
	2A2	1.091	A2	0.5455	B2	0.227	0.19450
	2A3	0.925	A3	0.4625	B3	0.117	0.085
	S	1.543				Total Area ellipses (μm^2)	0.44338
	Area triangle (μm^2)	0.45152		Total Area (nm^2)	894902.39		
	Sample:PHY4_Au_190						
Au_190_004	2A1	1.36	A1	0.68	B1	0.266	0.28412
	2A2	1.445	A2	0.7225	B2	0.222	0.25194
	2A3	1.287	A3	0.6435	B3	0.137	0.13848
	S	2.046				Total Area	0.67455

						ellipses (μm^2)	
	Area triangle (μm^2)	0.800153		Total Area (nm^2)	1474707.1		
Au_190_005	2A1	1.312	A1	0.656	B1	0.213	0.21948
	2A2	1.451	A2	0.7255	B2	0.185	0.21082
	2A3	1.29	A3	0.645	B3	0.124	0.12563
	S	2.0265				Total Area ellipses (μm^2)	0.55594
	Area triangle (μm^2)	0.7834		Total Area (nm^2)	1339344.7		
Au_190_006	2A1	1.275	A1	0.6375	B1	0.255	0.25535
	2A2	1.375	A2	0.6875	B2	0.174	0.18790
	2A3	1.266	A3	0.633	B3	0.123	0.12230
	S	1.958				Area ellipses	0.56556
	Area triangle (μm^2)	0.734521		Total Area (nm^2)	1300080.4		
Au_190_007	2A1	1.574	A1	0.787	B1	0.273	0.33748
	2A2	1.49	A2	0.745	B2	0.213	0.24926
	2A3	1.303	A3	0.6515	B3	0.2	0.20467
	S	2.1835				Total Area ellipses (μm^2)	0.79142
	Area triangle (μm^2)	0.90147		Total Area (nm^2)	1692893.9		

Table I.2 Tabulated Results from horizontal sectioning of AFM images from residual nanoindentation impressions on octanethiol SAM on Gold (111) (Sample PHY4_octanethiol). Total contact areas calculated from trigonometry approach.

Sample Max disp/indent	Sample:PHY4_Octa_40						Areas Semi- ellipse
Octa_40_006	2A1	0.478	A1	0.239	B1	0.052	0.01952
	2A2	0.259	A2	0.1295	B2	0.082	0.01668
	2A3	0.467	A3	0.2335	B3	0.093	0.03411
	S	0.602				Total Area ellipses (μm^2)	0.07031
	Area triangle (μm^2)	0.058793		Total Area (nm^2)	129105.42		
Octa_40_008b	2A1	0.408	A1	0.204	B1	0.071	0.02275
	2A2	0.282	A2	0.141	B2	0.194	0.04296
	2A3	0.413	A3	0.2065	B3	0.09	0.02919
	S	0.5515				Total Area ellipses (μm^2)	0.09491
	Area triangle (μm^2)	0.05435		Total Area (nm^2)	149262.66		
Octa_40_009	2A1	0.378	A1	0.189	B1	0.106	0.03146
	2A2	0.247	A2	0.1235	B2	0.077	0.01493
	2A3	0.364	A3	0.182	B3	0.103	0.02944
	S	0.4945				Total Area ellipses (μm^2)	0.07585
	Area triangle (μm^2)	0.043136		Total Area (nm^2)	118988.88		
	Sample:PHY4_Octa_90						
Octa_90_006	2A1	0.835	A1	0.4175	B1	0.203	0.13312
	2A2	0.452	A2	0.226	B2	0.141	0.05005
	2A3	0.792	A3	0.396	B3	0.188	0.11694
	S	1.0395				Total Area ellipses (μm^2)	0.30012
	Area triangle (μm^2)	0.175813		Total Area (nm^2)	475939.34		
Octa_90_007	2A1	0.827	A1	0.4135	B1	0.142	0.09223
	2A2	0.588	A2	0.294	B2	0.159	0.07342
	2A3	0.775	A3	0.3875	B3	0.163	0.09921
	S	1.095				Total Area ellipses (μm^2)	0.26487
	Area triangle (μm^2)	0.218199		Total Area (nm^2)	483075.65		
Octa_90_008	2A1	0.74	A1	0.37	B1	0.291	0.16912
	2A2	0.411	A2	0.2055	B2	0.2	0.06456
	2A3	0.796	A3	0.398	B3	0.131	0.08189
	S	0.9735				Total Area ellipses (μm^2)	0.31558
	Area triangle	0.150651		Total Area	466236.49		

	(μm^2)			(nm^2)			
	Sample:PHY4_Octa_140						
Octa_140_005	2A1	1.253	A1	0.6265	B1	0.137	0.13482
	2A2	0.693	A2	0.3465	B2	0.112	0.06095
	2A3	1.267	A3	0.6335	B3	0.244	0.24280
	S	1.6065				Total Area ellipses (μm^2)	0.43858
	Area triangle (μm^2)	0.419671		Total Area (nm^2)	858257.24		
Octa_140_006	2A1	1.204	A1	0.602	B1	0.196	0.18534
	2A2	0.736	A2	0.368	B2	0.284	0.16416
	2A3	1.209	A3	0.6045	B3	0.258	0.24498
	S	1.5745				Total Area ellipses (μm^2)	0.59449
	Area triangle (μm^2)	0.422825		Total Area (nm^2)	1017316.4		
Octa_140_007	2A1	1.301	A1	0.6505	B1	0.188	0.19209
	2A2	0.737	A2	0.3685	B2	0.112	0.06483
	2A3	1.279	A3	0.6395	B3	0.279	0.28026
	S	1.6585				Total Area ellipses (μm^2)	0.53719
	Area triangle (μm^2)	0.455354		Total Area (nm^2)	992545.31		
Octa_140_008	2A1	1.232	A1	0.616	B1	0.13	0.12578
	2A2	0.689	A2	0.3445	B2	0.182	0.09848
	2A3	1.149	A3	0.5745	B3	0.188	0.16965
	S	1.535				Total Area ellipses (μm^2)	0.39393
	Area triangle (μm^2)	0.389721		Total Area (nm^2)	783653.63		
	Sample:PHY4_Octa_190						
Octa_190_005	2A1	1.626	A1	0.813	B1	0.239	0.30521
	2A2	0.953	A2	0.4765	B2	0.259	0.19385
	2A3	1.505	A3	0.7525	B3	0.29	0.34278
	S	2.042				Total Area ellipses (μm^2)	0.84186
	Area triangle (μm^2)	0.704816		Total Area (nm^2)	1546677		
Octa_190_006	2A1	1.597	A1	0.7985	B1	0.178	0.22326
	2A2	0.945	A2	0.4725	B2	0.253	0.18777
	2A3	1.563	A3	0.7815	B3	0.242	0.29707
	S	2.0525				Total Area ellipses (μm^2)	0.70811
	Area triangle (μm^2)	0.711925		Total Area (nm^2)	1420037.2		
Octa_190_007	2A1	1.64	A1	0.82	B1	0.291	0.37482
	2A2	0.999	A2	0.4995	B2	0.165	0.12946
	2A3	1.514	A3	0.757	B3	0.302	0.35910

	S	2.0765				Total Area ellipses (μm^2)	0.86339
	Area triangle (μm^2)	0.741187		Total Area (nm^2)	1604577.9		
Octa_190_008	2A1	1.63	A1	0.815	B1	0.213	0.27268
	2A2	1.057	A2	0.5285	B2	0.258	0.21418
	2A3	1.527	A3	0.7635	B3	0.313	0.37538
	S	2.107				Total Area ellipses (μm^2)	0.86224
	Area triangle (μm^2)	0.782348		Total Area (nm^2)	1644595.2		

Table I.3 Tabulated Results from horizontal sectioning of AFM images from residual nanoindentation impressions on Gold (111) (Sample L4). Total contact area calculated from trigonometry approach.

Sample Max disp/indent	Sample:L4_Au_40						Areas Semi- ellipse
Au_40_001	2A1	0.495	A1	0.2475	B1	0.109	0.042376
	2A2	0.404	A2	0.202	B2	0.135	0.042836
	2A3	0.36	A3	0.18	B3	0.062	0.01753
	S	0.6295				Total Area ellipses (μm^2)	0.102742
	Area triangle (μm^2)	0.071732		Total Area (nm^2)	174473.65		
Au_40_006	2A1	0.48	A1	0.24	B1	0.086	0.032421
	2A2	0.437	A2	0.2185	B2	0.119	0.040843
	2A3	0.399	A3	0.1995	B3	0.077	0.02413
	S	0.658				Total Area ellipses (μm^2)	0.097394
	Area triangle (μm^2)	0.081878		Total Area (nm^2)	179272.41		
	Sample:L4_Au_90						
Au_90_000	2A1	0.687	A1	0.3435	B1	0.191	0.103058
	2A2	0.718	A2	0.359	B2	0.209	0.117858
	2A3	0.602	A3	0.301	B3	0.083	0.039243
	S	1.0035				Total Area ellipses (μm^2)	0.260159
	Area triangle (μm^2)	0.190806		Total Area (nm^2)	450964.93		
Au_90_001	2A1	0.869	A1	0.4345	B1	0.196	0.133772
	2A2	0.731	A2	0.3655	B2	0.206	0.11827
	2A3	0.638	A3	0.319	B3	0.162	0.081176
	S	1.119				Total Area ellipses (μm^2)	0.333218
	Area triangle (μm^2)	0.228493		Total Area (nm^2)	561711.03		
Au_90_006	2A1	0.657	A1	0.3285	B1	0.212	0.109393
	2A2	0.697	A2	0.3485	B2	0.171	0.093609
	2A3	0.675	A3	0.3375	B3	0.071	0.03764
	S	1.0145				Total Area ellipses (μm^2)	0.240643
	Area triangle (μm^2)	0.197722		Total Area (nm^2)	438365.22		
	Sample:L4_Au_140						
Au_140_000	2A1	1.028	A1	0.514	B1	0.235	0.189736
	2A2	1.018	A2	0.509	B2	0.254	0.203082
	2A3	0.818	A3	0.409	B3	0.172	0.110502

	S	1.432				Total Area ellipses (μm^2)	0.503321
	Area triangle (μm^2)	0.383483		Total Area (nm^2)	886804.22		
Au_140_001	2A1	1.225	A1	0.6125	B1	0.171	0.164521
	2A2	1.003	A2	0.5015	B2	0.258	0.203241
	2A3	0.912	A3	0.456	B3	0.176	0.126066
	S	1.57				Total Area ellipses (μm^2)	0.493828
	Area triangle (μm^2)	0.449535		Total Area (nm^2)	943363.09		
Au_140_002	2A1	0.995	A1	0.4975	B1	0.202	0.157857
	2A2	1.039	A2	0.5195	B2	0.169	0.137909
	2A3	0.914	A3	0.457	B3	0.118	0.084707
	S	1.474				Total Area ellipses (μm^2)	0.380473
	Area triangle (μm^2)	0.41472		Total Area (nm^2)	795192.94		
Au_140_003	2A1	1.046	A1	0.523	B1	0.264	0.216883
	2A2	1.036	A2	0.518	B2	0.254	0.206673
	2A3	0.824	A3	0.412	B3	0.147	0.095134
	S	1.453				Total Area ellipses (μm^2)	0.51869
	Area triangle (μm^2)	0.393843		Total Area (nm^2)	912532.72		
Au_140_005	2A1	1.192	A1	0.596	B1	0.216	0.202218
	2A2	1.086	A2	0.543	B2	0.228	0.194471
	2A3	0.916	A3	0.458	B3	0.117	0.084173
	S	1.597				Total Area ellipses (μm^2)	0.480862
	Area triangle (μm^2)	0.474421		Total Area (nm^2)	955282.67		
Au_140_007	2A1	1.197	A1	0.5985	B1	0.217	0.204006
	2A2	1.1	A2	0.55	B2	0.189	0.163284
	2A3	1.005	A3	0.5025	B3	0.103	0.0813
	S	1.651				Total Area ellipses (μm^2)	0.448591
	Area triangle (μm^2)	0.516528		Total Area (nm^2)	965118.74		
	Sample:L4_Au_190						
Au_190_002	2A1	1.222	A1	0.611	B1	0.219	0.210187
	2A2	1.335	A2	0.6675	B2	0.135	0.141548
	2A3	1.207	A3	0.6035	B3	0.077	0.072994
	S	1.882				Total Area ellipses (μm^2)	0.424729
	Area triangle (μm^2)	0.677216		Total Area (nm^2)	1101945.4		
Au_190_003	2A1	1.29	A1	0.645	B1	0.295	0.298883
	2A2	1.361	A2	0.6805	B2	0.223	0.238371

	2A3	1.183	A3	0.5915	B3	0.119	0.110566
	S	1.917				Total Area ellipses (μm^2)	0.64782
	Area triangle (μm^2)	0.700374		Total Area (nm^2)	1348194.3		
Au_190_007	2A1	1.557	A1	0.7785	B1	0.3	0.366859
	2A2	1.497	A2	0.7485	B2	0.181	0.212809
	2A3	1.332	A3	0.666	B3	0.153	0.160061
	S	2.193				Total Area ellipses (μm^2)	0.73973
	Area triangle (μm^2)	0.914227		Total Area (nm^2)	1653956.7		
Au_190_008	2A1	1.12	A1	0.56	B1	0.191	0.168012
	2A2	1.325	A2	0.6625	B2	0.15	0.156098
	2A3	1.261	A3	0.6305	B3	0.144	0.142616
	S	1.853				Total Area ellipses (μm^2)	0.466726
	Area triangle (μm^2)	0.65158		Total Area (nm^2)	1118305.6		

Table I.4 Tabulated Results from horizontal sectioning of AFM images from residual nanoindentation impressions on decanethiol SAM on Gold (111) (Sample L4_decanethiol). Total contact areas calculated from trigonometry approach.

Sample Max disp/indent	Sample:L4_Deca_40						Areas Semi- ellipse
Deca_40_007	2A1	0.486	A1	0.243	B1	0.073	0.02786
	2A2	0.276	A2	0.138	B2	0.082	0.01777
	2A3	0.501	A3	0.2505	B3	0.111	0.04367
	S	0.6315				Area ellipses	0.08931
	Area triangle (μm^2)	0.065289		Total Area (nm^2)	154605.75		
Deca_40_008	2A1	0.521	A1	0.2605	B1	0.089	0.03641
	2A2	0.291	A2	0.1455	B2	0.112	0.02559
	2A3	0.479	A3	0.2395	B3	0.088	0.03310
	S	0.6455				Area ellipses	0.09512
	Area triangle (μm^2)	0.068873		Total Area (nm^2)	163994.78		
	Sample:L4_DECA_100						
Deca_90_003	2A1	0.909	A1	0.4545	B1	0.238	0.16991
	2A2	0.55	A2	0.275	B2	0.234	0.10108
	2A3	0.958	A3	0.479	B3	0.249	0.18735
	S	1.2085				Area ellipses	0.45834
	Area triangle (μm^2)	0.244345		Total Area (nm^2)	702690.82		
Deca_90_004	2A1	0.887	A1	0.4435	B1	0.245	0.17067
	2A2	0.537	A2	0.2685	B2	0.236	0.09953
	2A3	0.899	A3	0.4495	B3	0.2	0.14121
	S	1.1615				Area ellipses	0.41142
	Area triangle (μm^2)	0.228619		Total Area (nm^2)	640047.12		
Deca_90_007	2A1	0.918	A1	0.459	B1	0.178	0.17448
	2A2	0.517	A2	0.2585	B2	0.247	0.06902
	2A3	0.959	A3	0.4795	B3	0.243	0.13482
	S	1.197				Area ellipses	0.37833
	Area triangle (μm^2)	0.232483		Total Area (nm^2)	610815.28		
	Sample:L4_Deca_140						
Deca_140_002	2A1	1.253	A1	0.6265	B1	0.242	0.23815
	2A2	0.746	A2	0.373	B2	0.17	0.09960
	2A3	0.777	A3	0.3885	B3	0.179	0.10923

	S	1.388				Area ellipses	0.44699
	Area triangle (μm^2)	0.271113		Total Area (nm^2)	718105.49		
Deca_140_003	2A1	1.192	A1	0.596	B1	0.284	0.26587
	2A2	0.734	A2	0.367	B2	0.186	0.10722
	2A3	1.263	A3	0.6315	B3	0.226	0.22418
	S	1.5945				Area ellipses	0.59728
	Area triangle (μm^2)	0.427871		Total Area (nm^2)	1025158		
Deca_140_004	2A1	1.252	A1	0.626	B1	0.212	0.20846
	2A2	1.255	A2	0.6275	B2	0.2	0.19713
	2A3	1.334	A3	0.667	B3	0.231	0.242024
	S	1.9205				Area ellipses	0.647622
	Area triangle (μm^2)	0.70789		Total Area (nm^2)	1355512.2		
Deca_140_007	2A1	1.256	A1	0.628	B1	0.212	0.20913
	2A2	0.605	A2	0.3025	B2	0.2	0.09503
	2A3	1.242	A3	0.621	B3	0.231	0.22533
	S	1.5515				Area ellipses	0.52949
	Area triangle (μm^2)	0.366476		Total Area (nm^2)	895970.79		
	Sample:L4_Deca_190						
Deca_190_000	2A1	1.595	A1	0.7975	B1	0.196	0.24553
	2A2	0.964	A2	0.482	B2	0.171	0.12946
	2A3	1.744	A3	0.872	B3	0.202	0.276686
	S	2.1515				Area ellipses	0.65168
	Area triangle (μm^2)	0.761174		Total Area (nm^2)	1412859.6		
Deca_190_001	2A1	1.567	A1	0.7835	B1	0.158	0.19445
	2A2	1	A2	0.5	B2	0.234	0.18378
	2A3	1.651	A3	0.8255	B3	0.351	0.45513
	S	2.109				Area ellipses	0.83337
	Area triangle (μm^2)	0.761967		Total Area (nm^2)	1595343.3		
Deca_190_002	2A1	1.601	A1	0.8005	B1	0.226	0.28417
	2A2	1.007	A2	0.5035	B2	0.154	0.12179
	2A3	1.727	A3	0.8635	B3	0.283	0.38385
	S	2.1675				Area ellipses	0.78983
	Area triangle (μm^2)	0.792273		Total Area (nm^2)	1582105.1		
Deca_190_006	2A1	1.048	A1	0.524	B1	0.195	0.16050
	2A2	1.744	A2	0.872	B2	0.312	0.42735

	2A3	1.617	A3	0.8085	B3	0.399	0.506726
	S	2.2045				Area ellipses	1.09458
	Area triangle (μm^2)	0.830513		Total Area (nm^2)	1925100		

Table I.5 Tabulated Results from horizontal sectioning of AFM images from residual nanoindentation impressions on Gold (111) (Sample PHY3). Total contact areas calculated from trigonometry approach.

Sample Max disp/indent	Sample:PHY3_Au_40						Areas Semi- ellipse
Au_40_003	2A1	0.395	A1	0.1975	B1	0.126	0.039089267
	2A2	0.402	A2	0.201	B2	0.106	0.033467387
	2A3	0.552	A3	0.276	B3	0.065	0.028180086
	S	0.6745				Total Area ellipses (μm^2)	0.100736739
	Area triangle (μm^2)	0.079329		Total Area (nm^2)	180065.9586		
Au_40_004	2A1	0.364	A1	0.182	B1	0.14	0.040133846
	2A2	0.393	A2	0.1965	B2	0.087	0.026853549
	2A3	0.352	A3	0.176	B3	0.035	0.002391537
	S	0.5545				Total Area ellipses (μm^2)	0.069378932
	Area triangle (μm^2)	0.058776		Total Area (nm^2)	135329.1405		
Au_40_005	2A1	0.44	A1	0.22	B1	0.079	0.02730044
	2A2	0.44	A2	0.22	B2	0.094	0.032484068
	2A3	0.358	A3	0.179	B3	0.053	0.014902145
	S	0.619				Total Area ellipses (μm^2)	0.074686653
	Area triangle (μm^2)	0.071948		Total Area (nm^2)	146634.6336		
Au_40_006	2A1	0.356	A1	0.178	B1	0.219	0.061232782
	2A2	0.35	A2	0.175	B2	0.13	0.035735616
	2A3	0.329	A3	0.1645	B3	0.088	0.022738848
	S	0.5175				Total Area ellipses (μm^2)	0.119707246
	Area triangle (μm^2)	0.051369		Total Area (nm^2)	171076.65		
	Sample:PHY3_Au_90						
Au_90_000	2A1	0.573	A1	0.2865	B1	0.157	0.070655204
	2A2	0.677	A2	0.3385	B2	0.194	0.103152624
	2A3	0.675	A3	0.3375	B3	0.083	0.044001932
	S	0.9625				Total Area ellipses (μm^2)	0.21780976
	Area triangle (μm^2)	0.175419		Total Area (nm^2)	393228.5381		
Au_90_001	2A1	0.744	A1	0.372	B1	0.141	0.082391409
	2A2	0.658	A2	0.329	B2	0.255	0.131781958
	2A3	0.646	A3	0.323	B3	0.059	0.029934666
	S	1.024				Total Area ellipses (μm^2)	0.244108032
	Area triangle	0.199166		Total Area	443274.1403		

	(μm^2)			(nm^2)			
Au_90_003	2A1	0.793	A1	0.3965	B1	0.074	0.046088735
	2A2	0.773	A2	0.3865	B2	0.142	0.086210015
	2A3	0.74	A3	0.37	B3	0.065	0.037777652
	S	1.153				Total Area ellipses (μm^2)	0.170076401
	Area triangle (μm^2)	0.255231		Total Area (nm^2)	425306.9937		
	Sample:PHY3_Au_140						
Au_140_003	2A1	1.125	A1	0.5625	B1	0.17	0.150207399
	2A2	1.057	A2	0.5285	B2	0.144	0.119543884
	2A3	0.986	A3	0.493	B3	0.076	0.058854597
	S	1.584				Total Area ellipses (μm^2)	0.328605879
	Area triangle (μm^2)	0.478674		Total Area (nm^2)	807279.8707		
Au_140_004	2A1	1.055	A1	0.5275	B1	0.236	0.195548435
	2A2	0.985	A2	0.4925	B2	0.22	0.170195782
	2A3	0.928	A3	0.464	B3	0.135	0.098394682
	S	1.484				Total Area ellipses(μm^2)	0.464138899
	Area triangle (μm^2)	0.420275		Total Area (nm^2)	884413.6164		
Au_140_005	2A1	1.058	A1	0.529	B1	0.219	0.181978325
	2A2	1.002	A2	0.501	B2	0.228	0.179428923
	2A3	1.01	A3	0.505	B3	0.071	0.056320902
	S	1.535				Total Area ellipses (μm^2)	0.41772815
	Area triangle (μm^2)	0.452644		Total Area (nm^2)	870372.0124		
Au_140_006	2A1	1.121	A1	0.5605	B1	0.107	0.094206154
	2A2	1.054	A2	0.527	B2	0.227	0.187912794
	2A3	0.975	A3	0.4875	B3	0.141	0.107972613
	S	1.575				Total Area ellipses (μm^2)	0.39009156
	Area triangle (μm^2)	0.472784		Total Area (nm^2)	862875.4745		
	Sample:PHY3_Au_190						
Au_190_000	2A1	1.507	A1	0.7535	B1	0.347	0.410707476
	2A2	1.382	A2	0.691	B2	0.298	0.323455238
	2A3	1.239	A3	0.6195	B3	0.177	0.172240173
	S	2.064				Total Area ellipses (μm^2)	0.906402888
	Area triangle (μm^2)	0.80427		Total Area (nm^2)	1710672.399		
Au_190_001	2A1	1.456	A1	0.728	B1	0.186	0.212698389
	2A2	1.368	A2	0.684	B2	0.341	0.366378818
	2A3	1.186	A3	0.593	B3	0.159	0.148105673

	S	2.005				Total Area ellipses (μm^2)	0.727182881
	Area triangle (μm^2)	0.757801		Total Area (nm^2)	1484983.625		
Au_190_002	2A1	1.411	A1	0.7055	B1	0.201	0.222747559
	2A2	1.352	A2	0.676	B2	0.224	0.237856263
	2A3	1.245	A3	0.6225	B3	0.124	0.121249768
	S	2.004				Total Area ellipses (μm^2)	0.58185359
	Area triangle (μm^2)	0.766868		Total Area (nm^2)	1348722.076		
Au_190_003	2A1	1.428	A1	0.714	B1	0.201	0.225431264
	2A2	1.333	A2	0.6665	B2	0.288	0.301517497
	2A3	1.275	A3	0.6375	B3	0.094	0.09412997
	S	2.018				Total Area ellipses (μm^2)	0.62107873
	Area triangle (μm^2)	0.778442		Total Area (nm^2)	1399520.766		

Table I.6 Tabulated Results from horizontal sectioning of AFM images from residual nanoindentation impressions on dodecanethiol SAM on Gold (111) (Sample PHY3_dodecanethiol). Total contact area calculated from trigonometry approach.

Sample Max disp/indent	Sample:PHY3_Dode_40						Areas Semi-ellipse
Dode_40_005	2A1	0.409	A1	0.2045	B1	0.033	0.010601
	2A2	0.259	A2	0.1295	B2	0.053	0.010781
	2A3	0.424	A3	0.212	B3	0.097	0.032302
	S	0.546				Total Area ellipses (μm^2)	0.053684
	Area triangle (μm^2)	0.051177		Total Area (nm^2)	104860.85		
Dode_40_006	2A1	0.447	A1	0.2235	B1	0.187	0.065651
	2A2	0.259	A2	0.1295	B2	0.047	0.009561
	2A3	0.425	A3	0.2125	B3	0.065	0.021697
	S	0.5655				Total Area ellipses (μm^2)	0.096908
	Area triangle (μm^2)	0.053719		Total Area (nm^2)	150627.04		
Dode_40_008	2A1	0.422	A1	0.211	B1	0.065	0.021543
	2A2	0.211	A2	0.1055	B2	0.141	0.023366
	2A3	0.436	A3	0.218	B3	0.125	0.042804
	S	0.5345				Total Area ellipses (μm^2)	0.087714
	Area triangle (μm^2)	0.043773		Total Area (nm^2)	131486.96		
	Sample:PHY3_Dode_90						
Dode_90_005	2A1	0.839	A1	0.4195	B1	0.245	0.161443
	2A2	0.464	A2	0.232	B2	0.118	0.043002
	2A3	0.791	A3	0.3955	B3	0.224	0.13916
	S	1.047				Total Area ellipses (μm^2)	0.343605
	Area triangle (μm^2)	0.180285		Total Area (nm^2)	523889.49		
Dode_90_006	2A1	0.85	A1	0.425	B1	0.172	0.114825
	2A2	0.54	A2	0.27	B2	0.176	0.074644
	2A3	0.856	A3	0.428	B3	0.218	0.146562
	S	1.123				Total Area ellipses (μm^2)	0.336031
	Area triangle (μm^2)	0.218455		Total Area (nm^2)	554485.59		
Dode_00_007	2A1	0.852	A1	0.426	B1	0.22	0.147215
	2A2	0.499	A2	0.2495	B2	0.076	0.029785

	2A3	0.783	A3	0.3915	B3	0.144	0.088555
	S	1.067				Total Area ellipses (μm^2)	0.265556
	Area triangle (μm^2)	0.192369		Total Area (nm^2)	457924.55		
Dode_90_008	2A1	0.864	A1	0.432	B1	0.106	0.07193
	2A2	0.426	A2	0.213	B2	0.106	0.035465
	2A3	0.876	A3	0.438	B3	0.183	0.125906
	S	1.083				Total Area ellipses (μm^2)	0.233301
	Area triangle (μm^2)	0.179599		Total Area (nm^2)	412900.05		
	Sample:PHY3_Dode_140						
Dode_140_006	2A1	1.159	A1	0.5795	B1	0.157	0.142913
	2A2	0.711	A2	0.3555	B2	0.248	0.138488
	2A3	1.172	A3	0.586	B3	0.228	0.209871
	S	1.521				Total Area ellipses (μm^2)	0.491272
	Area triangle (μm^2)	0.394525		Total Area (nm^2)	885796.67		
Dode_140_007	2A1	1.241	A1	0.6205	B1	0.09	0.087721
	2A2	0.703	A2	0.3515	B2	0.212	0.117053
	2A3	1.256	A3	0.628	B3	0.26	0.25648
	S	1.6				Total Area ellipses (μm^2)	0.461253
	Area triangle (μm^2)	0.421001		Total Area (nm^2)	882253.89		
Dode_140_008	2A1	1.199	A1	0.5995	B1	0.309	0.290983
	2A2	0.701	A2	0.3505	B2	0.159	0.08754
	2A3	1.23	A3	0.615	B3	0.214	0.206733
	S	1.565				Total Area ellipses (μm^2)	0.585255
	Area triangle (μm^2)	0.407171		Total Area (nm^2)	992426.29		
Dode_140_009	2A1	1.276	A1	0.638	B1	0.269	0.269583
	2A2	0.726	A2	0.363	B2	0.1	0.05702
	2A3	1.328	A3	0.664	B3	0.274	0.285784
	S	1.665				Total Area ellipses (μm^2)	0.612388
	Area triangle (μm^2)	0.45272		Total Area (nm^2)	1065107.5		
	Sample:PHY3_Dode_190						
Dode_190_006	2A1	1.679	A1	0.8395	B1	0.28	0.369231
	2A2	0.988	A2	0.494	B2	0.212	0.164506
	2A3	1.573	A3	0.7865	B3	0.368	0.454639

	S	2.12				Total Area ellipses (μm^2)	0.988376
	Area triangle (μm^2)	0.760859		Total Area (nm^2)	1749235.3		
Dode_190_007	2A1	1.532	A1	0.766	B1	0.511	0.614851
	2A2	0.911	A2	0.4555	B2	0.13	0.093015
	2A3	1.493	A3	0.7465	B3	0.381	0.44676
	S	1.968				Total Area ellipses (μm^2)	1.154626
	Area triangle (μm^2)	0.656357		Total Area (nm^2)	1810982.6		
Dode_190_008	2A1	1.495	A1	0.7475	B1	0.261	0.306458
	2A2	1.111	A2	0.5555	B2	0.2	0.174515
	2A3	1.543	A3	0.7715	B3	0.395	0.478688
	S	2.0745				Total Area ellipses (μm^2)	0.959662
	Area triangle (μm^2)	0.784623		Total Area (nm^2)	1744285.1		
Dode_190_009	2A1	1.715	A1	0.8575	B1	0.377	0.507803
	2A2	1.139	A2	0.5695	B2	0.206	0.184281
	2A3	1.527	A3	0.7635	B3	0.411	0.492914
	S	2.1905				Total Area ellipses (μm^2)	1.184998
	Area triangle (μm^2)	0.852456		Total Area (nm^2)	2037453.8		

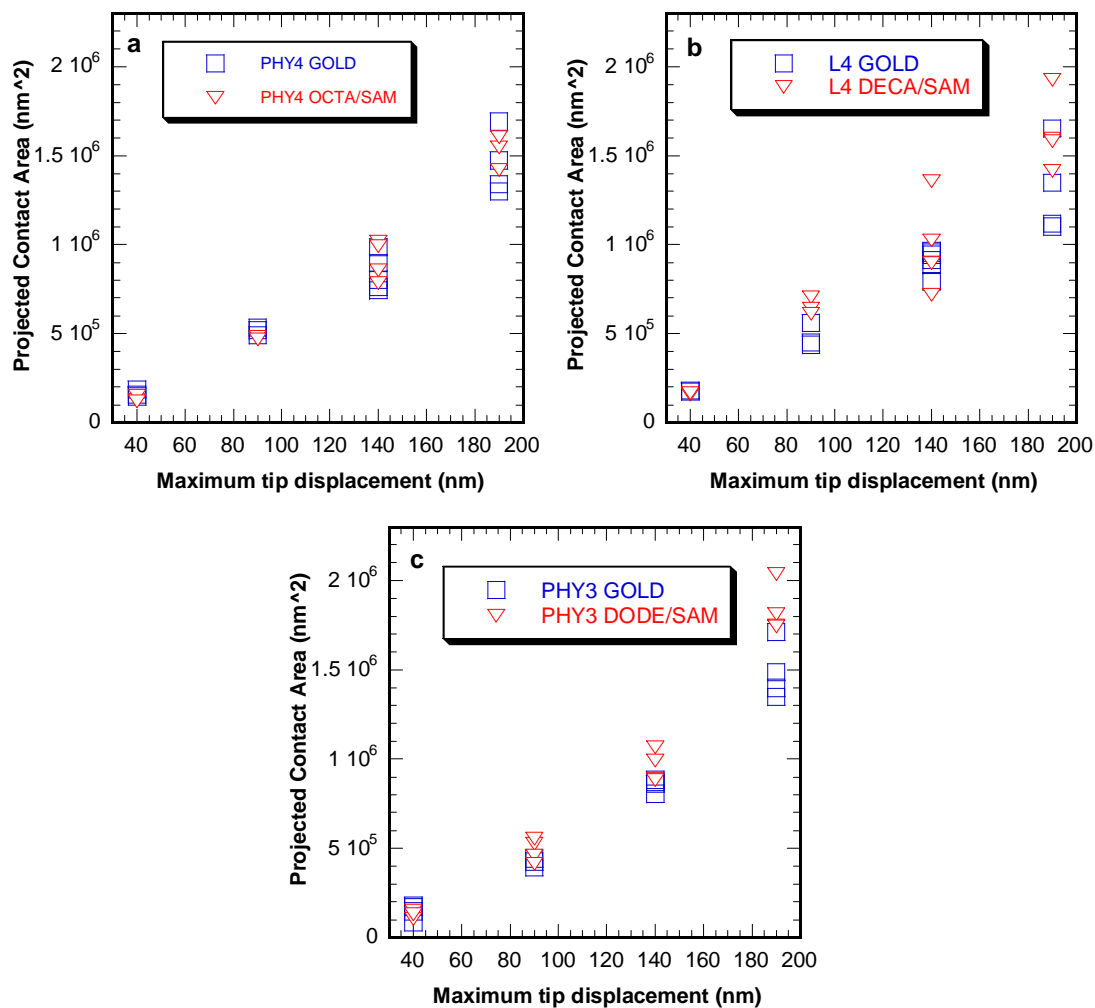


Figure I.1 Nanoindentation projected contact areas from indented gold (blue rectangle) and SAM (red triangle) as a function of maximum tip displacements for (a) eight carbons SAM, (b) ten carbons SAM, and (c) twelve carbons SAM. Projected areas were approximated from AFM image analysis.

Appendix J

Elastic Modulus (E_{AFM}), Hardness (H_{AFM}) and Pile-up Volumes Obtained from AFM Imaging

Table J.1 Hardnesses and Reduced Elastic Moduli values approximated from AFM imaging of nanoindentation projected contact area on gold (Sample PHY4).

PHY4 Gold	Contact Area (nm ²)	Max Load (μ N)	Stiffness (μ N/nm)	Approximated Hardness (Gpa)	Approximated Er (Gpa)
50_004	156653.5222	176.528168	28.284215	1.126870086	63.3313854
50_005	185027.2986	177.210493	28.445291	0.957753231	58.60537074
50_006	146792.5309	164.168594	26.166821	1.118371575	60.52627199
100_006	519546.7697	1017.438233	37.697273	1.958318851	46.34923292
100_007	533528.0969	1018.902061	36.902077	1.909743961	44.77309367
100_008	492252.8774	1034.362443	38.262938	2.101282675	48.33137191
150_000	759749.2806	2484.520393	55.943905	3.270184595	56.88039055
150_001b	985319.954	2457.454896	55.26828	2.494067928	49.34376127
150_003	802473.8325	2521.746415	57.999084	3.142465602	57.3786909
150_003b	742529.121	2521.746415	57.999084	3.39615827	59.64984643
150_004	894902.3921	2515.143526	56.976135	2.810522743	53.37649984
200_004	1474707.059	4494.04726	72.018581	3.047416931	52.55773263
200_005	1339344.682	4544.078344	73.795513	3.392762449	56.5104438
200_006	1300080.387	4540.763334	74.516016	3.492678898	57.9174543
200_007	1692893.92	4536.687391	73.189759	2.679841506	49.85174733

Table J.2 Hardnesses and Reduced Elastic Moduli values approximated from AFM imaging of nanoindentation projected contact area on Octa/SAM (Sample PHY4).

PHY4 OCTA/SAM	Contact Area (nm ²)	Max Load (μ N)	Stiffness (μ N/nm)	Approximated Hardness (Gpa)	Approximated Er (Gpa)
50_006	129105.4201	162.840782	28.190583	1.261300895	69.53072543
50_008b	149262.656	172.327693	28.791274	1.154526508	66.04352432
50_009	118988.8796	173.627177	28.349716	1.459188267	72.83505721
100_006	475939.3359	1029.868527	37.86473	2.163865117	48.64116912
100_007	483075.6524	1021.756126	38.803673	2.115105824	49.47777967
100_008	466236.4942	1026.349641	38.326957	2.20134986	49.74462347
150_005	858257.2394	2422.321804	54.320349	2.822372702	51.96354299
150_006	1017316.437	2384.463764	53.244506	2.34387618	46.78339255
150_007	992545.311	2465.388969	54.904281	2.483905714	48.84003633
150_008	783653.6322	2486.531473	56.421569	3.172998083	56.48433555
200_005	1546677	4323.28615	68.46653	2.79520944	48.78917165
200_006	1420037.21	4411.054145	70.363176	3.10629476	52.32876829
200_007	1604577.9	4419.915532	69.701529	2.754565877	48.76484437

Table J.3 Hardnesses and Reduced Elastic Moduli values approximated from AFM imaging of nanoindentation projected contact area on gold (Sample L4).

L4 Gold	Contact Area (nm ²)	Max Load (μN)	Stiffness (μN/nm)	Approximated Hardness (Gpa)	Approximated Er (Gpa)
50_001	174473.6506	198.641341	25.399338	1.138517709	53.88928409
50_006	179272.4129	226.835618	24.052162	1.265312461	50.34337523
100_000	450964.9288	1128.317409	37.02813	2.502007001	48.86583635
100_001	561711.0259	1081.001909	35.231206	1.924480487	41.65968445
100_006	438365.2236	1079.773433	35.977635	2.463182239	48.15700902
150_000	886804.2232	2595.021955	55.354404	2.926262513	52.09346475
150_001	943363.0857	2583.201587	55.339225	2.738289876	50.49386033
150_002	795192.9418	2587.116234	54.013528	3.253444665	53.67984182
150_003	912532.723	2543.877109	53.703776	2.787710561	49.82250276
150_005	955282.674	2609.813266	54.093072	2.731980111	49.0479247
150_007	965118.7436	2591.869793	54.484119	2.685544976	49.15011049
200_002	1101945.371	4738.045849	72.835039	4.299710287	61.49010933
200_003	1348194.35	4716.625842	72.302419	3.498476198	55.18505973
200_007	1653956.671	4619.283652	70.06539	2.7928686	48.28212992
200_008	1118305.65	4745.098642	72.872929	4.243114254	61.07042

Table J.4 Hardnesses and Reduced Elastic Moduli values approximated from AFM imaging of nanoindentation projected contact area on Deca/SAM (Sample L4).

L4 Deca/SAM	Contact Area (nm ²)	Max Load (μN)	Stiffness (μN/nm)	Approximated Hardness (Gpa)	Approximated Er (Gpa)
50_007	154605.748	153.246734	21.737422	0.99120981	48.99369105
50_008	163994.7751	161.597882	20.192353	0.985384333	44.18927384
100_003	702690.8237	1050.970441	33.094453	1.495637065	34.98791049
100_004	640047.1221	1034.8421	33.806308	1.616821737	37.44869688
100_007	610815.2805	1049.61096	33.124864	1.71837705	37.56160126
150_002	718105.4929	2460.890733	49.805133	3.426920915	52.08646941
150_003	1025158.012	2395.913211	49.734329	2.337116019	43.53171715
150_004	1355512.246	2480.733577	50.409655	1.830107831	38.37133799
150_007	895970.7934	2441.598376	49.590263	2.725087016	46.4295448
200_000	1412859.574	4535.006844	66.831786	3.209807208	49.82857972
200_001	1595343.276	4383.481754	65.67292	2.747673068	46.07912187
200_002	1582105.07	4334.550867	65.776204	2.739736411	46.34427429
200_006	1925100.003	4362.718102	65.554289	2.266229336	41.87158537

Table J.5 Hardnesses and Reduced Elastic Moduli values approximated from AFM imaging of nanoindentation projected contact area on gold (Sample PHY3).

PHY3 Gold	Contact Area (nm ²)	Max Load (μN)	Stiffness (μN/nm)	Approximated Hardness (Gpa)	Approximated Er (Gpa)
50_003	180065.9586	183.288348	28.958681	1.017895606	60.47946056
50_004	84885.10246	171.375516	26.934773	2.018911576	81.92991831
50_005	146634.6336	167.402407	27.354883	1.141629388	63.30842703
50_006	171076.65	162.560979	25.34471	0.950223066	54.3046349
100_000	393228.5381	1056.214905	38.936022	2.686007761	55.02676796
100_001	443274.1403	1051.766456	38.462573	2.372722341	51.19730212
100_003	425306.9937	1022.295374	37.446182	2.403664621	50.88634082
150_003	807279.8707	2562.975276	56.556919	3.174828667	55.78515211
150_004	884413.6164	2492.587311	54.62423	2.818350221	51.47573525
150_005	870372.0124	2510.732574	56.498099	2.884666026	53.66934774
150_006	862875.4745	2503.601225	55.651845	2.901462956	53.09461121
200_000	1710672.399	4520.685057	72.748476	2.642636345	49.29301883
200_001	1484983.625	4515.520402	72.61964	3.040788009	52.8126792
200_002	1348722.076	4557.679163	73.528514	3.379257479	56.10990025
200_003	1399520.766	4623.116681	73.523558	3.303356974	55.07845924

Table J.6 Hardnesses and Reduced Elastic Moduli values approximated from AFM imaging of nanoindentation projected contact area on Dode/SAM (Sample PHY3).

PHY3 DODE/SAM	Contact Area (nm ²)	Max Load (μN)	Stiffness (μN/nm)	Approximated Hardness (Gpa)	Approximated Er (Gpa)
50_005	104860.8469	133.70157	25.617089	1.275038052	70.10807415
50_006	150627.0422	151.259958	27.136964	1.004201874	61.96618014
50_008	131486.9577	152.394274	25.124094	1.159006769	61.40362516
100_005	523889.4926	974.733318	36.185916	1.860570467	44.3062167
100_006	554485.591	983.037263	36.283755	1.77288153	43.18292281
100_007	457924.5482	966.005208	35.746164	2.109529205	46.81418008
100_008	412900.0484	991.067595	37.381389	2.400260303	51.5558449
150_006	885796.6735	2351.560051	51.891985	2.654740214	48.86278337
150_007	882253.8912	2299.877251	50.2604	2.606820184	47.42136929
150_008	992426.2899	2339.824947	50.944483	2.357681342	45.32032021
150_009	1065107.499	2340.577393	51.338073	2.19750344	44.08468913
200_006	1749235.324	4270.895866	65.84183	2.44157879	44.11870074
200_007	1810982.574	4246.257561	65.633472	2.344725798	43.22282853
200_008	1744285.125	4294.346602	65.529658	2.4619522	43.97178577
200_009	2037453.792	4229.18265	65.869163	2.075719541	40.89622312

Average Hardness (H_{AFM}) Obtained Using AFM Contact Areas

Table J.7 Averaged H_{AFM} from AFM imaging of nanoindentation projected contact area on Au(111) and Au(111) modified with SAMs.

Max tip displacement (nm)	PHY4 Au H (GPa)	Standard Error	PHY4 Octa/SAM H (GPa)	Standard Error	% difference
40	1.07	0.06	1.29	0.09	-20.98
90	1.99	0.06	2.16	0.02	-8.56
140	3.02	0.18	2.71	0.19	10.48
190	3.15	0.18	2.89	0.11	8.49

Max tip displacement (nm)	L4 Au H (GPa)	Standard Error	L4 Deca/SAM H (GPa)	Standard Error	% difference
40	1.20	0.06	0.99	0.00	17.77
90	2.30	0.19	1.61	0.06	29.88
140	2.85	0.09	2.58	0.34	9.60
190	3.71	0.36	2.74	0.19	26.09

Max tip displacement (nm)	PHY3 Au H (GPa)	Standard Error	PHY3 Dode/SAM H (GPa)	Standard Error	% difference
40	1.09	0.07	1.15	0.08	-4.76
90	2.49	0.10	2.04	0.14	18.16
140	2.94	0.08	2.45	0.11	16.66
190	3.09	0.17	2.33	0.09	24.60

Average Reduced Elastic Moduli (E_{AFM}) Obtained Using AFM Contact Areas

Table J.8 Averaged E_{AFM} from AFM imaging of nanoindentation projected contact area on Au(111) and Au(111) modified with SAMs.

Max tip displacement (nm)	PHY4 Au Er (GPa)	Standard Error	PHY4 Octa/SAM Er (GPa)	Standard Error	% difference
40	60.82	1.37	69.47	1.96	-14.22
90	46.48	1.03	49.29	0.33	-6.03
140	55.33	1.80	51.02	2.11	7.79
190	54.21	1.84	49.96	1.18	7.84
Max tip displacement (nm)	L4 Au Er (GPa)	Standard Error	L4 Deca/SAM Er (GPa)	Standard Error	% difference
40	52.12	1.25	46.59	2.40	10.60
90	46.23	2.29	36.67	0.84	20.68
140	50.71	0.75	45.10	2.86	11.06
190	56.51	3.10	46.03	1.63	18.54

Max tip displacement (nm)	PHY3 Au Er (GPa)	Standard Error	PHY3 Dode/SAM Er (GPa)	Standard Error	% difference
40	60.75	2.33	64.49	2.81	-6.17
90	52.37	1.33	46.46	1.86	11.28
140	53.51	0.89	46.42	1.07	13.24
190	53.32	1.51	43.05	0.93	19.26

Pile-up Volumes

Table J.9 Pile-up volumes in nm^3 for indent performed on clean Au and different chain length SAMs. Negative % difference represents an increase in the pile-up volume.

Tip displ (nm)	Au nm^3	Est. error	Octa/SAM nm^3	Est. error	%diff	Deca/SAM nm^3	Est. error	%diff	Dode/SAM nm^3	Est. error	%diff
40	3.E+06	2.E+05	4.E+06	2.E+05	-36	1.E+06	4.E+05	49	4.E+06	6.E+05	-46
90	1.E+07	1.E+06	1.E+07	1.E+06	-14	9.E+06	2.E+06	28	2.E+07	3.E+06	-47
140	2.E+07	8.E+05	4.E+07	2.E+06	-105	4.E+07	2.E+06	-102	4.E+07	1.E+06	-105
190	4.E+07	2.E+06	6.E+07	5.E+04	-70	6.E+07	1.E+07	-73	1.E+08	3.E+06	-214

8 REFERENCES

- ¹ M. Mrksich, L.E. Dike, J. Tien, D.E. Ingber, and G.M. Whitesides, "Using Microcontact Printing to Pattern the Attachment of Mammalian Cells to Self-Assembled Monolayers of Alkanethiolates on Transparent Films of Gold and Silver," *Experimental Cell Research* **235** (2), 305-313 (1997).
- ² K. Wadu-Mesthrige, S. Xu, N. A. Amro, and G. Y. Liu, "Fabrication and imaging of nanometer-sized protein patterns," *Langmuir* **15** (25), 8580-8583 (1999).
- ³ M. Mrksich and G. M. Whitesides, "Using self-assembled monolayers to understand the interactions of man-made surfaces with proteins and cells," *Annual Review of Biophysics and Biomolecular Structure* **25**, 55-78 (1996).
- ⁴ J. D. Kiely, R. Q. Hwang, and J. E. Houston, "Effect of Surface Steps on the Plastic Threshold in Nanoindentation," *Physical Review Letters* **81** (20), 4424 (1998).
- ⁵ M. Godin, P.J. Williams, and V.T. Cossa, "Surface stress, kinetics, and structure of alkanethiol self-assembled monolayers," *Langmuir* **20** (17), 7090–7096 (2004).
- ⁶ R. Berges, E. Delamarche, H.P. Lang, C. Gerber, J.K. Cimzewski, E. Meyer, and H-J Guntherodt, "Surface stress in the self-assembly of alkanethiols on gold probed by a force microscopy technique," *Appl. Phys. A.* **66**, S55-S59 (1998).
- ⁷ R. Berges, E. Delamarche, H.P. Lang, C. Gerber, J.K. Gimzewski, E. Meyer, and H-J Guntherodt, "Surface stress in the self-assembly of alkanethiols on gold," *Science* **276**, 2021-2024 (1997).

- 8 A.R.C Westwood, J.S Ahearn, and J.J Mills, "Developments in the theory and application of chemomechanical effects " *Colloids and Surfaces* **2** (1), 1-35 (1980).
- 9 E.N.DA C. Andrade, R.F.Y Randall, and M.J. Makin, "The reh binder effect," *Proc. Phys. Soc. B* **63**, 990-995 (1950).
- 10 S.V. Hainsworth and T.F. Page, "Nanoindentation studies of the chemomechanical effect in sapphire " *Journal of Materials Science* **29** (21) (1994).
- 11 W.D. Callister Jr., *Materials Science and Engineering and Introduction*. (John Wiley & Sons, Inc, New York, 2000).
- 12 J.G. Tweeddale, *The Mechanical Properties of Metals*. (New York, 1964).
- 13 T. Suzuki, S. Takeuchi, and H. Yoshinaga, *Dislocation Dynamics and Plasticity*. (Springer-Verlag, Berlin, 1991).
- 14 D. Hull and D.J. Bacon, *Introduction to Dislocations*. (Butterworth-Heinemann, Oxford, 1965).
- 15 R. Peierls, "The size of a dislocation," *Proc. Phys. Soc.* **52**, 34-37 (1940).
- 16 F.R.N. Nabarro, "Dislocations in a simple cubic lattice," *Proc. Phys. Soc.* **59**, 256-272 (1947).
- 17 J. Weertman and J.R. Weertmann, *Elementary Dislocation Theory*. (Oxford University Press, New York, Oxford, 1992).
- 18 Q.H. Fang and Y.W. Liu, "Size-dependent elastic interaction between a screw dislocation and a circular nano-hole with surface stress," *Phys. Stat. Sol (b)* **243** (4) (2006).

- 19 I. Kovacs and L. Zsoldos, *Dislocations and Plastic Deformation*. (Pergamon Press, Oxford, New York, Toronto, Sydney, Braunschweig, 1973).
- 20 J.W Gibbs, *The Scientific Paper of J. Willard Gibbs*. (Longmans-Green, London, 1906), p.55.
- 21 P. Gumbsch and M. S. Daw, "Interface stresses and their effects on the elastic moduli of metallic multilayers," *Physical Review B* **44** (8), 3934 (1991).
- 22 C.W. Mays, J.S. Vermaak, and D. Kuhlmann-Wilsdorf, "On surface stress and surface tension: II. Determination of the surface stress of gold," *Surface Science* **12** (2), 134-140 (1968).
- 23 T. Young, "An essay on the cohesion of fluids," *Philosophical Transactions of the Royal Society of London* **95**, 65-87 (1805).
- 24 F.M. Fowkes, "Atractive forces at interfaces," *Industrial and Engineering Chemistry* **56**, 40-52 (1964).
- 25 D. K. Owens and R.C. Wendt, "Estimation of the surface free energy of polymers," *Journal of Applied Polymer Science* **13**, 1741-1747 (1969).
- 26 Sneddon, "The relation between load and penetration in the axisymmetric Boussinesq problem for a punch of arbitrary profile," *Int. J. Eng. Sci.* **3**, 47-56 (1965).
- 27 K. L. Johnson, *Contact Mechanics*. (Cambridge University Press, Cambridge [Cambridgeshire] ; New York, 1985), pp.xi, 452 p.
- 28 A.C. Fischer-Cripps, *Nanoindentation*, 2nd ed. (Springer, New York, 2004), pp.xxii, 263 p.

- 29 J.L. Loubet, J.M. Georges, O. Marchesini, and G. Meille, "Vickers indentation curves of magnesium oxide (MgO)," *J. Tribol. Trans. ASME* **106**, 43–48 (1984).
- 30 M.F. Doerner and W.D. Nix, "A method for interpreting the data from depth-sensing indentation instruments," *J. Mater. Res.* **1** (4), 601-609 (1986).
- 31 W.C. Oliver and G.M. Pharr, "An improved technique for determining hardness and elastic modulus using load and displacement sensing indentation experiments," *J. Mater. Res.* **7** (6), 1564-1583 (1992).
- 32 J.S. Field and M.V. Swain, "A simple predictive model for spherical indentation," *J. Mater. Res.* **8** (2), 297-306 (1993).
- 33 N. Schawarzer, "Elastic surface deformation due to indenters with arbitrary symmetry of revolution," *J. Phys. D. Appl. Phys* **37** (2004).
- 34 H. Hertz and J Reine Angew, "On the contact of elastic solids " *Math.* **92**, 156-171 (1881).
- 35 H. Hertz, "On hardness," *Verh. Ver. Beförderung Gewerbe Fleisses* **61**, 410 (1882).
- 36 K. L. Johnson, K. Kendall, and A. D. Roberts, "Surface Energy and the Contact of Elastic Solids," *Proceedings of the Royal Society of London. Series A, Mathematical and Physical Sciences* **324** (1558), 301-313 (1971).
- 37 B. V. Derjaguin, V. M. Muller, and Yu P. Toporov, "Effect of contact deformations on the adhesion of particles," *Journal of Colloid and Interface Science* **53** (2), 314-326 (1975).
- 38 R. S Bradley, "The cohesive force between solid surfaces and the surface energy of solids," *Philosophical Magazine* **13** (7), 853 - 862 (1932).

- ³⁹ J. Drelich, "Adhesion forces measured between particles and substrates with nano-roughness," *Minerals & Metallurgical Processing* **23** (4), 226-232 (2006).
- ⁴⁰ K.N.G. Fuller and D. Tabor, "The effect of surface roughness on the adhesion of elastic solids," *Proc. R. Soc. Lon.* **A324**, 327-342 (1975).
- ⁴¹ J.E Lennard-Jones and B.M. Dent, "Cohesion at a crystal surface," *Trans. Faraday Soc.* **24**, 92-108 (1928).
- ⁴² W. C. Bigelow, D. L. Pickett, and W. A. Zisman, "Oleophobic monolayers : I. Films adsorbed from solution in non-polar liquids," *Journal of Colloid Science* **1** (6), 513-538 (1946).
- ⁴³ R.G. Nuzzo and D.L. Allara, "Adsorption of bifunctional organic disulfides on gold surfaces," *J. Am. Chem. Soc.* **105** (13), 4481-4483 (1983).
- ⁴⁴ E.B. Troughton, C.D. Bain, G.M. Whitesides, R.G. Nuzzo, D.L. Allara, and M.D. Porter, "Monolayer films prepared by the spontaneous self-assembly of symmetrical and unsymmetrical dialkyl sulfides from solution onto gold substrates: structure, properties, and reactivity of constituent functional groups," *Langmuir* **4** (2), 365-385 (1988).
- ⁴⁵ R.G. Nuzzo, F.A. Fusco, and D.L. Allara, "Spontaneously organized molecular assemblies. 3. Preparation and properties of solution adsorbed monolayers of organic disulfides on gold surfaces," *J. Am. Chem. Soc.* **109** (8), 2358-2368 (1987).
- ⁴⁶ C.D. Bain, E. B. Troughton, Y.T Tao, J. Evall, G.M. Whitesides, and R.G. Nuzzo, "Formation of monolayer films by the spontaneous assembly of organic thiols from solution onto gold," *J. Am. Chem. Soc.* **111** (1), 321-335 (1989).

- ⁴⁷ L. Salem, "Attractive Forces between Long Saturated Chains at Short Distances," J. Chem. Phys. **37** (9), 2100-2113 (1962).
- ⁴⁸ P.E. Laibinis, G.M. Whitesides, D.L. Allara, Y.T. Tao, A.N. Parikh, and R.G. Nuzzo, "Comparison of the structures and wetting properties of self-assembled monolayers of n-alkanethiols on the coinage metal surfaces, copper, silver, and gold," J. Am. Chem. Soc. **113** (19), 7152-7167 (1991).
- ⁴⁹ C.E.D. Chidsey and D.N. Loiacono, "Chemical functionality in self-assembled monolayers: structural and electrochemical properties," Langmuir **6** (3), 682-691 (1990).
- ⁵⁰ K.C. Eapen, S.T. Patton, and J.S. Zabinski, "Lubrication of Microelectromechanical Systems (MEMS) Using Bound and Mobile Phases of Fomblin Zdol®," Tribology Letters **12** (2002).
- ⁵¹ T. Patton Steven, C. Eapen Kalathil, S. Zabinski Jeffrey, H. Sanders Jeffrey, and A. Voevodin Andrey, "Lubrication of microelectromechanical systems radio frequency switch contacts using self-assembled monolayers," Journal of Applied Physics **102** (2), 024903 (2007).
- ⁵² O. M. Magnussen, B. M. Ocko, M. Deutsch, M. J. Regan, P. S. Pershan, D. Abernathy, G. Grubel, and J. F. Legrand, "Self-assembly of organic films on a liquid metal," Nature **384** (6606), 250-252 (1996).
- ⁵³ C.W. Sheen, J.X. Shi, J. Maartensson, A.N. Parikh, and D.L. Allara, "A new class of organized self-assembled monolayers: alkane thiols on gallium arsenide(100)," J. Am. Chem. Soc. **114** (4), 1514-1515 (1992).

- ⁵⁴ Y. Gu, Z. Lin, R. A. Butera, V. S. Smentkowski, and D. H. Waldeck, "Preparation of Self-Assembled Monolayers on InP," *Langmuir* **11** (6), 1849-1851 (1995).
- ⁵⁵ U. Srinivasan, M. R. Houston, R. T. Howe, and R. Maboudian, "Alkyltrichlorosilane-based self-assembled monolayer films for stiction reduction in silicon micromachines," *Journal of Microelectromechanical Systems* **7** (2), 252-260 (1998).
- ⁵⁶ R. Maboudian, W.R. Ashurst, and C. Carraro, "Self-assembled monolayers as anti-stiction coatings for MEMS: characteristics and recent developments," *Sensors and Actuators A: Physical* **82** (1-3), 219-223 (2000).
- ⁵⁷ R. W. Carpick and M. Salmeron, "Scratching the Surface: Fundamental Investigations of Tribology with Atomic Force Microscopy," *Chemical Reviews* **97** (4), 1163-1194 (1997).
- ⁵⁸ N.K. Chaki and K. Vijayamohan, "Self-assembled monolayers as a tunable platform for biosensor applications," *Biosensors and Bioelectronics* **17** (1-2), 1-12 (2002).
- ⁵⁹ K.L. Christman, V.D. Enriquez-Rios, and H.D. Maynard, "Nanopatterning proteins and peptides," *Soft Matter* **2** (11), 928-939 (2006).
- ⁶⁰ T. Pham, D. Lai, D. Ji, W. Tuntiwechapikul, J.M. Friedman, and T. Randall Lee, "Well-ordered self-assembled monolayer surfaces can be used to enhance the growth of protein crystals," *Colloids and Surfaces B: Biointerfaces* **34** (3), 191-196 (2004).

- ⁶¹ U. Meyer, A. Büchter, H. P. Wiesmann, U. Joos, and D. B. Jones, "Basic reactions of osteoblasts on structured material surfaces," *European Cells and Materials* **9**, 39-49 (2005).
- ⁶² A. Ulman, *An introduction to Ultrathin Organic Films : from Langmuir-Blodgett to Self-Assembly*. (Academic Press, Boston, 1991), pp.xxiii, 442 p.
- ⁶³ A. Ulman, *Self-Assembled Monolayers of Thiols*. (Academic Press, San Diego, 1998).
- ⁶⁴ H. Klein, W. Blanc, R. Pierrisnard, C. Fauquet, and P. Dumas, "Self-assembled monolayers of decanethiol on Au(111)/mica," *Eur. Phys. J. B* **14** (2), 371-376 (2000).
- ⁶⁵ H. Fujiwara, *Spectroscopic Ellipsometry : Principles and Applications*. (John Wiley & Sons, Chichester, England ; Hoboken, NJ, 2007), pp.xviii, 369 p.
- ⁶⁶ C. R. Brundle, C.A. Evans, and S. Wilson, *Encyclopedia of Materials Characterization : surfaces, interfaces, thin films*. (Butterworth-Heinemann; Manning, Boston, Greenwich, CT, 1992), pp.xix, 751 p.
- ⁶⁷ J.R. Ferraro, K. Nakamoto, and C.W. Brown, *Introductory Raman Spectroscopy*. (Academic Press, London, 1994).
- ⁶⁸ G.J. Kluth, C. Carraro, and R. Maboudian, "Direct observation of sulfur dimers in alkanethiol self-assembled monolayers on Au(111)," *Physical Review B* **59** (16), R10449 (1999).
- ⁶⁹ P. Gupta, A. Ulman, S. Fanfan, A. Korniaikov, and K. Loos, "Mixed self-assembled monolayers of alkanethiolates on ultrasmooth gold do not exhibit contact-angle hysteresis," *J. Am. Chem. Soc.* **127** (1), 4-5 (2005).

- 70 C. Lages and E. Mendez, "Contact angle measurements under thermodynamic equilibrium conditions," *Analytical and Bioanalytical Chemistry* **388** (8), 1689-1692 (2007).
- 71 W.C. Oliver and G.M. Pharr, "Measurement of hardness and elastic modulus by instrumented indentation: Advances in understanding and refinements to methodology," *J. Mater. Res.* **19** (1), 3 - 20 (2004).
- 72 J.B. Pethica, R. Hutchings, and W.C. Oliver, "Hardness measurement at penetration depths as small as 20 nm," *Philosophical Magazine A* (48) (1983).
- 73 D. Stone, W. R. LaFontaine, P. Alexopoulos, T. -W. Wu, and Che-Yu Li, "An investigation of hardness and adhesion of sputter-deposited aluminum on silicon by utilizing a continuous indentation test," *J. Mater. Res.* **3** (1), 141-147 (1988).
- 74 M.Kh. Shorshorov, S.I. Bulychev, and V.O. Alekhin, "Work of plastic and elastic deformation during indenter indentation," *Sov. Phys. Dokl.* **26** (8), 769-771 (1981).
- 75 M. Sakai, "Energy principle of the indentation-induced inelastic surface deformation and hardness of brittle materials," *Acta. Metal. Mater.* **41** (6), 1751-1758 (1993).
- 76 R. Desikan, S. Armel, H.M. Meyer III, and T. Thundat, "Effect of chain length on nanomechanics of alkanethiol self-assembly," *Nanotechnology* **18**, 1-6 (2007).
- 77 A. Bolshakov and G.M. Pharr, "Influences of pile-up on the measurement of mechanical properties by load and depth sensing indentation techniques," *J. Mater. Res.* **13** (4), 1049-1058 (1998).

- 78 G. Binnig, C. F. Quate, and Ch. Gerber, "Atomic Force Microscope," *Physical Review Letters* **56** (9), 930 (1986).
- 79 J. Drelich and K. Mittal, *Atomic Force Microscopy in Adhesion Studies* (Leiden, Boston, 2005).
- 80 F. P. Bowden and D. Tabor, *The Friction and Lubrication of Solids*. (Oxford University Press, Oxford, 1950).
- 81 D. Tabor, *The Hardness of Metals*. (Clarendon Press, Oxford, 1951).
- 82 L.Z. Liu, Y.W. Bao, and Y.C. Zhou, "Effects of strain hardening and residual stress in impression on the instrumented indentation technique," *J. Mater. Res.* **21** (7), 1680-1686 (2006).
- 83 R. Larson, B.H. Edwards, and R.P. Hostetler, *Calculus 7th edition*. (Houghton Mifflin Company).
- 84 R.L. Burden and J.D. Faires, *Numerical Analysis*. (Brooks/Cole, 2000).
- 85 A. Lio, D. H. Charych, and M. Salmeron, "Comparative Atomic Force Microscopy Study of the Chain Length Dependence of Frictional Properties of Alkanethiols on Gold and Alkylsilanes on Mica," *J. Phys. Chem. B* **101** (19), 3800-3805 (1997).
- 86 R.G. Nuzzo, L.H. Dubois, and D.L. Allara, "Fundamental studies of microscopic wetting on organic surfaces. 1. Formation and structural characterization of a self-consistent series of polyfunctional organic monolayers," *J. Am. Chem. Soc.* **112** (2), 558-569 (1990).
- 87 A. Mathur, P. Sharma, and R.C. Cammarata, "Negative Surface Energy: clearing up the confusion," *Nature Materials* **4** (3) (2005).

- ⁸⁸ Y.T Cheng and C.M Cheng, "Relationship between hardness, elastic modulus, and the work of indentation," Appl. Phys. Lett. **73** (5), 614-616 (1998).
- ⁸⁹ F.W. Del Rio, C. Jaye, D.A. Fischer, and R.F. Cook, "Elastic and adhesive properties of alkanethiol self-assembled monolayers on gold," Appl. Phys. Lett. **94** (13), 131909 (2009).
- ⁹⁰ Frank W. DelRio, Cherno Jaye, Daniel A. Fischer, and Robert F. Cook, "Elastic and adhesive properties of alkanethiol self-assembled monolayers on gold," Appl. Phys. Lett. **94** (13), 131909 (2009).
- ⁹¹ O. Levine and W. A. Zisman, "Physical properties of monolayers adsorbed at the solid-air interface. II. Mechanical durability of aliphatic polar compounds and effect of halogenation," **61** (9), 1188-1196 (1957).
- ⁹² X.D. Xiao, J. Hu, D. H. Charych, and M. Salmeron, "Chain length dependence of the frictional properties of alkylsilane molecules self-assembled on mica studied by atomic force microscopy," Langmuir **12** (2), 235-237 (1996).
- ⁹³ L. Lecamp, F. Houllier, B. Youssef, and C. Bunel, "Photoinitiated cross-linking of a thiol-methacrylate system," Polymer **42** (7), 2727-2736 (2001).
- ⁹⁴ D. Burget, C. Mallein, and J. P. Fouassier, "Photopolymerization of thiol-allyl ether and thiol-acrylate coatings with visible light photosensitive systems," Polymer **45** (19), 6561-6567 (2004).
- ⁹⁵ B. Ranby and J.F. Rabek, *Photodegradation, Photo-Oxidation and Photostabilization of Polymers*. (John Wiley & Sons, London, New York, Sydney, Toronto, 1975).

- ⁹⁶ S.L. Bourke and J. Kohn, "Polymers derived from the amino acid -tyrosine: polycarbonates, polyarylates and copolymers with poly(ethylene glycol)," *Advanced Drug Delivery Reviews* **55** (4), 447-466 (2003).
- ⁹⁷ L.G. Rao, L.J.F. Liu, T.M.C. Murray, E. McDermott, and X. Zhang, "Estrogen Added Intermittently, but Not Continuously, Stimulates Differentiation and Bone Formation in SaOS-2 Cells," *Biol. Pharm. Bull.* **26**, 936-945 (2003); C.M. Stanford, P.A. Jacobson, E.D. Eanes, L.A. Lembke, and R.J. Midura, "Rapidly Forming Apatitic Mineral in an Osteoblastic Cell Line (UMR 106-01 BSP)," *Journal of Biological Chemistry* **270** (16), 9420-9428 (1995).
- ⁹⁸ S. Shima and M. Oyane, "Plasticity Theory for Porous Metals " *International Journal of Mechanical Sciences* **18** (6), 285-291 (1976).
- ⁹⁹ X. M. Liao and T. S. Wiedmann, "Characterization of pharmaceutical solids by scanning probe microscopy," *Journal of Pharmaceutical Sciences* **93** (9), 2250-2258 (2004).
- ¹⁰⁰ G. Alderborn and C. Nyström, *Pharmaceutical Powder Compaction Technology*. (Marcel Dekker, New York, 1996), pp.xv, 610 p.
- ¹⁰¹ W.C. Duncan-Hewitt and G.C. Weatherly, "Evaluating the hardness, Young's modulus and fracture toughness of some pharmaceutical crystals using microindentation techniques," *Journal of Materials Science Letters* **8** (11), 1350-1352 (1989).

Curriculum Vita

Milca I. Aponte

A. Professional Preparation

Rutgers, State University of New Jersey	Materials Science & Engineering	Ph.D.	2010
Rutgers, State University of New Jersey	Materials Science & Engineering	M.S.	2008
University of Puerto Rico at Humacao	Physics Applied to Electronics	B.S.	2004

B. Experience

Graduate Research Assistant	Dept. Materials Science & Engineering, Rutgers, The State University of New Jersey Piscataway, NJ	2004-2010
Graduate Research Assistant	Dept. Cell Biology & Neuroscience, Rutgers, The State University of New Jersey Piscataway, NJ	Summer 2008
Teacher's Assistant	Dept. Materials Science & Engineering, Rutgers, The State University of New Jersey Piscataway, NJ	2008 & 2005
Summer Intern	Dept. Analytical Research and Development Bristol-Myers Squibb New Brunswick, NJ	Summer 2006
Undergraduate Summer Internship	National Science Foundation-REU Summer Program in Materials Science, University of Pennsylvania	Summer 2001
Undergraduate Research Assistant	Dep. Physics Applied to Electronics, University of Puerto Rico Humacao, PR	2000- 2004

C. Publications

- **M. Aponte**, A.B. Mann. "Nanomechanics of Self-Assembled Monolayers on Nanoscale Gold Films", in *Mechanics of Nanoscale Materials*, edited by C. Friesen, R.C. Cammarata, A. Hodge, O.L. Warren (Mater. Res. Soc. Symp. Proc. **Volume 1086E**, Warrendale, PA, 2008), 1086-U08-27
- Y. Wang, **M. Aponte**, N. León, I. Ramos, R. Furlan, N. Pinto, and J.J. Santiago-Avilés. "Tin Oxide Micro/Nano Fibers from Electrostatic Deposition", *Rev. Mex. de Fís. S*, Vol. 52, Num.2, 42-44, February, 2006
- Y. Wang, **M. Aponte**, N. León, I. Ramos, R. Furlan, S. Evoy, and J. J. Santiago-Aviles. "Synthesis and Characterization of Tin Oxide Micro/Nano-Fibers using Electrospinning", *Journal of The American Ceramic Society* 88 (8): 2059-2063, 2005
- Yu Wang, **Milca Aponte**, Neliza Leon, Idalia Ramos, Rogerio Furlan, Stephane Evoy, and Jorge J. Santiago-Avilés. "Synthesis and Characterization of Tin Oxide Microfibers Electrospun from a Simple Precursor Solution", *Semiconductor Science and Technology*, **19** (8) 1057 -1060, 2004
- **M. Aponte** and C. Guerra. "A simple Non-Destructive Technique to Measure the Elastic Constant of Concrete during the Curing Process" *Proceedings of the Fourth National Conference for Women in Puerto Rico*, **4** 6-9, 2003